BEHAVIOUR OF CANDU® FUEL AFTER A LOSS OF COOLANT ACCIDENT IN AN IRRADIATED FUEL BAY

COMPORTEMENT DU COMBUSTIBLE CANDU® À LA SUITE D'UNE PERTE DE CALOPORTEUR DANS LA PISCINE DE STOCKAGE DU COMBUSTIBLE ÉPUISÉ

A Thesis Submitted to the Division of Graduate Studies

of the Royal Military College of Canada

by

Derek Logtenberg, BASc.

In Partial Fulfillment of the Requirements for the Degree of

Master of Applied Science

January 2019

i. ACKNOWLEDGEMENTS

I feel extremely fortunate to have worked under consistently excellent mentorship during the entirety of my Master's Degree. I'd like to thank my thesis advisors Dr. Chan and Dr. Corcoran for their unwavering support and continual feedback in the development of this work. This experience has greatly furthered my career and personal growth, and I am highly appreciative of their efforts. I would also like to thank Dr. Bonin for his assistance in this thesis.

I am also grateful to the Royal Military College of Canada and Canadian Nuclear Safety Commission (CNSC), which jointly allowed me to participate in the graduate co-op program in the Physics and Fuel Division. Vali Tavasoli, the manager of physics and fuel, and numerous other staff at the CNSC offered a tremendous amount of support and guidance during the experience. I would also like to say thank you to Wade Grant for acting as my supervisor and ensuring I always had the resources necessary to do what I needed.

I would like to acknowledge the National Science and Engineering Research Council (NSERC) for their assistance in funding this MASc. level thesis project through the Collaborative Research and Development Grant (Project #: 509799-17).

I wish to thank my parents for their support and encouragement throughout my study. Thanks to everyone who pushed me to take on new challenges and believed in me when I was still figuring things out.

ii. ABSTRACT

After CANDU fuel is discharged from the reactor, it is submersed in large pools of water in Irradiated Fuel Bays (IFBs) to remove their decay heat. It has been postulated that a large-scale drainage scenario i.e. Loss of Coolant Accident (LOCA) in an IFB could lead to a release of radioactivity if the fuel reaches temperatures sufficient for a runaway oxidation of the Zircaloy-4 sheathing. The near miss at the Fukushima Diachii Spent Fuel Pools (SFPs) has prompted international efforts to better define the safety margins after irradiated fuel has been exposed to air. The purpose of this work is to support the development of an IFB severe accident code, specifically for CANDU type nuclear generating stations.

A literature review and stress analysis of a fuel element were performed to determine the risk of overstraining and ballooning due to heat-up in a depressurized environment. It was concluded that overstrains were possible for elements with extremely high fission gas release, but only after embrittlement of the sheath due to oxidation. In the development of a severe accident code, defects arising from overstrain may be correlated to temperature to simplify the analysis. If a mass failure of fuel sheaths is predicted, the effect of ballooning is expected to become significant.

In the concomitant analysis, the heat transfer behaviour of a 2-D bundle cross-section was simulated using COMSOL Multiphysics®. Several sensitivity studies were completed at steady-state to explore the effects of ballooning, fuel-sheath gap size and fill gas composition on the maximum temperatures in the fuel. It was shown the inclusion of conduction in the element's interior enhanced heat transfer and resulted in slightly lower maximum temperatures. Transient analyses were also completed to determine when oxidation (1) becomes a significant effect, and (2) is estimated to transition to linear reaction kinetics after which it may become self-sustaining. The transition was predicted to occur within 2.6 hours for a 4 kW bundle, which could be considered as an upper bound for the heat generation produced by an exposed IFB bundle. Therefore, due to the time required for heat up and the delay in the initiation of breakaway, it was indicated that sufficient margin exists for operators to intervene before a passively cooled, isolated bundle undergoes a breakaway reaction.

The cumulative effect of neighbouring bundles has the potential to adversely impact the heat dissipation process. Scaling up to a full-scale CANDU IFB or even IFB rack is difficult due to the complex bundle geometry and open rack design. In the last part of this work, a process to predict the steady-state temperature and mass fluxes of air as it passes through a rack of spent fuel using analytical models and computational fluid dynamics (CFDs) techniques is presented. The scenario acts as a lower bound estimate for the temperatures expected during a complete loss of coolant in a fuel bay by examining the 3-D heat-up of a stand-alone quarter rack without flow resistance of the bundles. The correct incorporation of flow resistance, in a detailed convection model that can be validated by experiment, is a necessary step before conclusions could be made about the safety of IFBs. However, the analysis as summarized in Section 8, using a CFD model for a 0.35 MW fuel rack, indicates that the maximum temperature of the air within the rack was about 575 K and located at the centre of the outlet. This result is encouraging to support the safety of IFBs, as the temperature is well below that required for a breakaway reaction.

iii. RÉSUMÉ

Suivant sa décharge du coeur du réacteur CANDU, le combustible est maintenu submergé sous l'eau dans une grande piscine de stockage du combustible irradié afin d'enlever la chaleur résiduelle. On a postulé qu'un scénario d'un problème majeur de drainage, i.e. un accident de perte de caloporteur dans une piscine, mènerait à un relâchement de radioactivité dans le cas où la température du combustible atteindrait des valeurs telles que l'oxydation de la gaine en Zircaloy-4 pourrait s'emballer. Ceci s'est presque produit dans les piscines de stockage de la centrale Fukushima Diachii et a déclenché des efforts internationaux pour améliorer la définition des critères de sûreté à la suite de l'exposition de combustible irradié à l'air libre. Le but du présent travail est de soutenir le développement d'un code de simulation d'un accident majeur dans une piscine de stockage de combustible irradié, dans le contexte plus spécifique des centrales nucléaires de type CANDU.

Une revue bibliographique a été effectuée, et on a analysé les contraintes d'un élément de combustible afin de déterminer les risques de sur-tensions et de gonflage à cause du réchauffement dans un environnement sous pression réduite. On a conclu que les sur-tensions sont possibles pour les éléments avec un relâchement extrême de produits de fission gazeux, mais seulement à la suite de la fragilisation de la gaine causée par l'oxydation. Dans le développement d'un code de simulation d'accident majeur, on peut établir une corrélation entre les défauts créés par les sur-tensions et la température pour simplifier l'analyse. Si une défaillance importante des gaines de combustible est prédite, on s'attend alors à ce que l'effet du gonflement devienne significatif.

Dans une analyse concomitante, on a simulé en deux dimensions à l'aide du logiciel COMSOL Multiphysics® le comportement du transfert de chaleur dans une section transversale d'une grappe de combustible. On a complété plusieurs études de sensibilité en régime permanent afin d'explorer les effets du gonflement de l'espace entre le combustible et la gaine et de déterminer les compositions du gaz de remplissage en fonction des températures maximales dans le combustible. On a démontré qu'inclure la conduction dans l'intérieur de l'élément rehaussait le transfert de chaleur et résultait en une légère diminution des températures maximales. Des analyses en régimes transitoires ont aussi été effectuées pour déterminer d'abord quand l'oxydation devient un effet important, puis quand elle est vue comme effectuant une transition à une cinétique de réaction linéaire avant de devenir auto-suffisante. L'étude a permis de prédire que la transition se produisait en-deçà de 2.6 heures pour une grappe de 4 kW, ce qui peut être considéré comme une limite supérieure pour la production de chaleur par une grappe de combustible irradiée exposée à l'air libre. Par conséquent, à cause du laps de temps nécessaire pour réchauffer la grappe et du délai pour de début de l'emballement, on a montré qu'il existe une marge suffisante pour permettre aux opérateurs d'intervenir avant qu'une grappe de combustible isolée et refroidie de manière passive ne puisse commencer une réaction d'emballement.

L'effet cumulatif de la proximité de plusieurs grappes peut détériorer le processus de dissipation de la chaleur. Il est difficile d'appliquer les méthodes de cette étude à l'échelle de l'entière piscine de stockage du combustible CANDU irradié ou même à l'échelle d'un des paniers à cause de la géométrie complexe de la grappe et de celle du panier. Dans la dernière partie de cette recherche, on présente une procédure pour prédire en régime permanent la température et les flux massiques de l'air qui passe dans un panier plein de combustible épuisé à l'aide de modèles analytiques et de techniques de calcul de la dynamique des fluides. Ce scénario se comporte comme un estimé inférieur donnant les températures attendues au cours d'une perte complète de caloporteur dans une piscine de stockage par l'examen en trois dimensions du réchauffement d'un quart d'un panier en négligeant la résistance des grappes à l'écoulement. Avant que des conclusions puissent être tirées sur la sûreté des piscines de stockage du combustible épuisé, il est nécessaire d'incorporer correctement la résistance à l'écoulement dans un modèle de convection détaillé qui peut être validé par des données expérimentales. Cependant, à l'aide d'un modèle de calcul de la dynamique des fluides pour un panier de combustible de 0.35 MW, une analyse telle que résumée à la Section 8 indique que la température maximale de l'air dans le panier était d'environ 575 K et localisée au centre de la sortie. Ce résultat est encourageant pour le soutien de la sûreté des piscines de stockage des

combustibles épuisés, puisque la température prédite est bien en deçà de celle requise pour une réaction qui s’emballe.

iv. CONTENTS

v. LIST OF FIGURES

vi. LIST OF TABLES

vii. LIST OF ACRONYMS

AECL	- Atomic Energy of Canada Limited
ASTEC	- Accident Source Term Evaluation Code
ATHLET-CD	- Analysis of THermal-hydraulics of LEaks and Transients with Core Degradation
BDBA	- Beyond-Design-Basis Accident
BWR	- Boiling Water Reactors
CANDU	- CANada Deuterium Uranium
CFD	- Computational Fluid Dynamics
CNL	- Canadian Nuclear Laboratories
CNSC	- Canadian Nuclear Safety Commission
DBA	- Design Basis Accident
ELOCA	- Element Loss of Coolant Accident, detailed fuel behaviour code
EPRI	- Electric Power Research Institute
GRS	- Gesellschaft für Anlagen- und Reaktorsicherheit gGmbH
GWd	- Gigawatt days
IFB	- Irradiated Fuel Bay
IRSN	- Institut de Radioprotection et de Sûreté Nucléaire
IKE	- Institut für Kernenergetik und Energiesysteme, University of Stuttgart
LWR	- Light Water Reactors
LOCA	- Loss of Coolant Accident
MAAP	- Modular Accident Analysis Program
MELCOR	- Methods for Estimation of Leakages and COnsequences of Releases
MOX	- Mixed Oxide (Fuel)
MWd	- Megawatt days
NEA	- Nuclear Energy Agency
NEAMS	- Nuclear Energy Fuels Modelling and Simulation
NWMO	- Nuclear Waste Management Organization
PBq	- Picobecquerel
PHWR	- Pressurized Heavy Water Reactor
PKPIRT	- Phenomena and Key Parameters Identification and Ranking Table
PSI	- Paul Scherrer Institute
PWR	- Pressurised Water Reactor
RANS	- Reynolds-Averaged Navier-Stokes
SCC	- Stress Corrosion Cracking

SFUEL	- Spent FUEL (Heat-up Code)
tHM	- (Metric) Tonne of Heavy Metal
USNRC	- United States Nuclear Regulatory Commission

viii. LIST OF SYMBOLS

A_{1E} - Anisotropic strain factor in the circumferential direction

A_{1S} - Anisotropic stress factor in the axial direction

A_{2E} - Anisotropic strain factor in the radial direction

A_{2S} - Anisotropic stress factor in the circumferential direction

A_{3E} - Anisotropic strain factor in the axial direction

A_{3S} - Anisotropic stress factor in the radial direction

A_{top} - Area at the top of the spent fuel rack

A_s - Area on the sides of the spent fuel rack

B_u - Burnup

C - Constant used by gas conductivity correlation

C_d - Overall discharge coefficient

C_{d_top} - Discharge coefficient for the top opening of the spent fuel rack

C_{d_side} - Discharge coefficient for the side openings of the spent fuel rack

C_p - Specific heat capacity at constant pressure

C_{p_avg} - Average specific heat capacity of the air inside the spent fuel rack

E - Young's modulus

F - Force (of buoyancy)

g - Temperature jump distance

G_{rad} - Incident radiation

G_z - Vertical mass flux at the outlet

$\bar{G}_z$ - Mean of the vertical mass flux in a vertical slice of the spent fuel rack

h - Height of the rack

h_{gap} - Convection coefficient of the fuel sheath gap

h_{cond} - Convection coefficient of the fuel sheath gap with only conductive heat transfer

h_{rad} - Convection coefficient of the fuel sheath gap with only radiative heat transfer

H_{out} - Difference in height between the neutral height and the outlet

ΔH_{oxid} - Enthalpy of oxide formation

I - Identity vector

J - Radiosity

k - Conduction coefficient

k_g - Conduction coefficient of the fuel-sheath fill gas

k_r - Temperature dependent rate constant

K - Strength coefficient

K_r - Reaction rate constant

LF - Lifetime integral

m - Strain rate sensitivity exponent

n - Strain hardening exponent

$\hat{n}$ - Normal vector

P - Pressure

P_C - Critical pressure

P_R - Relative pressure

$P(l, z_{i+1})$ - Pressure at the side of the rack (x = l) and the vertical step i +1 (z = z_{i+1})

ΔP - Pressure difference between the internal element and atmosphere

$\Delta P_{x=0}(z_{i+1}, z_i)$ - Pressure difference between steps i +1 and step i at the rack's centre (x = 0)

q_{out} - Volumetric flow of air through the outlet

Q_{oxid} - Heat release associated with oxide formation

Q - Heat source

r_0 - Element radius

R_f - Surface roughness of the fuel

R_{sh} - Surface roughness of the fuel sheath

s - Constant used by gas conductivity correlation

t - Time

t_{gap} - Size of the fuel sheath gap

T - Temperature

T_a - Ambient temperature of the air outside the spent fuel rack

T_{avg} - Average temperature of the sheath and fuel

T_f - Temperature of the fuel surface

T_i - Temperature of the air inside the spent fuel rack

T_{sh} - Temperature of the fuel sheath

T_C - Critical temperature

T_R - Relative temperature

Δt - Time elapsed to reach the specified strain rate with constant temperature conditions

u - Velocity vector

w - Element thickness

w_r - Weight of reacted material per unit area

x - Oxide layer thickness

z_{i+1} - height at step i +1

ε_θ - True circumferential strain

ε_e - True effective strain

ε_f - Emissivity coefficient for the fuel

ε_r - True radial strain

ε_{sh} - Emissivity coefficient for the sheath

ε_z - True axial strain

$\dot{\varepsilon}_e$ - True effective strain rate

ρ - Density

ρ_a - Ambient density of air outside the spent fuel rack

ρ_i - Density of the air inside the spent fuel rack

σ - Stefan–Boltzmann constant

σ_θ - True circumferential stress

σ_e - True effective stress

σ_r - True radial stress

σ_z - True axial stress

μ - Dynamic viscosity

1. INTRODUCTION

The nuclear power industry is a reliable generator of commercial energy. There are over 440 reactors worldwide producing a total of 390 GW, which accounts for 11% of global electricity consumption [1]. In the advent of climate change and sustained population growth, the number of nuclear plants is expected to increase. It has been estimated the amount of power produced will swell from 578 to 2119 TWh by 2030, largely driven by utilities in Asia [2]. China specifically has been under political pressure to improve their air quality and environmental track record, and nuclear has been touted as an option to shift power generation away from the existing coal fleet and decrease their dependence on fossil fuels. Nuclear boasts the lowest lifecycle emissions aside from wind power [3], and its on-demand nature gives it an advantage over many sources of renewable power. Its low carbon footprint and ability to generate large amounts of base-load power are a few of the reasons why nuclear power operates in over 31 countries including Canada [4].

Nuclear power development started in Canada in the 1950s and was realized at full scale with the reactor in Douglas Point, Ontario, in 1967. This was soon followed by the installation of the Pickering plant in 1971, which is still operating today. The Pickering plant was the first commercial implementation of a Pressurized Heavy Water Reactor (PHWR) and the CANDU® (CANada Deuterium Uranium) [5]. Contrary to Light Water Reactors (LWRs), which have since become the standard power plant design internationally, the CANDU design uses heavy water as a moderator and coolant. The primary advantage offered by heavy water is its high neutron economy, which allows it to use natural uranium. The ability of CANDU reactors to burn non-enriched uranium has improved the accessibility and economics of nuclear power for countries that did not have pre-existing nuclear programs and has mitigated proliferation concerns. Argentina, China, India, Pakistan, Romania, and South Korea currently have CANDU or CANDU inspired nuclear reactors in operation today.

The rest of the world's CANDU reactors reside in their native homeland at the Bruce Power, Darlington, and Pickering stations in Ontario and the Point Lepreau station in New Brunswick [6]. The Gentilly-2 reactor located in Bécancour, Quebec, was decommissioned in 2012 and will be followed by the Pickering reactors within the next several years. Conversely Point Lepreau has finished their refurbishment in 2012, and the Bruce Power and Darlington sites are following with projects that will extend their lifetimes to 2064 [7] and 2055 [8], respectively, securing nuclear energy's presence in the province for the next 50 years. Nuclear power generation has grown to cumulatively provide 91.7 TWh, or 61%, of Ontario's total grid power as of 2015 [9]. As a result of nuclear power's expansion, the province has been able to shut down their coal plants and thereby reduce carbon dioxide emissions from 33 to 7 annual megatonnes in the electricity sector over the past 10 years [9]. For Canada to meet the current target of 30% below the 2005 emissions levels by 2030, it is likely that nuclear power must continue to be an important electrical provider in the nation's most populous province.

Although there are many advantages that nuclear power offers, there are also drawbacks. Among the most prominent issues are safety and waste, two topics that converge with the lifecycle management of fuel. Spent fuel, or irradiated fuel as it is also called, refers to discharged fuel that typically can no longer reliably sustain the fission process and is therefore no longer economical to keep in the reactor. However, defueling may occur earlier due to reasons such as in-channel defects, reactor refurbishment or decommissioning. The disposal process of spent fuel follows a three-stage process [10]. In the first stage, the freshly removed fuel is placed in large Irradiated Fuel Bays (IFBs) for seven to ten years where they are provided containment and cooling. Afterward the fuel is moved into dry storage, which in Canada consists primarily of concrete canisters, modular air-cooled storage units or portable dry storage containers that are kept onsite. The Nuclear Waste Management Organization (NWMO) is responsible for planning the indefinite storage and safekeeping of the fuel. Long-term options include the expansion of reactor site storage, the implementation of centralized storage, or the frequently discussed use of a deep geological repository. All phases of the storage process and transport of radioactive materials are overseen and licensed by the Canadian Nuclear Safety Commission (CNSC). The groundwork laid out in

the field of radioactive waste management has created a regulatory environment that ensures nuclear power is generated responsibly and fuel passes from 'Cradle to Grave' in an accountable and safe manner.

However, risks still exist for all phases of storage and it is paramount that utilities and the regulators work together to prevent radiation exposure to the workers, environment, and public. Irradiated fuel requires the most monitoring in the first stage when there is a high thermal load from its decay heat and therefore the state of the fuel needs to be actively managed. As shown in Figure 1 and previously mentioned, discharged bundles are stored underwater in IFBs until their thermal power is sufficiently low to be moved to dry storage.

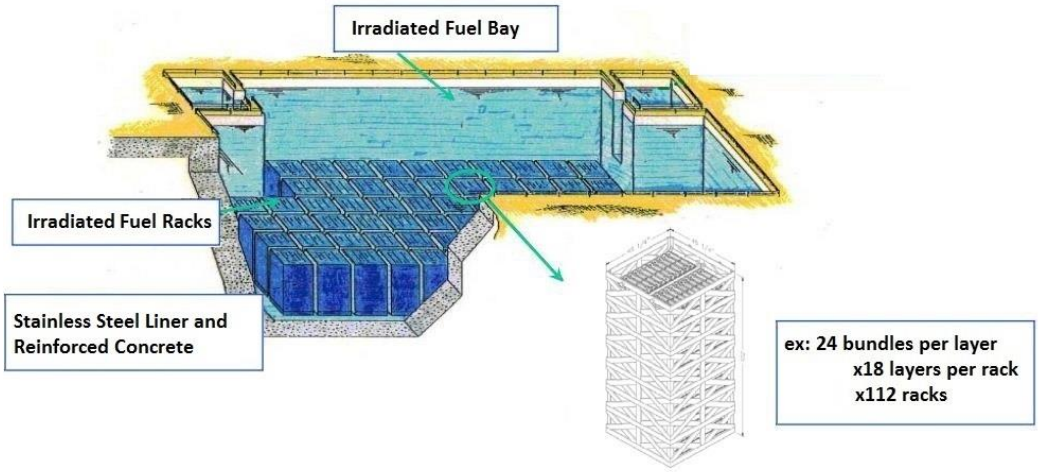

Figure 1:IFB with racks that provide interim storage for spent fuel. The number of bundles is based on a Cernavoda Unit 2 fuel rack and estimates for the number of racks are by Fan [11]. Image adapted from references [12] and [13].

During the in-bay wet storage period, racks are used to efficiently space and facilitate movement of the bundles, and the IFB water provides radiological shielding to workers and maintains cooling. One concern regarding the fuel bays is a hypothetical loss of coolant, in which the water is evaporated away or leaks through the steel liner and surrounding concrete. In this highly unlikely scenario, the bundles may be exposed to an air or steam environment where they would quickly heat-up. In addition to the damage to the fuel itself, the risk is magnified by the oxidation of the zirconium sheath, which is both exothermic and has thermally driven reaction kinetics. When the sheath reaches sufficient temperatures, the oxidation may become a self-sustaining 'breakaway' reaction [12] [14]. Although it is not directly known whether these temperatures would be reached, a breakaway event in CANDU IFBs would increase the probability for fission product release and present an immediate safety risk to the surrounding population and environment. Therefore, it is important water levels above the fuel are maintained.

During the Fukushima Daichii nuclear accident, maintaining water levels became a significant challenge for onsite personnel. In addition to workers, helicopters, cement trucks, and fire trucks were employed to ensure that the fuel was not exposed in the Unit 4 Spent Fuel Pool (SFP). Despite their efforts, the water levels dipped to within almost 1.2 m of the top of the fuel and took over a month to stabilize [15]. The near miss highlighted the need for mitigating equipment and more analysis into severe accidents in the fuel bays.

The accident at Fukushima was considered to be a 'black swan' event. Unlikely as it was, the public, regulators and industry's perspective on severe accidents were dramatically altered and there was suddenly an international demand for research on all aspects of the accident, including events at SFPs. In Canada, the accident highlighted a knowledge gap, as previously a long loss-of-cooling event in IFBs was not considered credible in the safety reports. Therefore, no severe accident analysis of an uncovered

CANDU IFB existed and the safety margins were not determined precisely. In addition to other actions, the CNSC undertook a number of investigative studies to determine if CANDU spent fuel poses the same type of risks as that of LWR fuel. One of the studies supported by CNSC on CANDU fuel was conducted by Krasnaj [16] [17]. Using COMSOL Multiphysics, the dissipation of decay heat from irradiated fuel bundles was examined in an air environment at steady-state conditions. The model identified that freshly discharged fuel bundles pose a risk of a breakaway oxidation reaction, which may occur between 600 to 1000 °C. The study demonstrated that similar risks existed and that further research was required to bring the level of analysis for CANDU IFBs up to the same standard of LWR SFPs. In 2015, this conclusion was punctuated when the Nuclear Energy Agency (NEA) Committee on the Safety of Nuclear Installations recommended a severe accident code be created specifically for CANDU IFBs [12] and in 2016 the CNSC released their plan for its development [18].

There is a demand for theoretical tools to support the development of an IFB severe accident code. The first part of this work will extend the model by Krasnaj to investigate the behaviour of a single bundle and determine: (1) how long does it take for the bundle to heat to 600 °C, (2) when is a breakaway reaction expected to occur, and (3) can intervention be assured before this. The second part will look at convection on the scale of an entire rack and start to estimate how the neighbouring bundles will diminish the cooling capacity of the bundle and heat the surrounding air. With further development, the two models may be able to work together to predict the maximum sheath temperature of fuel on a rack, assess the severity and likelihood of a breakaway oxidation occurring, and make comparisons to the safety margins of LWR fuel pools.

2. GENERAL BACKGROUND

The following sections serve as a more detailed explanation of the areas related to the problem described in the introduction. They are meant to familiarize the reader with the broader context of CANDU fuel, IFBs and the Fukushima accident.

2.1. Fuel Bundles and Racks

CANDU fuel bundles consist of hollow sheaths containing the fuel pellets, which are welded to endcaps and subsequently endplates as shown in Figure 2. They are roughly a half metre long, have a 0.1 m diameter, weigh 22 kg and have 28 or 37 elements depending on the CANDU reactor type [19].

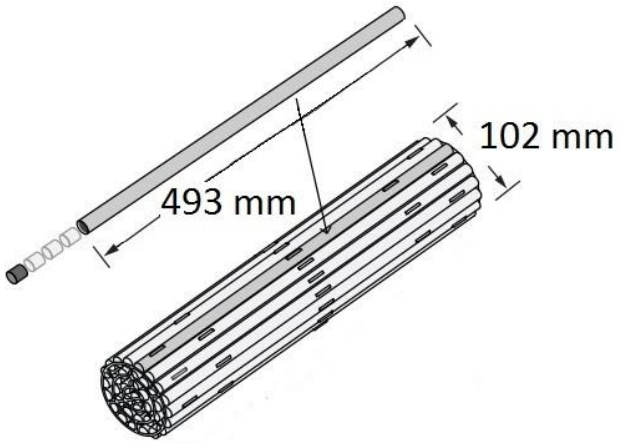

Figure 2: Overall dimensions for a CANDU 37 element fuel bundle. The fuel sheath, or cladding, is a hollow structure that holds the uranium fuel pellets. The sheath and pellets together are considered a fuel element or rod. Image adapted from reference [20].

The sheaths are made of Zircaloy-4, which is primarily composed of zirconium and small quantities of other metals. The ceramic uranium dioxide pellets inside the sheath have a natural isotopic level of the fissile U-235 atom at 0.72% compared to the enriched 2-5% used in LWRs [21]. This feature has made CANDU fuel significantly more economical to manufacture than other fuel types. CANLUB, a graphite coating, is applied to the inside of the sheath to reduce the possibility of Stress Corrosion Cracking (SCC).

There are three types of racks in Canada: the Pickering Basket, the CANDU 6/Bruce tray and the Darlington module [22]. As shown on the right in Figure 3, CANDU 6 racks are loaded horizontally and comprised of 18-19 stacked trays each holding 24 bundles.

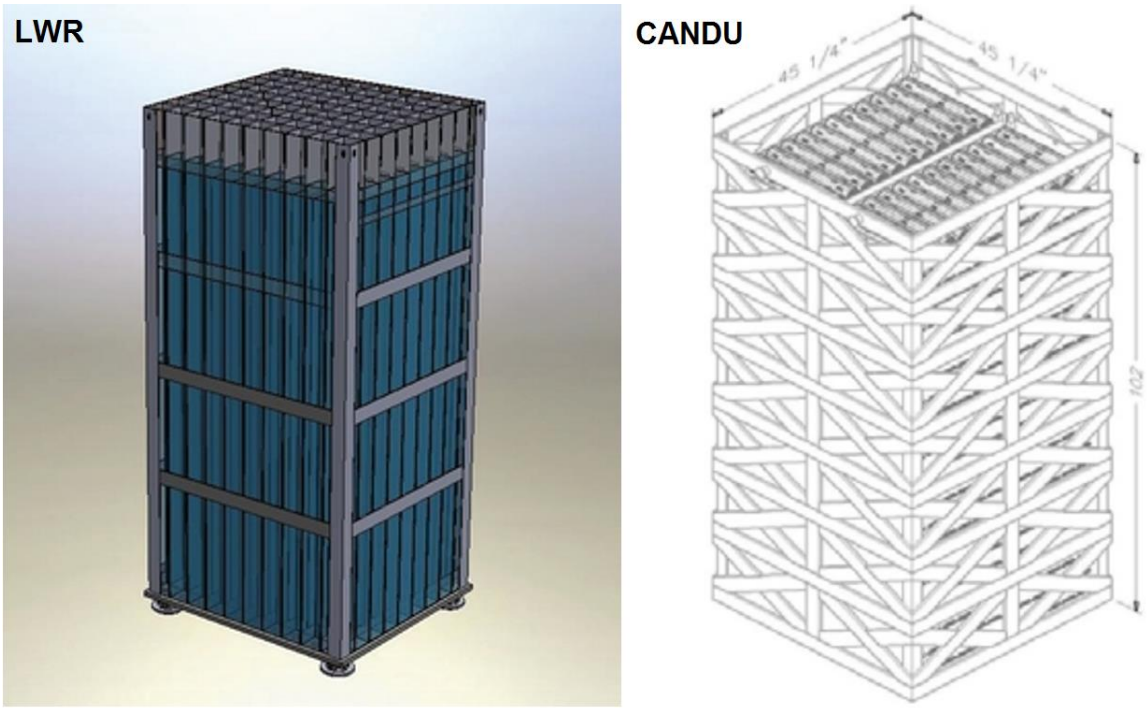

Figure 3: Generic LWR fuel rack [23] (left) and CANDU 6 fuel rack from the Cernavoda plant in Romania [11] (right).

Also shown in Figure 3 is a LWR fuel rack for comparison. There are many differences between the two racks primarily due to the design requirements imposed by the fuel, the most significant of which have been summarized in Table 1.

Table 1: Summary of differences between LWR and CANDU fuel and racks [12].

CANDU IFBs	LWR SFPs
• Small, horizontally loaded bundles • Open fuel rack frames • Continuous Refuelling • Wide pools • Low burn-up • Criticality is not a concern	• Large, vertically aligned bundles • Closed fuel rack frames • Batch Refuelling • Deep pools • Large spacing between elements

An apparent difference is that LWR fuel is much larger in size. While CANDU bundles are light enough to be carried by hand, LWR assemblies need to be vertically loaded using cranes. These fuel LWR assemblies are approximately 4 m long with rods packed in a more spaced out 17 x 17 arrangement [24]. LWR racks also require closed frames with neutron absorbing material to mitigate the risk of criticality. Conversely, CANDU fuel is not at risk of criticality, so utilities have the opportunity to use a densely packed, open frame design.

The open rack design has complicated the analysis of CANDU spent fuel racks in air and made them inaccessible to the same techniques applied to simulate Loss of Coolant Accidents (LOCAs) in LWR

SFPs. Open racks by definition have multiple pathways for fluid to travel, which is expected to yield more effective convection and lower temperatures [25]. Due to the side flows predicted in a drained IFB, the convection pattern will be different from the axial flow conditions in a CANDU reactor and the predominantly vertical convection expected in LWR SFPs. Therefore, existing CANDU thermal-hydraulic codes cannot be directly applied to CANDU IFBs, nor can the codes that are designed to assess LWR spent fuel accidents. The complex geometry of many CANDU bundles further aggravates the issue. Assuming a 19-layer stack, a single fuel rack can hold nearly 456 bundles or 16,872 individual rods when fully loaded. Without a myriad of simplifying assumptions and support from experiments, the direct mathematical analysis is virtually impossible. During a LOCA, CANDU spent fuel bays present a unique and difficult problem that has yet to be addressed.

2.2. CANDU IFBs

During normal fuel bay operation, the decay heat from the bundle is carried away by the cooling system of the pool. There are three main sections of IFBs, which together can hold between 50,000 – 200,000 fuel assemblies. The reception bay is a relatively small pool for bundles that have been discharged within one to two weeks. There is also the transfer bay, which facilitates the loading and unloading of fuel bundles, and the main storage bay where most bundles reside until they are transferred to dry storage. Numerous safety systems are in place to prevent accidents in the pool. The water levels, temperature, pressure, flow speed, radiation, and status of pump and valves are all continuously being monitored via instrumentation. The fuel pool's sensors relay information to both a local control panel and the main control room. Redundant pumps are installed on the cooling line and emergency-pumping systems must be readily available. Some passive safeguards include the three to five metres minimum of cover water, double walls of 1.5 m thick concrete and the steel floor liner, which extends up the sides of the pool. A more extensive description of CANDU IFBs is available in reference [12]. CANDU IFBs are also seismically qualified, located in areas that are not historically prone to earthquakes and are situated below grade [26]. The aforementioned features make a rapid draining of the coolant extremely unlikely, and the double reinforced walls ensure that any failure of the liner will not result in the immediate exposure of the fuel.

In the unlikely event of an extended power loss or an event that causes structural damage to the bay, water levels will be depleted and this could challenge the cooling functions of the IFB. The most probable cause of loss of coolant is believed to be a break at the outlet of the IFB cooling pump, which would cause the water level to drain down below the cooling circuit inlet. Fortunately, there is a significant amount of time before the event transitions to a large-scale LOCA and operator intervention is expected to halt the Design Basis Accident (DBA) before the pool's temperature limits are reached. By definition, DBAs have a probability of occurring once every 100 to 100,000 years per reactor. However, if an event progresses to a Beyond-Design-Basis Accident (BDBA), the fuel may become exposed to a steam, steam-air or air environment where the impaired cooling would lead to severe fuel damage. The probability of such an occurrence is far less likely. BDBAs have a probability of occurring once every 100,000 to 10,000,000 years per reactor, with the United States Nuclear Regulatory Commission (USNRC) predicting that likelihood to be once every 0.5 to 1.72 million years per SFP [14].

However, if a loss of coolant event continues without intervention, its progression would follow the phenomenology outlined in Figure 4. In the first stage, a loss of cooling would cause the water temperatures to climb at a rate of approximately 1 °C per hour. Natural circulation of the water during this time will limit fuel temperatures such that no damage would be expected. Assuming typical conditions and the liner maintains its integrity, after about 2.5 days the water will begin boiling, and 13.3 days later the top of the fuel bundles will be exposed [11]. Once the fuel is exposed though, the degradation would be more rapid. Ballooning and rupture of the fuel elements could be possible due to thermal stresses placed on the fuel.

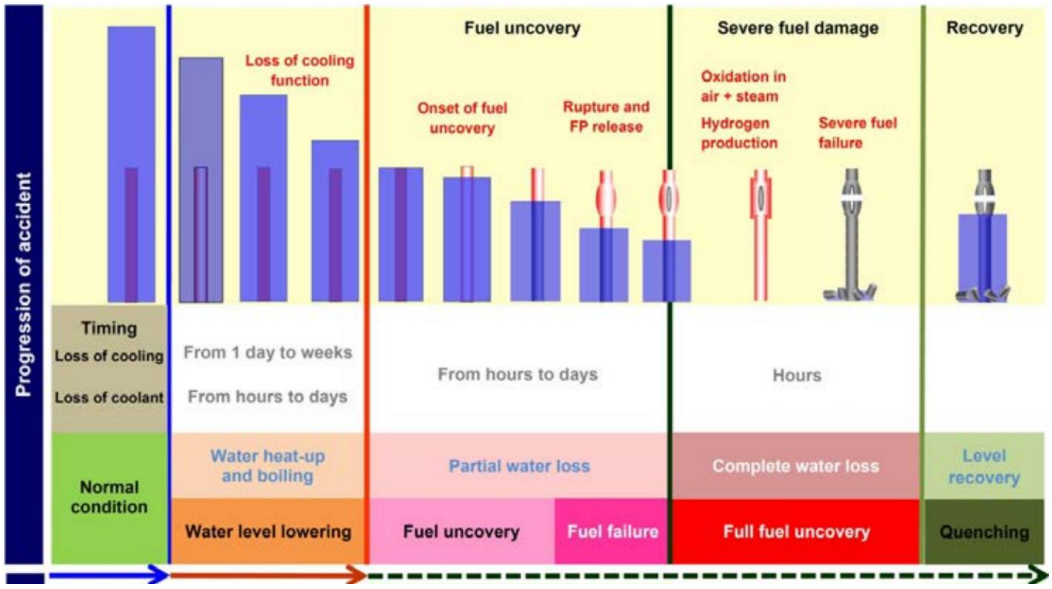

Figure 4: Phenomenology of a spent fuel accident arising from a loss of cooling or loss of coolant event [12].

At elevated temperatures, the oxidation of the zirconium fuel sheath becomes a significant phenomenon and adversely affects the accident in three primary ways: 1) the reaction is highly exothermic, which has a fast reaction rate; 2) it weakens the barrier to fission products, and 3) produces hydrogen. When the fuel is exposed to air, the presence of nitrogen will increase the speed and severity of the oxidation, and therefore the probability of the fuel entering a breakaway reaction is increased. The final recovery phase where the fuel bundles are re-submerged, or quenched with water, marks the end of an accident.

The second and third stages are the most difficult to analytically model and represent the most risk for escalation to a severe accident. It is theorized that convective forces could potentially transport radioactive materials as aerosols out of the building into the surrounding area and have adverse environmental, economic, and health impacts. Certain hypothetical spent fuel release scenarios for LWRs have estimated the potential damage of a zirconium fire to be approximately $57.8 billion US [14]. A larger safety margin has been suggested for spent CANDU fuel since the decay heats are less than that of LWR fuel [18] and a re-criticality event is not possible. There is also a substantial amount of time before these later stages are reached, which is largely why a complete draining of an IFB was considered close to impossible before the Fukushima Daichii accident.

2.3. Fukushima Accident

The Fukushima Daiichi accident has become known as the third major nuclear disaster, alongside the Three Mile Island and Chernobyl incidents. On March 11th, 2011, an earthquake with a 9.0 magnitude struck Japan. The subsequent 15 m high tsunami waves overwhelmed the flood barriers and inundated the Fukushima Daiichi facility. This triggered the mass failure of the backup diesel generators, which came online when the external power supply sources were lost due to earthquake damage. The three affected Boiling Water Reactor (BWR) units had already been successfully shutdown, but they were without power for cooling. Emergency measures in the form of containment venting and injection of fresh and seawater by fire pumps reduced the pressure and heat build-up in the vessels. Freshwater cooling was restored 15 days later, but not before extensive damage and melting had taken place in the cores [15]. Further loss of containment issues arose due to the production of hydrogen, which caused explosions. The three reactors that underwent meltdowns and an additional unit damaged in an explosion

have been slated for decommissioning. A total of 940 Picobecquerels (PBq) of Iodine equivalent radioactive material was released in the accident [15] which necessitated the evacuation of 154,000 people within the 30 km zone surrounding Fukushima, of which 97,000 remain displaced as of 2016 [27].

The incidents in the reactors overshadowed the near miss that occurred in the SFPs. As previously discussed, spent fuel must be submerged in water to keep their temperature levels under control. After the hydrogen explosion in the defueled unit 4, the SFPs in the adjacent buildings became contaminated and access to the pools was greatly restricted. Therefore, the task of directly monitoring the pools and adding make-up water became much more difficult. SFP #4, in particular, contained recently discharged fuel and had a particularly high thermal load of 3 MW. As shown in Figure 5, operators managed to keep the fuel in SFP #4 submerged during the accident, but there were clearly difficulties.

For more than a month the water levels went basically unmeasured, and for more than two months the pool was still boiling. Early on, a helicopter was used to visually confirm that water levels were above the fuel. Soon after, make-up water was delivered to the pool through holes in the building that were created by the aforementioned hydrogen explosion. This was initially performed by fire trucks and later using a cement truck boom to more accurately aim the water.

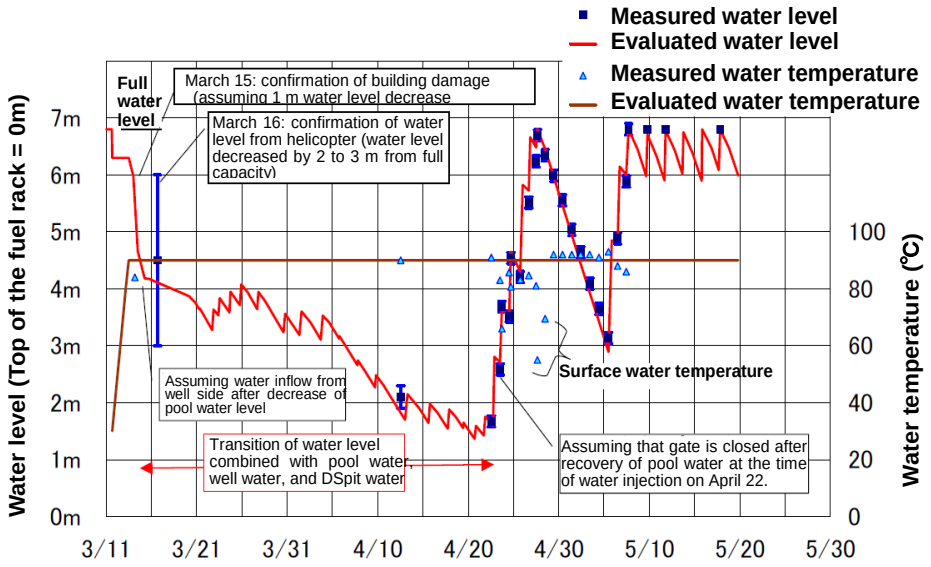

Figure 5: Temperature and water levels in Fukushima Daiichi Unit 4's SFP over time [18].

The post-accident inspection verified that the water reached its minimum level 1.2 m above the top of the fuel on April 22nd [15]. The unorthodox methods applied during the recovery and measurements from the fuel pool indicated the safety margin for the fuel being uncovered was small. The other three SFPs on the site also received supplemental water to replace losses but were not as problematic. New cooling circuits were installed on pools 1-3 to treat the overheated fuel pools and stabilized their status. Due to the use of seawater during the recovery effort, desalination of the pools and post-accident inspections for corrosion were also required.

Although the SFPs did not contribute to the release of radioactive material, there have been wide-sweeping reverberations due to the overall accident. In Japan, nearly 100,000 people are still displaced and, although there have been no direct mortalities due to the radiation [15], the evacuation process caused the deaths of an estimated 1,200 people. Furthermore, the evacuation zone itself represents 20 km of land that will remain uninhabitable for decades. It has profoundly changed the outlook for the industry too. Before the accident, the nuclear industry provided 7.6% of the world's total energy and projections

for its future market share were expected to be between 5.0% - 11.9% by 2050 [28]. Today these projections have been cut in half (to 2.1% - 4.9% by 2050, with growth in the industry dependent on rising global energy demand rather than taking over market share) [2]. To prevent the reoccurrence of a similar scale accident, international efforts have been initiated to better understand all aspects that lead to the failures at Fukushima.

The Fukushima Diachii nuclear accident was widely regarded as an unpredictable, black swan event, but many agreed the disaster's mitigation in many aspects could have been improved [29]. In addition to other measures outlined in the *"Integrated Action Plan On the Lessons Learned From the Fukushima Daiichi Nuclear Accident"* [30], the CNSC has conducted more research related to fuel bays. The Canadian nuclear industry was also required to upgrade their emergency mitigating response plans for fuel bays. These actions have decreased the probability of an accident escalating to the scale of the Fukushima Daiichi disaster and helped improve the safety of fuel in wet storage.

3. STATE OF THE ART

Studies suggesting a loss-of-pool-coolant event could trigger a breakaway oxidation have existed since the late 1970s [31]. Initial studies of CANDU IFBs have focused on the first stages of an accident including the draining of the fuel pools [11], and have only recently been expanded to consider the dry-out stages of the accident [17]. Due to significant differences between the design and storage configurations, studies on drained CANDU IFBs have a limited relevance to other reactor's SFPs and vice versa. For this reason, the developments internationally and for CANDU are discussed separately.

3.1. International

The simulation tools and research completed on LWRs represent the most sophisticated level of analysis completed on spent fuel accidents to date. Some of the most widely used internationally are ASTEC [32], ATHLET-CD [33], MAAP5 [34] and MELCOR [35]. These codes are capable of simulating different aspects of failure including thermal-hydraulics, criticality, fuel behaviour, degradation and fission product release. However, arguably the most important tools are the severe accident codes that can predict the impact of an accident through the temperatures, fission release, hydrogen generation and other key outputs. Most of the severe accident codes used were originally thermalhydraulic codes for simulating an in-reactor LOCAs, but have been repurposed for SFPs [12].

The ASTEC system code was jointly developed through a partnership between the Institut de Radioprotection et de Sûreté (IRSN) in France and the Gesellschaft für Anlagen- und Reaktorsicherheit (GRS) in Germany. It is composed of many different modules, each simulating a distinct reactor zone or physical phenomenon, that can be coupled to calculate the overall state of an accident or run independently [32]. Similarly, ATHLET-CD, developed by GRS and the University of Stuttgart (IKE), and MAAP5, developed by the Electric Power Research Institute (EPRI), use a modular structure. The aforementioned codes are based in FORTRAN and consider the following phenomena in Pressurized Water Reactors (PWRs) and BWRs [12] [36]:

- Radiation, convection, and conduction;
- Boiling and two-phase flow;
- Air and steam oxidation;
- Fuel degradation;
- Fission-product release; and
- Hydrogen production.

While the fuel is still completely covered, a LOCA's progression in LWR SFPs is similar to that expected in CANDU IFBs. Since LWR cladding also primarily uses Zircaloy-4, the oxidation process in CANDU may be modelled using correlations for LWR fuel. Although some relevant modules could have potentially been leveraged to create a model for CANDU fuel or otherwise serve as a resource, these system codes are not freely accessible. MELCOR on the other hand, developed by the Sandia National Laboratory, openly shares its reference manuals [35] and has consequently become one of the primary references for this work.

The results of integral tests have shown that severe accident codes are able to predict the temperature at various locations along the fuel bundles and capture the time of ignition with reasonable accuracy. These testing programs, typically for air ingress into reactors, are well known and have helped improve existing models; QUENCH, PHEBUS, PARAMETER, and CODEX have been completed by researchers in Germany, France, Russia, and Hungary, respectively [12]. Sandia National Laboratories in the United States also recently published experimental data specifically for validation of SFPs [37] [38]. As shown in Figure 6, MELCOR was able to accurately estimate the time to ignition and sheath temperatures.

However, trials during the 2nd phase of the project showed that fuel assemblies with higher decay heats were less successful and more refinement is needed for modelling oxidation in air.

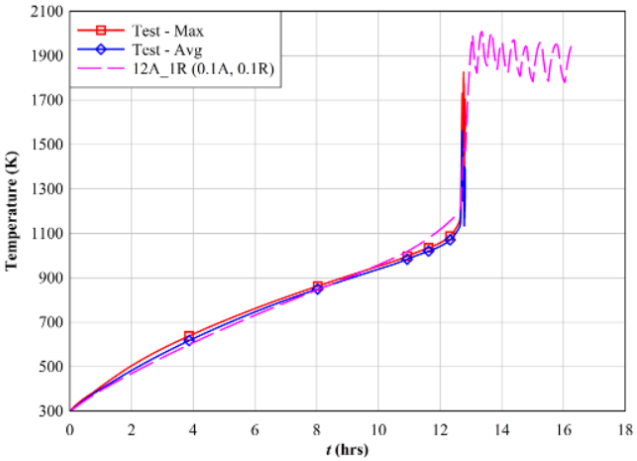

Figure 6: Sandia Lab testing of a single fuel assembly electrically heated with 5 kW and exposed to air [37].

As system codes often rely on empirically based models for complex phenomena, model validation over a wide range of scenarios is crucial. Typically, this is achieved by separate effect tests such as those completed by Steinbrück [39] and Duriez [40] [41] on the behaviour of zirconium-nitrogen reactions. Despite progress made, integral experiments have demonstrated that aspects of the sheath's reaction under air ingress are inherently complex and difficult to model. Some system codes include nitrogen indirectly as a reaction catalyst, which is a simplification that will lead to difficulties for steam-air mixtures and rate limited reactions. Currently, direct modelling of nitride formation and its re-oxidation is limited and remains an area of ongoing research [12]. Therefore, more integral and separate effect tests will be important in the continued development of mechanistic nitriding models.

3.2. Canada

There has been historically weak demand for analysis of severe accidents in CANDU fuel bays due to the comparatively low fuel burnup and large pool sizes, open rack design and the unprecedented nature of fuel bay accidents. One of the most commonly used severe accident codes is the CANDU variant of MAAP, but its applicability to the IFBs is limited due to significant differences in heat transfer between reactor cores and IFBs. Bundles in a reactor are typically subject to forced axial flows, whereas during an IFB LOCA, natural convection is free to occur in all directions.

The first noted open fuel rack analysis was published by the USNRC with the SFUEL code [25]. According to their calculations, they found the open racks had significantly lower temperatures than the closed racks. These studies and the aforementioned lower decay heat and larger pools supported the notion that a larger safety margin existed compared to typical LWR SFPs and therefore should be considered satisfactory for CANDU.

However, the previous attitudes of acceptance changed after the Fukushima Daiichi accident and soon more research became available. One of the first studies post-Fukushima Daiichi was done by Fan *et al.* [11], wherein the configuration of spent fuel in pools was assessed to determine the risk of failure after a loss of cooling. They concluded the risk of fuel failure after a loss of coolant was extremely low given the weeks of time allowed for corrective action.

Meanwhile, studies by Krasnaj [16] [17] examined standard 37 element CANDU spent fuel bundles in an air environment. The first model examined radiative heating in 3D to determine whether a breakaway reaction has the potential to propagate from hot to cold bundles throughout the bay. It was concluded that freshly discharged fuel would not sufficiently heat up the older fuel surrounding them to cause a runaway oxidation, and therefore the risk of a propagating breakaway reaction was low. Another model also created on the COMSOL Multiphysics platform examined steady-state temperatures based on the bundle's decay heat and heat transfer through radiation and natural convection. The model identified that recently discharged fuel bundles pose a risk of entering the temperature range between 600 to 1000 °C as shown in Table 2 where the breakaway oxidation may occur. Preliminary results for a transient model including oxidation were presented [42], but the updated results have not since been published.

Table 2: Steady-state single fuel bundle temperatures in air by Krasnaj model [16].

Average Bundle Power [kW]	Bundle Temperature of Single Mode (Radiative) Analysis [K]		Bundle Temperature of Multi-Mode (Convective and Radiative) Analysis [K]	
	Average	Max	Average	Max
0.5	584	662	491	576
1.0	698	800	613	730
1.5	779	898	705	841
2.0	843	977	779	929
2.5	898	1045	841	1003
3.0	946	1104	895	1068
3.5	989	1157	942	1125
4.0	1028	1206	984	1177

Table 2 showed that there was a risk of breakaway for bundles with thermal powers above 1 kW and further work was necessary to define the existing safety margins. The NEA 2015 *Status Report on the Spent Fuel Pools under a Loss of Cooling and Loss of Coolant Accident Conditions* [12] recommended the development of a severe accident code for CANDU spent fuel. In accordance with the conclusions of the report, the CNSC has initiated development of a severe accident code.

In the first step of the code development, a Phenomena and Key Parameters Identification and Ranking Table (PKPIRT) was created specifically for CANDU spent fuel in collaboration between the CNSC, Canadian Nuclear Laboratories (CNL) and industry experts [22]. The proposed outputs for tracking the severity of the accident were the sheath temperature and radioactivity release from the pool. Four stages were identified in an accident:

1. Fuel Covered, but there is an ongoing loss of coolant
2. Partial Fuel Uncovering, continued loss of coolant
3. Full Fuel Uncovery, Total loss of coolant
4. Fuel is recovered, water injection

During two meetings, experts ranked the importance and knowledge levels of phenomena at each stage of the accident. In total 86 unique phenomena were identified, and 58 were stated to have at least a moderate impact. Of the high and medium importance phenomena, 44 were found to have a low level of knowledge. As per the IFB development project plan, a literature review and research of existing models will be required on each of the significant phenomena. Where models for phenomena are under-developed or knowledge levels are low, experimental programs will be required. Afterward, the code development and verification of the model will begin. The full diagram of the CNSC development plan [29] is shown in Figure 7.

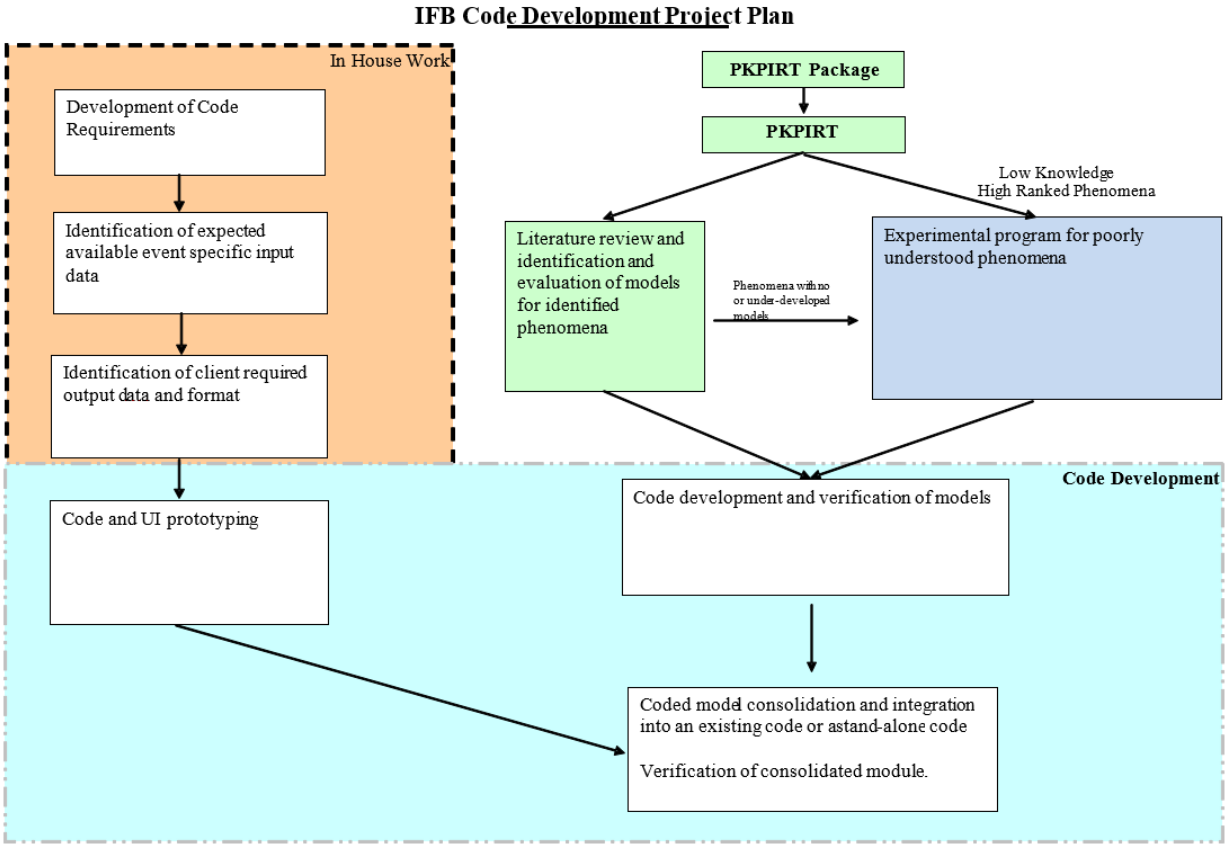

Figure 7: CNSC code development plan [18]. The PKPIRT has been completed and experimental programs are being initiated.

The sheath temperature was identified as a key figure of merit to monitor the severity of the accident as it is one of the primary determinants of fuel failure. Fission product release and hydrogen generation are other significant variables to track an accident's progression. However, experiments completed by Atomic Energy of Canada Limited (AECL) at Chalk River have shown the fuel matrix and sheath are relatively effective at containing fission gases up to the temperatures observed in the Krasnaj model. Punctured elements were observed to have limited fission product release after 24 h at 400 °C, 2 h at 600 °C or 2.5 h at 900 °C [43].

During the third phase of the accident, 29 high importance phenomena were identified, which could be broadly grouped as the initial conditions of the IFB, heat transfer mechanisms, mechanical and chemical degradation, fission product release, exothermic reactions, and hydrogen release. While detailed accident progression models already exist for IFB drainage (Stage 1), there is far more uncertainty with respect to the accident's progression after exposure of the fuel to air. After the fuel is exposed to air, the PKPIRT identified convection in the CANDU racks as a highly important, but poorly understood phenomenon [44]. To address this knowledge gap, a preliminary model was derived for a rack with freshly discharged fuel during the PKPIRT [45]. However, there was interest in further expanding the results and defining the applicability of the model. It was also important to verify the results of this analysis as it provides a lower bound estimate for fuel temperatures during a LOCA. Furthermore, the model provides a theoretical basis for convective heat transfer in the fuel bay, which will potentially be useful in the development of an accident code.

4. OBJECTIVES OF RESEARCH

Wet storage of fuel became a focus of international concerns after the loss of power accident at the Fukushima Daiichi power plants. Previously, it had been assumed the inherent risk of spent fuel bundles being exposed on a pool scale was negligible, but the near miss at Fukushima has changed that belief. In response, utilities and regulators have improved their accident response plans and have put more resources into defining the safety margins [30]. The objective of this thesis is to examine the safety margins of IFBs in the event of a LOCA with a special focus on the later stages of the accident after the fuel bundles have dried out. The PKPIRT [22] conducted recently, as detailed in Section 3.2, gives an extensive list of phenomena that would need to be considered in a full-scale accident code. However, the requirements outlined in the PKPIRT document are considered to exceed the scope of this thesis project. The model produced in this thesis does not supersede the need for a severe accident code, but rather will support the development and validation process.

It has been proposed that the model of Krasnaj be extended to model oxidation to determine when a breakaway reaction is expected to occur and whether intervention can be assured beforehand. Continuing in COMSOL, simulations have been made to predict the temperature profile of an irradiated fuel bundle exposed to an air environment with oxidation and a volumetric heat generation model. The fuel's mechanical degradation was not considered for this Masters level thesis. One of the primary benefits of modelling stress-strain mechanics in the fuel would be to determine the extent of fission gases released, but as discussed in Section 3.2 and without a rapid change in power, these releases are not expected to be significant in the short term [46]. Steady-state investigations into the effect of deformation on temperatures due to element ballooning and changes in conduction across the fuel-sheath gap have been conducted to determine its importance in the heat transfer process.

The most critical aspect that has not yet been studied in detail is the effect of neighbouring fuel bundles in racks. Early work has shown that simplifications of the rack and fuel geometry will be required to make progress in simulation. The second part will look at convection on the scale of an entire rack without flow resistance and estimate how much the neighbouring bundles will diminish the cooling capacity of the bundle. With further development, the two models may be able to work together to predict the maximum sheath temperature of fuel on a rack and thereby assess the severity and likelihood of a breakaway oxidation occurring and make comparisons to LWR SFPs.

The proposed project will help support the development for a CANDU severe accident modelling tool, as outlined by the NEA in their 2015 report [12], that is of comparable scale to existing codes for PWRs and BWRs. Effectively, it will help regulators to assess whether the existing safety margins of CANDU fuel bundles are adequate or whether they need to be adjusted. The benefits of a successful project to stakeholders are profound. Conclusive results will grant the public, industry, and regulators further assurances that spent nuclear fuel is safe and can be reliably contained in wet and dry storage.

5. HEAT TRANSFER AND GENERATION BACKGROUND

To simulate the temperatures of spent fuel bundles for an uncovered CANDU IFB, the model needs to incorporate the active modes of heat transfer and generation in a fuel bay. The fundamentals of the thermodynamic problem will be discussed in the following section.

5.1. Decay Heat

Nuclear power is driven by the heat generated by the induced fission of atoms in the fuel. A small percentage of the uranium fuel contains the fissile isotope Uranium-235 (U-235), which readily splits into multiple atoms after absorbing a neutron. CANDU reactors use uranium oxide, which has natural U-235 levels of 0.72%, while in LWRs the content of U-235 in the fuel is enriched to 2.5-5%. About 200 MeV of energy is immediately released in this nuclear reaction as shown in Figure 8, along with 2-3 neutrons, which propagates the nuclear reaction.

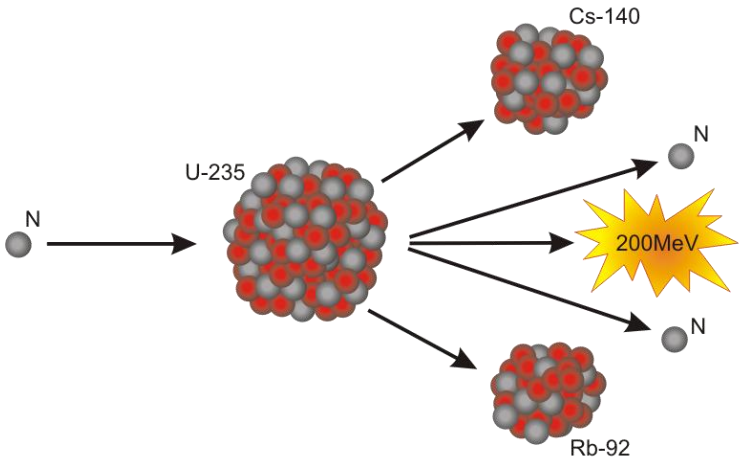

Figure 8: Example of fission reaction for an uranium 235 isotope. A neutron impacts the fissile atom causing it to split into two fission fragments and the release of further neutrons and energy [47].

U-238 and Pu-239 will also fission after absorbing a neutron, however they contribute less total energy than U-235 fissions in a thermal reactor. The amount of energy released per kg of fuel is defined as the burn-up and is often expressed in terms of gigawatt or megawatt days (GWd or MWd, respectively) per kg or tonne of heavy metal. The newly formed atoms undergo further nuclear reactions to achieve a stable state, which releases more energy in the form of gamma radiation and alpha, beta or neutron particles. This series of reactions is called the radioactive decay chain and its power emitted is called the decay heat.

The decay heat varies significantly for different fuels and depends heavily on its in-reactor power history and burn-up. Short-lived fission products and continuing fissions due to delayed neutrons make up the majority of the decay heat early on and therefore have been found to be similar for different types of fuels. This is shown in Figure 9 and matches the conclusions of researchers at Oak Ridge National Laboratories who compared LWR uranium oxide fuel to mixed oxide (MOX) fuels [21]. For freshly discharged CANDU fuel, the decay heats were calculated to be essentially the same as LWR fuel per kg despite large differences in burn-up.

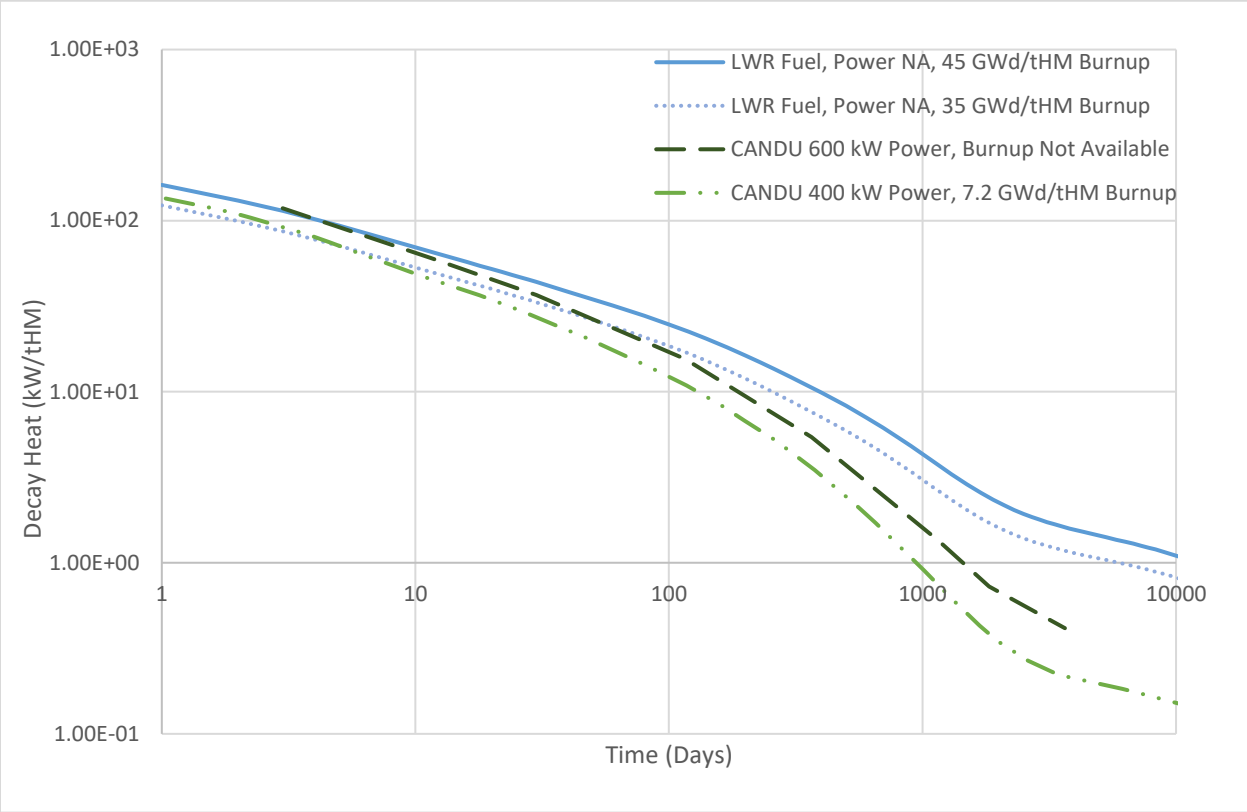

Figure 9: Comparison of decay heats for CANDU [48] and LWRs as measured by Oak Ridge National Laboratory (ORNL) [21]. The LWR fuel had a burnup of 45 GWd per tonne of Heavy Metal (tHM). It is assumed each CANDU bundle has 19.3 kg of heavy metal.

The original data by Fan [11] for determining the thermal output per kilogram of spent CANDU fuel are shown in Table 3.

Table 3: Long term decay powers for a CANDU fuel bundle.

Decay time (s)	Decay Time	Normalized Decay Power	Design Bundle Power (kW)	Typical Bundle Power (kW)
0.0	Leaving the core	1.000000000	800.0	600.0
2.59E+05	3 days	0.003800000	3.040	2.280
1.00E+06	11.6 days	0.001940000	1.552	1.164
2.59E+06	1 month	0.001180000	0.944	0.708
1.00E+07	4 months	0.000500000	0.400	0.300
3.15E+07	1 year	0.000174800	0.140	0.105
1.00E+08	3.2 years	0.000043320	0.035	0.026
1.58E+08	5 years	0.000022740	0.018	0.014
3.15E+08	10 years	0.000013942	0.011	0.008

For long periods after discharge, long-lived species such as actinides provide the bulk of the decay heat. Since the burn-up is directly related to the number of fissions undergone and the amount of long-lived fission products, the burn-up becomes the dominant factor for predicting the thermal output, and differences become more evident between CANDU and LWR. After a month, CANDU fuel has a thermal output that is 80% of LWR fuel on a weight basis, and after a year it is only 50%. The lower burn-ups of CANDU fuel has been a strong argument for why risks are far smaller than for LWRs. However, data show that this is not relevant for freshly discharged fuel and further emphasize the importance of accident analysis and research into SFPs.

5.2. Oxidation

Although the oxidation phenomena can affect almost all structures in the fuel pool, these concerns are most pronounced with regards to the Zircaloy fuel sheath. As shown by Equations 5.2.1 and 5.2.2 for standard temperature and pressure, the formation of zirconium oxide is highly exothermic [12] .

$$Zr + O_2 \rightarrow ZrO_2 + 1101\ kJ \cdot mol^{-1} \tag{5.2.1}$$

$$Zr + 2H_2O \rightarrow ZrO_2 + 2H_2 + 528\ kJ \cdot mol^{-1} \tag{5.2.2}$$

In the presence of oxygen, Equation 5.2.1 becomes the dominant form of reaction. Equation 5.2.2 is important in the presence of steam and has been extensively studied due to its prevalence in-reactor LOCAs.

Zirconium undergoes oxidation readily at high temperatures and when the protective oxide layer is thin or non-existent. Initially, the oxide layer acts as an inert barrier to reactions that is overcome by the diffusion of oxygen and therefore, the oxide layer's thickness, *x*, may be considered to have a growth that is inversely proportional to itself [49]. The thermally driven aspect of the oxidation kinetics is expressed in the form of a temperature dependent rate constant, k_r, which follows the form of the Arrhenius equation. It follows that the reaction may be described by Equation 5.2.3 [25] where t represents time and T represents temperature as per standard notation.

$$\frac{dx}{dt} = \frac{k_r(T)}{x} \tag{5.2.3}$$

By substituting the oxide layer thickness for the weight of zirconium reacted per unit surface area, w_r, this yields the familiar form of the parabolic growth equation [49]:

$$\frac{dw_r^2}{dt} = K_r(T) \tag{5.2.4}$$

The new constant, K_r, includes additional factors that arise from the change of oxide thickness to weight. It is important to note that there is little standardization of reaction constants. The reaction's K_r value may be in terms of the oxygen or metal reacted, or alternatively Equation 5.2.4 may be expressed such that the weight is proportional to the square root of time (meaning the K_r constant used is also square rooted) depending on the author's preference. Units must be carefully heeded.

The energy release associated with the oxidation, Q_{oxid}, is equal to the change in the weight of the reacted zirconium multiplied by the oxide's enthalpy of formation per kg of zirconium, ΔH_{oxid}. This is expressed in Equation 5.2.5.

$$Q_{oxid} = \frac{K_r(T)}{2w_r}\Delta H_{oxid} \tag{5.2.5}$$

The early oxidation process can be approximated using the preceding formulas for reactions with both air and steam.

As the layer gets thicker and eventually cracks, the protective ability of the oxide diminishes and the reaction accelerates. The transition, or breakaway as it is also called, to accelerated reaction kinetics is

marked by the transformation of the dense zirconium oxide outer layer to one that is porous and has penetrating radial cracks [39] [50]. The transition is most commonly described in literature and models as a change from parabolic to linear kinetics [51].

MELCOR 2.1 [35] offers an empirical correlation to determine the pre-breakaway lifetime as shown by Equation 5.2.6 where T is the sheath temperature in Kelvin and t is the time in seconds.

$$LF = \int_0^t \frac{T^{12.528}}{10^{42.038}}\, dt' \tag{5.2.6}$$

The values in the Equation 5.2.6 have been determined from isothermal oxidation experiments. The transition to post-breakaway kinetics occurs when the lifetime for a particular node, LF, exceeds one. Instead of switching to linear kinetics, a similar accelerating effect can be achieved by continuing with the parabolic set up and a scaled reaction constant. The reaction constants for pre-breakaway and a post-breakaway are shown in Figure 10.

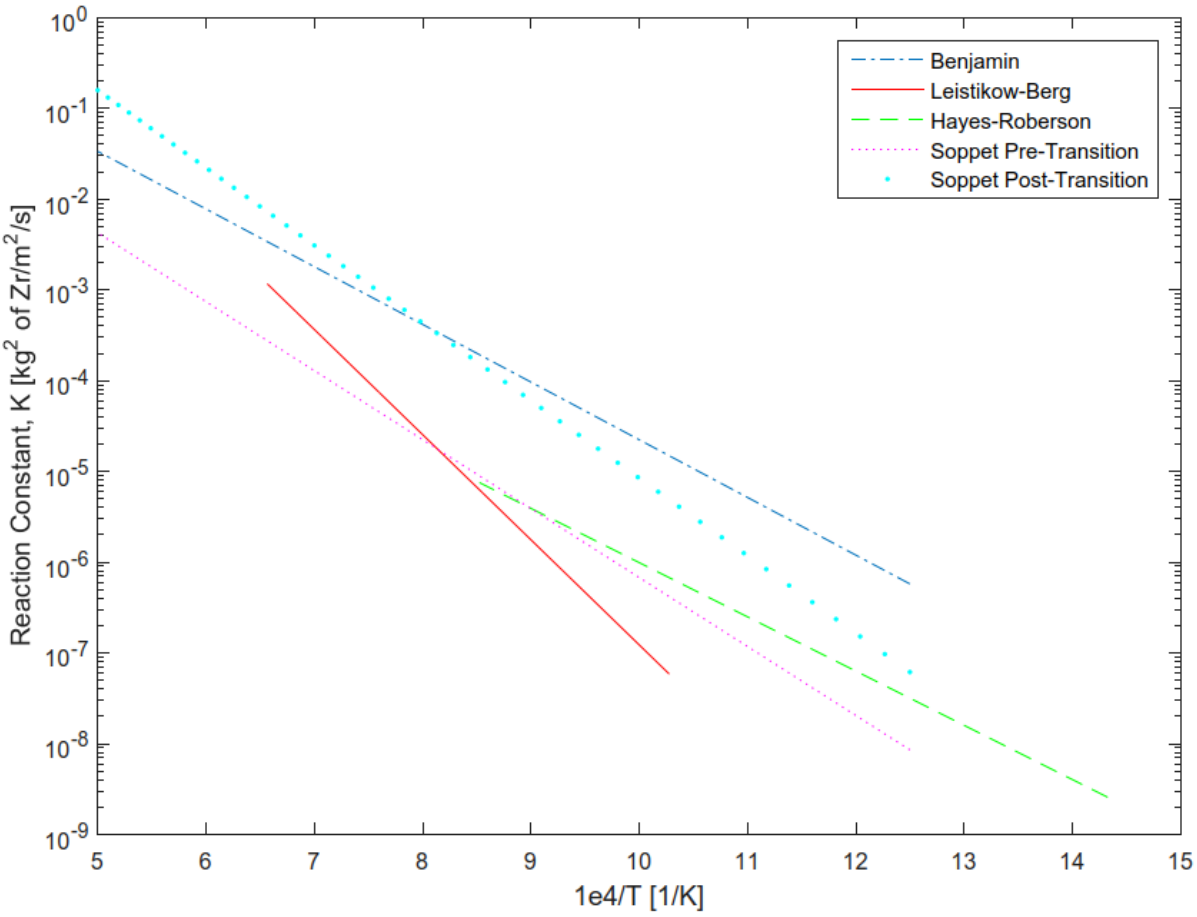

Figure 10: Rate constant, $K_r(T)$, measured by Benjamin [25], Hayes-Roberson [52], Leistikow-Berg [53] and Soppet [50] for zirconium's reaction in air is shown between 700 K and 2000 K (427 – 1727 °C).

Note that the reaction rate constant estimated by Benjamin and used in older versions of the MELCOR [25] code appears to have been conservative. MELCOR 2.1 now offers the best-estimate correlations by Soppet [50] for pre- and post-oxidation, which have been used in this thesis.

Although not shown in the figure above, zirconium's oxidation reaction is much faster in air than in steam and the reaction constant is therefore lower. In addition to a larger amount of thermal energy release per

mole (see Equation 5.2.1 and 5.2.2), nitrogen plays a critical role in increasing the likelihood for breakaway. After the initial oxygen is consumed and leads to a state of 'oxygen starvation', secondary reactions with zirconium and nitrogen begin to occur as shown by Equation 5.2.7 and 5.2.8 for standard temperature and pressure [12].

$$Zr + \frac{1}{2}N_2 \rightarrow ZrN + 365\ kJ \cdot mol^{-1} \tag{5.2.7}$$

$$ZrN + O_2 \rightarrow ZrO_2 + \frac{1}{2}N_2 + 736\ kJ \cdot mol^{-1} \tag{5.2.8}$$

It is believed that due to the large volume increase as the metal reacts to form nitrides and oxides, high local stresses are created, which induce flaking and radial cracks [40]. This effectively strips the sheath's surface of its protective properties. Upon reintroduction of oxidation, the zirconium nitride reacts to form an oxide, which releases more heat.

5.3. Conduction

Conduction is an important phenomenon in the CFD modelling of spent fuel bundles, particularly in the fuel sheath. Conduction is the transfer of energy through a medium due to the vibration of particles and sharing of electrons. It is the mode of heat transfer most commonly associated with solids and is described in its most basic form by Fourier's Law, which states that heat travels in the direction of a temperature gradient.

Conductive heat transfer occurs in the interior of the fuel, although its effect is less pronounced in this model. Conduction is shown explicitly as the rightmost term in the heat transport equation below where *k* represents the conductivity coefficient.

$$\rho C_p \frac{\partial T}{\partial t} + \rho C_p (u \cdot \nabla T) = \mathrm{Q} + \nabla \cdot (k \nabla \mathrm{T}) \tag{5.3.1}$$

Equation 5.3.1 may be used for all phases of a physical system, wherein the conduction coefficient represents the diffusion part of the convection process. However, there are large spaces between particles in gases compared to other phases and which results in a conductivity coefficient, which is significantly less than that of a solid. In effect, the phenomenon typically has a smaller influence on the average temperature of fluids compared to convection as discussed in Section 5.4 (A notable exception is in the near wall boundary layer where fluid movement is constrained by friction). The other terms in the equation represent energy storage, movement and generation, where C_p represents the specific heat capacity at a constant pressure, *u* represents the velocity vector and *Q* represents the heat output (note since the chemical and nuclear decay processes are restricted to the fuel, the *Q* term is effectively zero in the liquid domain). Together, equation 5.3.1 describes the transient conservation of energy and is employed in COMSOL to solve for the temperature variation and conduction in the fluid and solid.

5.4. Convection

During a LOCA in an IFB, heat would escape fuel assemblies primarily via convection [45]. Convection is considered to consist of two phenomena: (1) diffusion, which is the random individual movement of microscopic particles in a fluid, and (2) advection, which is the bulk macroscopic transport of properties through movement of a fluid. In COMSOL, the diffusion process is considered to be mathematically equivalent to the conduction process in solids.

The compressible time-dependent formulation of the Navier-Stokes Equation and continuity equation may be used to solve for natural convection flows arising for a bundle exposed to air. This is shown in Equation 5.4.1 and 5.4.2, wherein *t* represents time, *u* represents the velocity vector, ρ represents the fluid density, *I* is the identity vector, and μ is the fluid's dynamic viscosity [54].

$$\rho \frac{\partial u}{\partial t} + \rho(u \cdot \nabla)u = \nabla \cdot \left[-pI + \mu(\nabla \cdot u + (\nabla \cdot u)^T) - \frac{2}{3}\mu(\nabla \cdot u)I\right] + F \quad (5.4.1)$$

$$\frac{\partial \rho}{\partial t} + \nabla \cdot (\rho u) = 0 \quad (5.4.2)$$

The volume force, *F*, is equal to the force of gravity acting on the fluid and is responsible for driving the natural convection process. The two previous formulations are presented in their time-dependent and compressible form as this facilitates transient, buoyancy-driven flow.

5.5. Radiation

The final method of heat release, radiation, occurs between unobstructed surfaces in a direct proximity to each other. As is standard when dealing with radiative heat transfer problems, it will be assumed that the objects are:

- gray bodies, meaning that their emissive power is independent of the wavelength;
- diffuse radiators, meaning that the emission direction is uninfluenced by the incident angle of the radiation; and
- opaque, meaning that no radiation is transmitted through the object.

To describe this process mathematically, it is convenient to express the incident radiation as a single factor, G_{rad}, and the total emitted radiation (also called the radiosity), *J*, which also includes incident radiation that has been reflected.

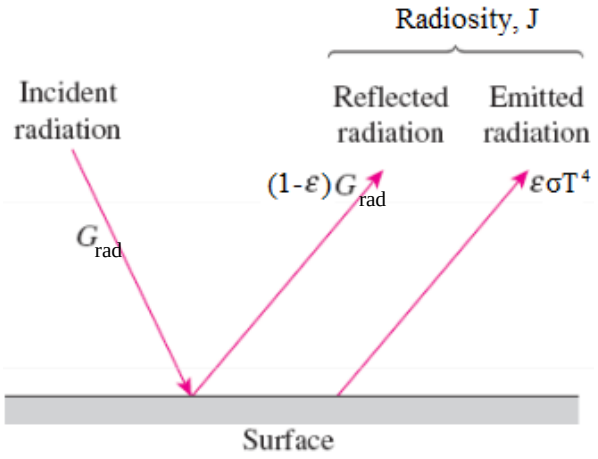

Figure 11: Illustration of the surface-to-surface radiation. Adapted from reference [55].

As illustrated in Figure 11, the net heat flux on the surface per unit area is equal to the incident radiation subtracted by the radiosity. This relation can be expressed in the form of Equation 5.5.1 to determine the net inward radiative heat flux at the surface where *k* is the conduction coefficient, and *σ* represents the Stefan–Boltzmann constant [54].

$$\hat{n} \cdot (k\nabla T) = \varepsilon(G_{rad} - \sigma T^4) \quad (5.5.1)$$

Due to its fourth order dependency on temperature, this mode of heat transfer becomes the dominant form of heat release at high temperatures [16]. For a given surface, the incident radiation G_{rad} is calculated through an integral over the emitting surfaces. It determines how much radiation from a surface is emitted and what proportion of the emission will reach the neighbouring surfaces using a view factor. The view factor is calculated to account for geometric obstructions and the radiation's angle to the receiving point.

The hemicube method [56], which simplifies the direct area integration problem by using projections, may be used to calculate the model's view factor.

5.6. Heat Transfer Coefficient of the Fuel-Sheath Gap

To determine the thermal conductivity of the gap, h_{gap}, it is necessary to understand its physical characteristics. During normal operation, the collapsible sheath comes into contact with the fuel to greatly enhance heat transfer. However, simulations show that the sheath lift off is possible near its end-of-life due to the release of fission gases. The result is a much lower heat transfer coefficient, which is driven primarily by conduction through the gas, but also radiation as shown by Equation 5.6.1 [57] [58].

$$h_{gap} = \frac{k_g}{C(R_f+R_{sh})+t_{gap}+g} + \frac{4\sigma {T_{avg}}^3}{\frac{1}{\varepsilon_{sh}}+\frac{1}{\varepsilon_f}-1} \tag{5.6.1}$$

For an open gap, the conduction term is approximately equal to the coefficient of the gas, k_g, divided by the size of the gap, t_{gap}. This is because the gap thickness of irradiated fuel ranges from approximately 38 µm to 130 µm [59], while the surface roughness of the fuel and sheath, R_f and R_{sh} respectively, and the temperature jump distance, g, are an order of magnitude less. The roughness of the communicating surfaces may be assumed to be 1 µm each while the factor, C, will be taken as 2.5 to be consistent with measurements completed by Ross and Stout at low interfacial pressures [57]. For a discharged fuel bundle with a predominantly fission gas fill and an internal pressure of 488 kPa, the expected jump can be calculated to be about 0.1 µm using relationships from ELOCA [60]. This is clearly negligible when compared to the size of the gap. The conductivity of a gas may be expressed as a function of the relative pressure, P_R, and relative temperature, T_R, as shown in Equation 5.6.2 which has been sourced from ELOCA [60].

$$k_g(T,P) = (k_0 T^s)(1 + aP_R^n) \tag{5.6.2}$$

Where

- $a = 0.51\ T_R^{-2.26}$
- $n = 1+2.5\ T_R^{-6.2}$
- $T_R = T/T_C$
- $P_R = P/P_C$

Here T_C and P_C represent the critical temperature and pressure, respectively. Again, it is assumed there is a purely fission gas fill, which uses an s constant of 0.856, a critical temperature of 281.0 K and a critical pressure of 5.86 MPa. The listed variables have been largely determined from experiments in literature. In particular, Von Ubisch determined the primary variation due to temperature [61] and Lenoir describes the high pressure corrections with respect to the critical pressure and temperature [62].

Assuming no further expansion occurs in the fuel sheath, the conductivity of the gas and therefore the heat transfer coefficient can be simplified into a function of temperature alone using the ideal gas law.

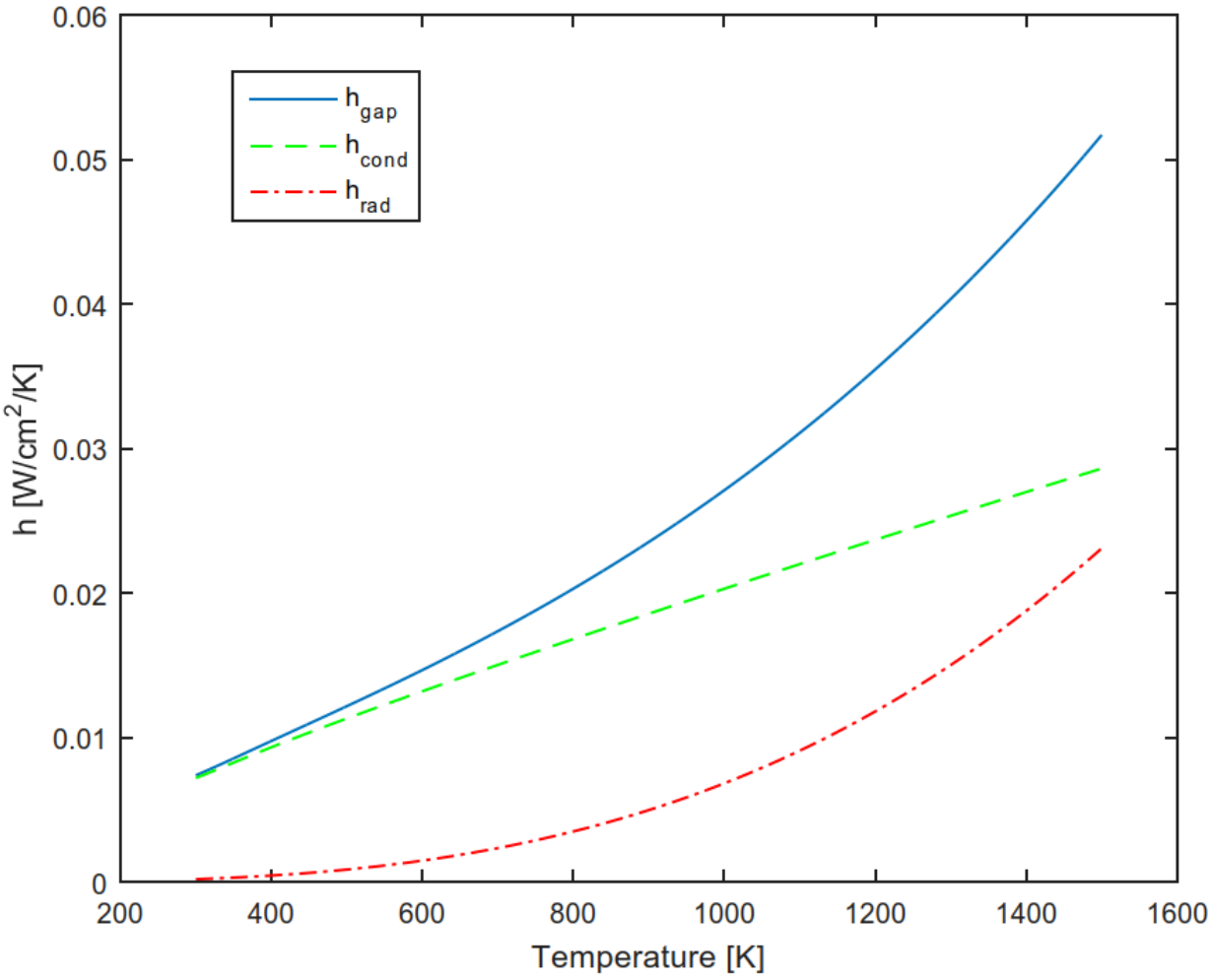

Figure 12: Heat transfer coefficients through the fuel-sheath gap as a function of temperature by radiation (red), conduction (green) and the total (blue) with a 100% fission gas fill and 80 µm gap.

The radiation term on the right has a lesser contribution to heat transfer of the gap. Here σ represents the Stefan Boltzmann constant, ε_{sh} and ε_f represent the emissivity coefficients for the sheath and fuel respectively, and T_{avg} represents the average temperature of the fuel and sheath.

5.7. Mechanical Deformation

A fuel bundle's mechanical integrity has important implications on its ability to retain fission products and disperse heat. Both the fuel matrix and the sheath are considered barriers to protect workers and public, and are enshrined in the nuclear industry's practice of "Defence in Depth." Research has been completed by AECL wherein elements were punctured and heated in air to test the amount of fission product release. They observed insignificant fission product releases (less than 10^{-6} of inventory) after 24 h at 400 °C, 2 h at 600 °C and 2.5 h at 900 °C [43]. The possible dispersion of oxidized uranium particulates, especially given the fuel's damaged state, was concluded to be more concerning. Due to the aforementioned small direct releases expected during the early stages of an accident and inherent complexity of predicting defects and late stage exposure, modelling radioactive releases was not considered in this thesis work.

Instead the effect of physical deformation was examined with respect to its influence on the bundle's heat transfer. In the previously discussed study where bundles were heated in air, the oxidation of the uranium pellets induced extreme ballooning and splitting of the sheath. This was due to oxidation of the sheath and increased temperatures that 1) forms U_3O_8 which is of a lower density than UO_2 and 2) mechanically degrades the fuel and sheath. The diametral increase was over 50% near the artificial defect and around 15% at the ends for a bundle maintained at 400 °C [43]. Such ballooning would limit the amount of flow through the bundle and thereby impair the effectiveness of natural convection. While it is possible that conduction through contacted fuel sheaths could help mitigate temperatures, it is expected the net effect would be negative. Another result of ballooning would be an increase in the size of the fuel-sheath gap and the lowering of its heat transfer coefficient as has been shown in simulations of in-core LOCAs [63]. The influence of the sheath radius on a bundle's cooling was examined in a series of parametric tests in Section 7.7.

The possibility for ballooning was examined without the presence of pre-existing defects. As sheath deformation has been the focus of numerous studies and experiments, literature provides adequate information to predict how fuel would strain when exposed to different temperatures for extended periods. One study conducted by Point Lepreau Nuclear Generating Station examined how long it took for fuel exposed to a steam environment at 600 °C to sustain damage [64]. As explained in their analysis, defects tend to occur anywhere from 15-100% local strains and therefore a 5% average diametral strain was considered a conservative representation of an overstrain failure. The analysis based on the CREEP code showed that spent fuel could be expected to survive for 2-3 days in an environment pressurized at 140 kPa, which is approximately atmospheric conditions. Embrittlement due to oxidation was considered to be the more limiting phenomena in terms of fuel sheath integrity.

Other studies have focused on characterizing the tensile behaviour of Zircaloy-4 tubing and determining when a 'burst', or pressure induced defect in the sheath would occur. AECL conducted experiments wherein Pickering Generating Nuclear Station fuel sheaths were heated at a constant rate until burst [65]. It was found that heating rates had a strong influence on the strains observed and final burst temperature as shown in Figure 13.

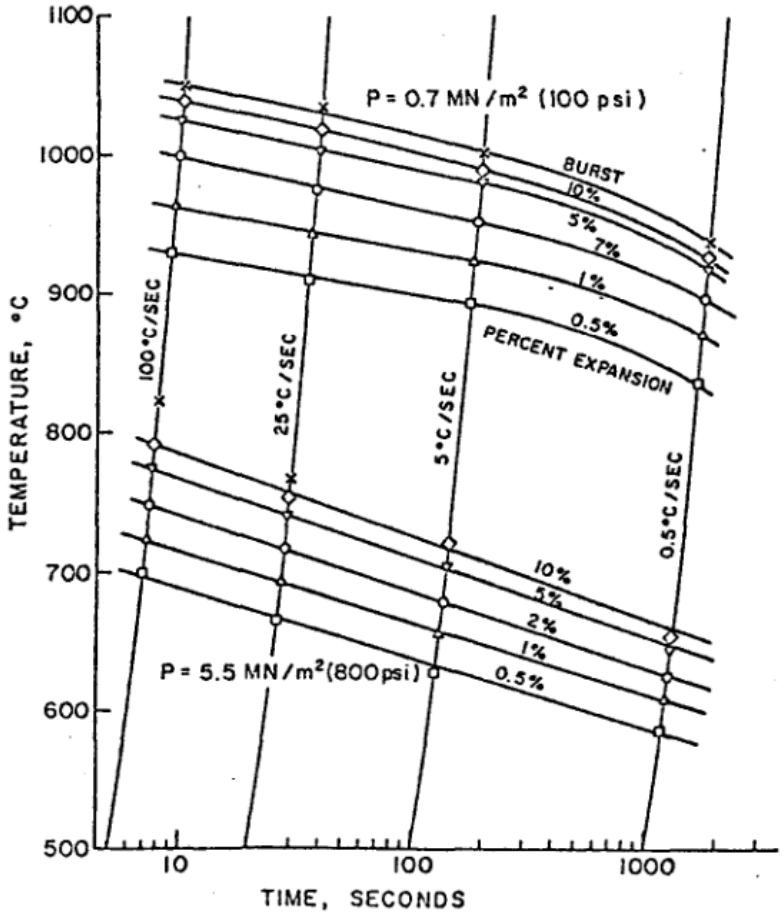

Figure 13: Isostrain and rupture curves as a function of the heating rate for tubes pressurized to 5.5 and 0.7 MPa for Pickering fuel sheaths [65].

The tests focused on fast transients like that would occur after a LOCA and therefore their data are on the order of 10^3 seconds. They noted that once plastic deformation has started, the rate of diametral expansion becomes progressively more rapid until rupture. They also compared their data to PWR and BWR cladding and found Pickering sheaths to be more resilient to deformation and bursting.

Also, data have been published for Indian PHWR cladding [66], which retains physical similarities to its CANDU predecessor. Experiments were conducted with transient heating in a steam atmosphere and elements initially pressurized at 3-70 bars. The burst temperature was determined to be 932 °C and 686 °C for elements heated at 14 °C per second and starting at an initial pressure of 7.91 bar and 50.68 bar, respectively. These results agree with the approximate range determined by AECL [65]. Also, researchers provided comparisons to previous experiments completed in an argon atmosphere. They found that the extent of oxidation strongly affected the maximum circumferential strain achieved and diminished the ductility of Zircaloy. For Zircaloy sheaths reacting in air, this oxidation effect is expected to be magnified.

To supplement the above findings, a theoretical investigation was conducted based on Zirconium sheath behaviour models. While the data required to implement AECL stress-strain models such as those in ELESTRES are not freely available, the MATPRO has disseminated its methods and is drawn upon heavily in the following analysis [67] [68] [69] [70]. The relation between the true effective strain, ε_e, and the true effective stress, σ_e, due to plastic deformation may be modelled according to Equation 5.7.1.

According to the analysis MATPRO is based on, the strain rate values are to be constrained within 10^{-1} to 10^{-5}/s [67].

$$\sigma_e = K\,{\varepsilon_e}^n \left(\frac{\dot{\varepsilon}}{10^{-3}}\right)^m \qquad 5.7.1$$

Here the variables *K*, *n* and *m* represent the strength coefficient, the work hardening exponent and the strain rate sensitivity, all of which have been sourced from various MATPRO volumes for fully annealed isotropic zircaloy-4 cladding. By evaluating Equation 5.7.1 in the limit where the strain rate goes to zero, the relation will have reached its maximum plastic strain. The purpose of the following calculations is to approximate this scenario and solve the 'maximum' strain by selecting the minimum strain rate appropriate for the set of equations. Explained another way, if the strain rate has dropped to 10^{-5} /s and strain rate is assumed to continually decrease, then future effective strains will be less than an additional 0.036 per hour. Depending on the amount of time a bundle is exposed and how long it takes to reach the assumed strain rate, the implications of such low strain rates may be negligible.

As shown by the MATPRO correlation [68] and the more recently conducted analysis by the Pacific Northwest National Laboratory (PNNL) [70] in Figure 14, the strain rate sensitivity is primarily a function of temperature.

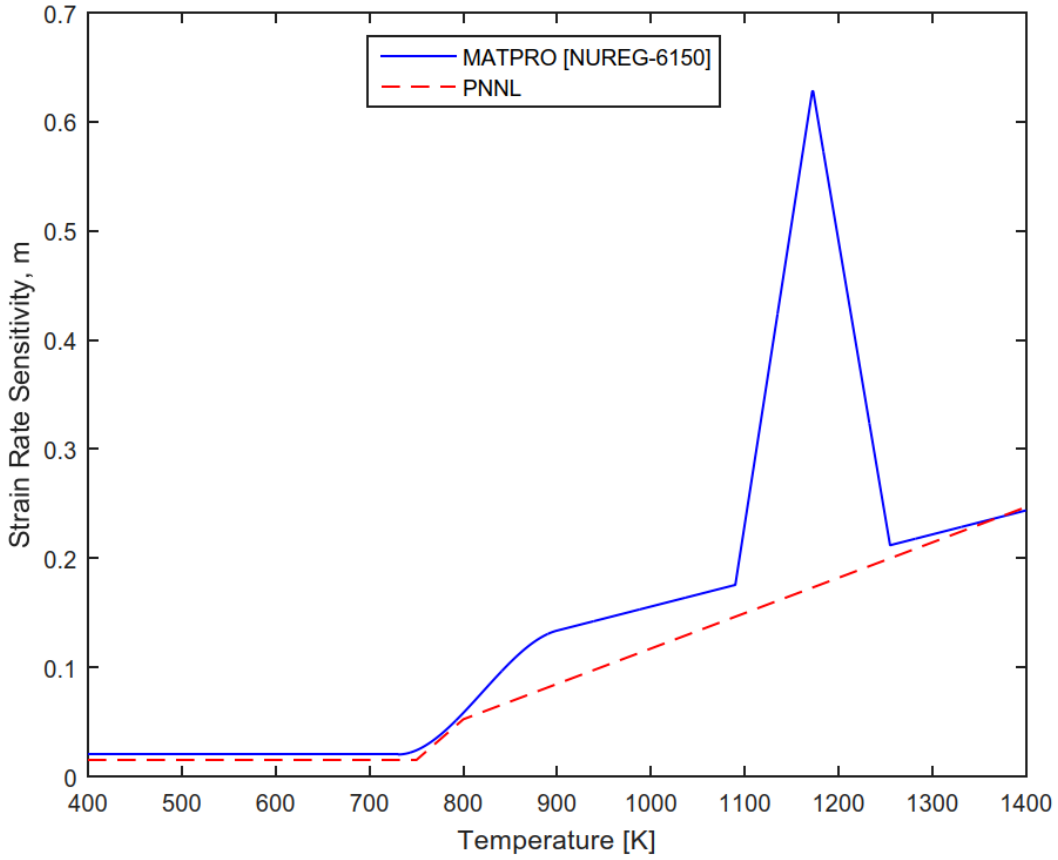

Figure 14: Strain rate sensitivity as a function of temperature (in Kelvin) provided by MATPRO NUREG-6150 [68] and PNNL [70]. The strain rate, $\dot{\varepsilon}$, in the MATPRO NUREG 6150 correlation has been assumed to be equal to its minimum value, 10^{-5}.

A peak is observable between 1090 K and 1255 K in the MATPRO data, which corresponds to the temperature range in which the alpha to beta transition in zircaloy occurs. The height of the peak is

affected by the strain rate, however PNNL did not include this dependency in their revised model because the effect 'was not observed to be large' [70].

The strength coefficient, *K*, is shown by the log plot in Figure 15 for MATPRO and its revised model by PNNL for Zircaloy-4.

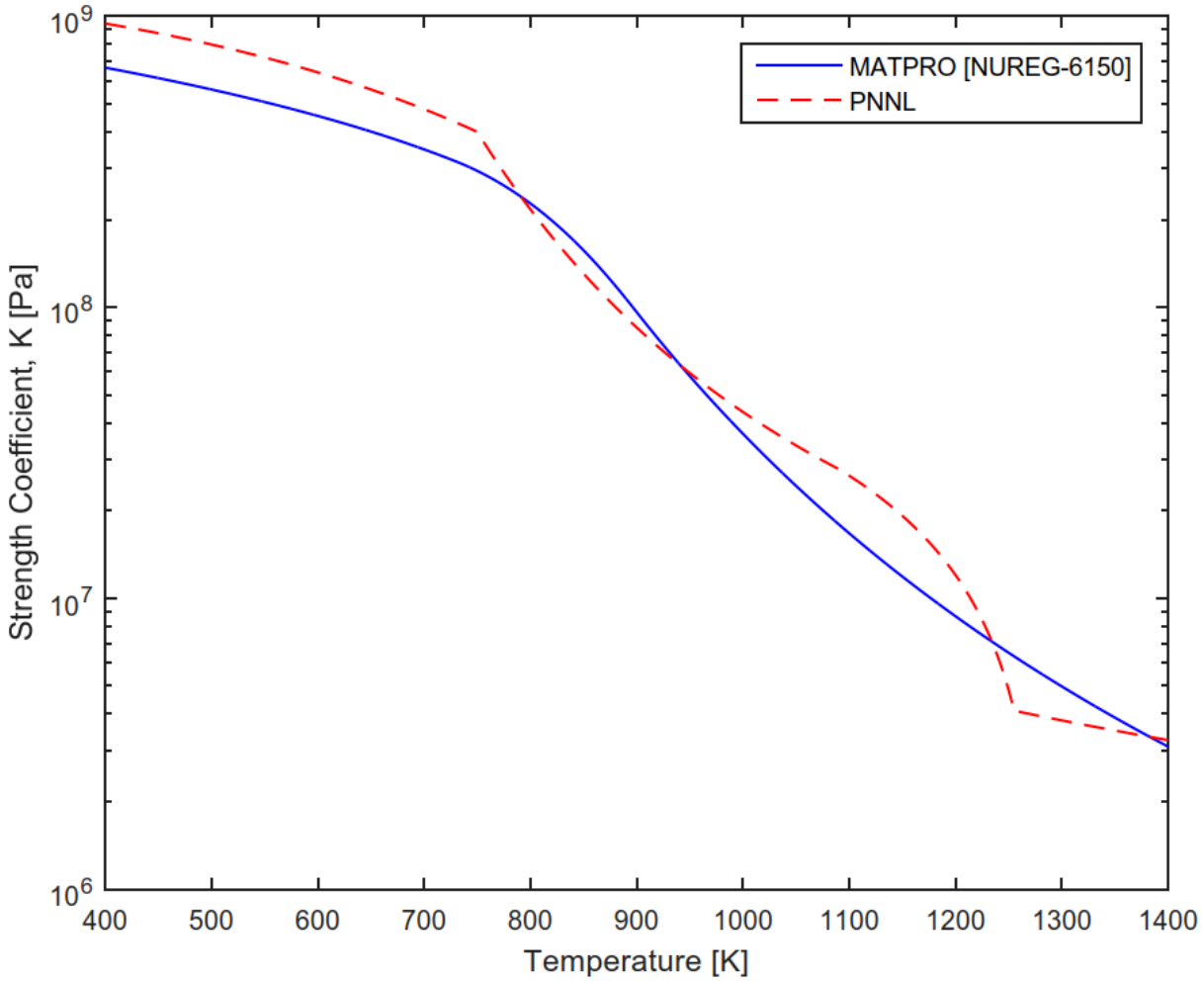

Figure 15: Correlations for the strength coefficient, K, provided by MATPRO report NUREG-6150 [68] and the Pacific Northwest National Laboratory (PNNL) [70] as a function of temperature only.

In general, good agreement is observed between the two correlations. As anticipated, the strength of the metal diminishes as it becomes hotter and approaches its melting point. Note that dependencies on the cold work and fluence have been omitted due to a lack of data in CANDU spent fuel and the uncertainties associated with extrapolating American PWR-based models.

While the values for the strain rate sensitivity and strength coefficient are primarily functions of temperature, the work hardening coefficient is sensitive to the strain as shown in Figure 16 and will be discussed.

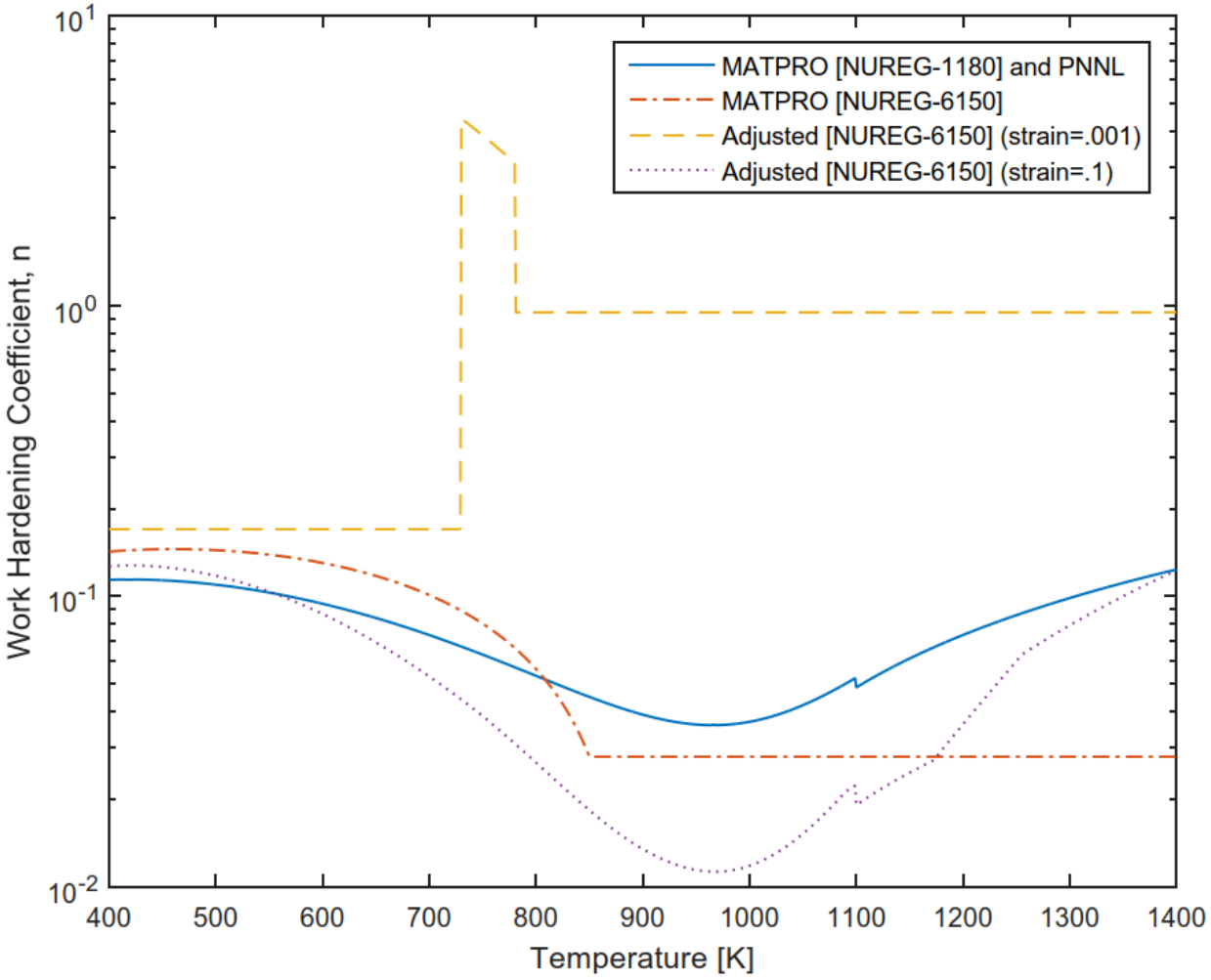

Figure 16: Work hardening coefficient, n, for the various versions of MATPRO and the adjusted values recommended by NUREG-6150 [68] for strains less than $\frac{n^2}{(1+m)}$. *The relation recommended by the PNNL [70] is equal to that of NUREG-1180 [69].*

According to the NUREG-6150 version of MATPRO [68], the work hardening coefficient should be replaced by a larger adjusted coefficient, n', when the condition $\varepsilon < \frac{n^2}{(1+m)}$ is satisfied.

$$n' = \min\left(ANL, \frac{n^2}{(1+m)\varepsilon} \right) \qquad 5.7.2$$

Little information is given about the ANL in MATPRO documentation aside than its form as a function of temperature. Although no adjustment factor is recommended by PNNL [70], the base work hardening coefficient relation is unchanged compared to the earlier MATPRO correlations after ignoring effects of fast fluence. Previous versions of MATPRO in NUREG-1180 show a more simplified version of the work hardening coefficient [69]. The work hardening coefficient has been plotted as a function of temperature for all the MATPRO sources in Figure 16. Plots for the adjusted work hardening coefficient have been included for strains of 10^{-1} and 10^{-3} following the methodology prescribed by NUREG-6150 [68]. There is a clear contrast between the values of the adjusted coefficient at strains on the order of 10^{-3} when n' is derived from the ANL results. However, the adjusted coefficient for strains on the order of

10^{-1} were similar in value to the unadjusted values. The values of the strength coefficient, strain hardening coefficient and strain rate sensitivity proposed by the MATPRO report, NUREG-6150, and those derived by PNNL will be analyzed in this stress strain problem.

Referring back to the Equation 5.7.1, the effective stress is calculated by adding in quadrature the three different components [67] [68]: (1) axial stress, σ_z, (2) circumferential or hoop stress, σ_θ, and (3) radial stress, σ_r.

$$\sigma_e = \sqrt{A_{1S}(\sigma_z - \sigma_\theta)^2 + A_{2S}(\sigma_\theta - \sigma_r)^2 + A_{3S}(\sigma_r - \sigma_z)^2} \quad 5.7.3$$

The symbols A_{1S}, A_{2S} and A_{3S} represent the anisotropic factors of stress in each direction. While the fuel is not in contact with the sheath, the hoop stress on an element may be described by Equation 5.7.4, where ΔP describes the pressure difference between the internal fill gas and the bundle's environment [67].

$$\sigma_\theta = \frac{\Delta P\, r_0}{w} \quad 5.7.4$$

This relation is considered appropriate for thin-walled cylinders where the radius, r_0, is at least ten times its thickness, w [71]. The internal pressure can be calculated in Equation 5.7.5 by assuming that the pellet experiences no thermal expansion.

$$\Delta P = P_{int} \frac{T}{T_0} \frac{r_{int}^2 - r_p^2}{\exp(2\varepsilon_\theta)\, r_{int}^2 - r_p^2} - P_a \quad 5.7.5$$

Using the ideal gas law, the change in internal pressure from the starting equilibrium state, P_{int}, and starting temperature, T_0, is a function of the volume of the pellet-sheath gap. The internal volume resulting from pellet chamfers, dishes and axial gaps has been neglected and instead the pressure is calculated through only the pellet radius, r_p, and sheath's internal diameter, r_{int}.

The axial and radial stress for a pressurized cylinder with endcaps may be expressed in a similar form to the hoop stress, as shown by Equations 5.7.6 and 5.7.7 [67].

$$\sigma_z = \frac{\Delta P\, r_0}{2w} = \frac{\sigma_\theta}{2} \quad 5.7.6$$

$$\sigma_r \approx -\frac{\Delta P}{2} = -\frac{\sigma_\theta w}{2r_0} \quad 5.7.7$$

To simplify matters, it will be assumed that the Zircaloy is isotropic and maintains this property throughout the deformation process. Therefore, the anisotropic stress factors will be equal ($A_{1S} = A_{2S} = A_{3S} = \frac{1}{2}$ [71]) and the deviation from isotropy, δ, discussed in MATPRO [68] for closed tube burst tests is zero. More complicated formulations of the anisotropy coefficients are also available in MATPRO, but are considered unnecessary for this calculation to CANDU spent fuel.

Since the ratio of the sheath's thickness to its radius does not change significantly, the effective stress is roughly proportional to the hoop stress.

$$\sigma_e = \frac{\sigma_\theta}{\sqrt{2}} \sqrt{\left(\frac{1}{2}\right)^2 + \left(1 - \frac{w}{2r_0}\right)^2 + \left(\frac{1}{2} - \frac{w}{2r_0}\right)^2} \quad 5.7.8$$

Similarly, manipulations are necessary to transform the effective strain into its components. This is shown by Equation 5.7.9 for plastic deformations over small time steps [68].

$$d\varepsilon_\theta = \frac{d\varepsilon_e}{\sigma_e}(\sigma_\theta(A_{1E} + A_{3E}) - \sigma_z A_{1E} - \sigma_r A_{3E}) \quad 5.7.9$$

The variables A_{1E}, A_{2E} and A_{3E} represent the anisotropic factors of strain and will be assumed to also behave isotropically. By substituting Equations 5.7.5 - 5.7.7 into Equation 5.7.8 and integrating over time, it is found that the circumferential strain is approximately a linear function of the effective strain as shown by Equation 5.7.10.

$$\varepsilon_\theta = \varepsilon_e \frac{\sqrt{2}\left(\frac{3}{4}-\frac{w}{4r_0}\right)}{\sqrt{\left(\frac{1}{2}\right)^2+\left(1-\frac{w}{2r_0}\right)^2+\left(\frac{1}{2}-\frac{w}{2r_0}\right)^2}} \quad 5.7.10$$

This integral over time was solved using the initial condition that $\varepsilon_\theta = \varepsilon_e = 0$ and assuming that the ratio of the sheath's thickness to radius is effectively constant during expansion. Therefore, it will not be valid for large strains and instead the relation in Equation 5.7.9 should be used in conjunction with time stepping.

The plastic deformation may then be predicted for spent fuel after a loss of coolant by assuming a given strain rate in Equation 5.7.1 and substituting in for the stress-strain relations found in Equations 5.7.8 and 5.7.10. To solve the strain as a nonlinear function of temperature, fzero algorithm in MATLAB was used to numerically find the minimum solution. This method uses a combination of bisection, secant, and inverse quadratic interpolation methods and was originally developed by T. Dekker [72]. If the effective strain calculated is less than the $n^2/(1+m)$ with the MATPRO NUREG-6150 data, the solution with the adjusted strain hardening coefficient, n', is instead used.

For elastic stresses below the yield stress of the material, Hooke's law in Equation 5.7.11 is applied where E represents Young's Modulus. The value for the Young's modulus is based on the temperature dependent function found in the AECL code ELESTRES [73].

$$\sigma = E\varepsilon \quad 5.7.11$$

The transition from the elastic to the plastic deformation regions is defined to be the nonzero intersection of the curves. Therefore, the strain experienced by the sheath can be simply taken as the maximum of the plastic and elastic deformation relations.

The strain results for a given strain rate with the MATPRO NUREG-6150 material properties data are shown in Figure 17. Depending on the timeframe of interest, further strains may be assumed to not significantly change the system once the strain rate falls below a certain level. This scoping of the solution is justified as an accident will not last indefinitely.

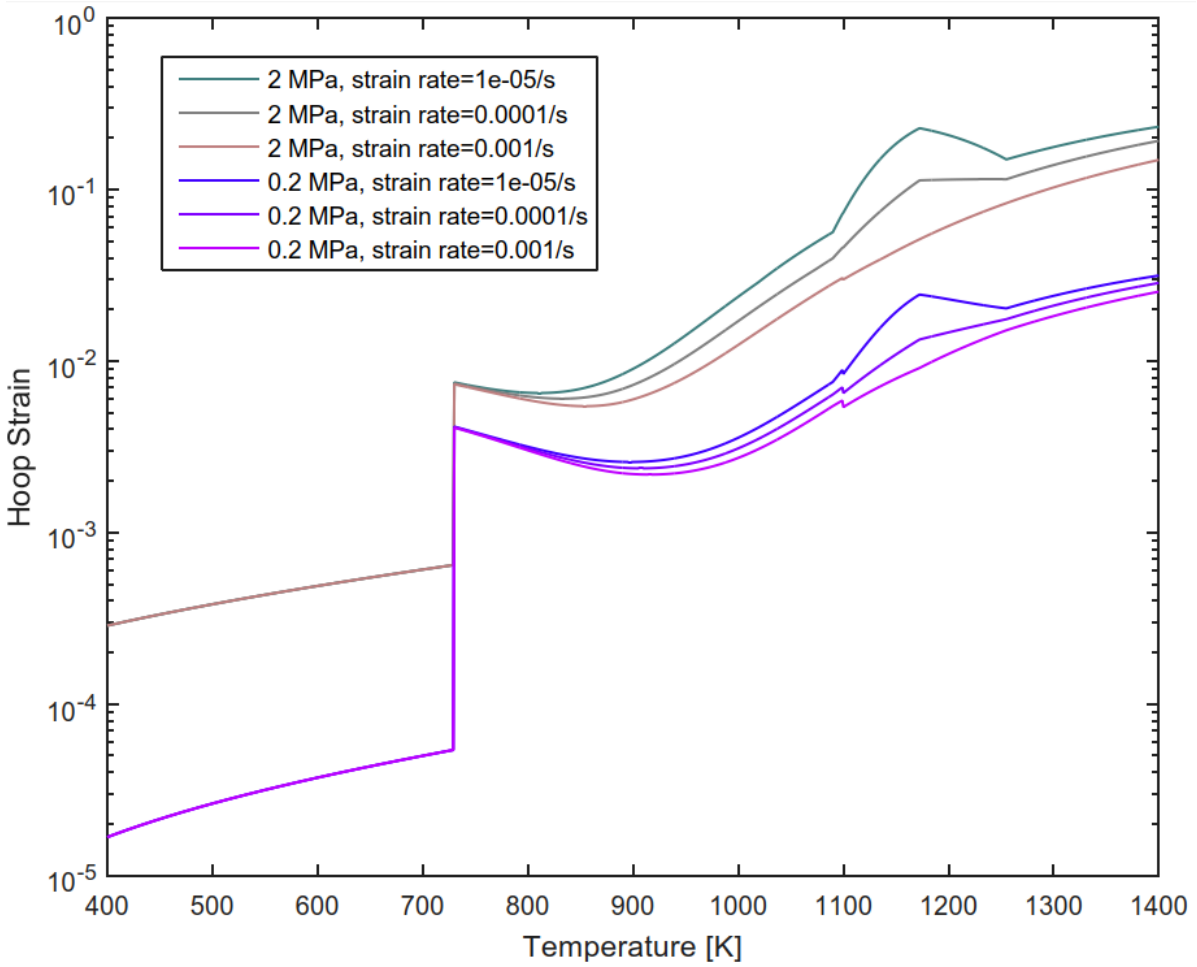

Figure 17: Hoop strains due to the fuel's internal pressure when the strain rate has diminished to between 10^{-3} and 10^{-5}.

The initial pressures assumed before the temperature excursion is 2 MPa and 0.2 MPa, which are meant to represent the maximum and minimum expected in spent fuel. The high-pressure estimate was based on measurements for fuel in CANDU derivative-PHWRs in India, which were found to reach up to 2.1-2.7 MPa for burn-ups up to 15,000 MWd/tU [74]. Note that this is almost more than three times the typical burn-up of fuel discharged from CANDU reactors and therefore is expected to serve as an appropriate upper bound.

The lower bound is assumed to be twice that of the initial atmospheric fill and in alignment with tests at the Kakrapar Atomic Power Station for fuel with a burn-up of 387 MWd/tU [74]. Post irradiation examinations of Romanian CANDU fuel elements were found to have internal pressures of 0.488 MPa [75], which aligns with the maximum and minimum proposed here. The strain rates were selected at the lower bound of their range based on the assertion that MATPRO properties were valid for strain rates between 10^{-1} and 10^{-5} /s [67]. Many versions of the MATPRO library [68] [69] do not mention this, thus it is possible that the limit is no longer applicable and Equation 5.7.1 would be valid with even lower strain rates.

The curves presented in Figure 17 show a number of unique features and transition points. At approximately 728 K, there is a departure from the elastic to plastic deformation regime with the adjusted value of the strain hardening coefficient based on the ANL value and then to that based on $n^2/(1+m)$. Since there is not a significant physical change in the material known to be associated with this

temperature, the transition is clearly an exaggeration of the behaviour expected. A smoother transfer in this region is expected as shown in Figure 18 when using the data from the PNNL [70].

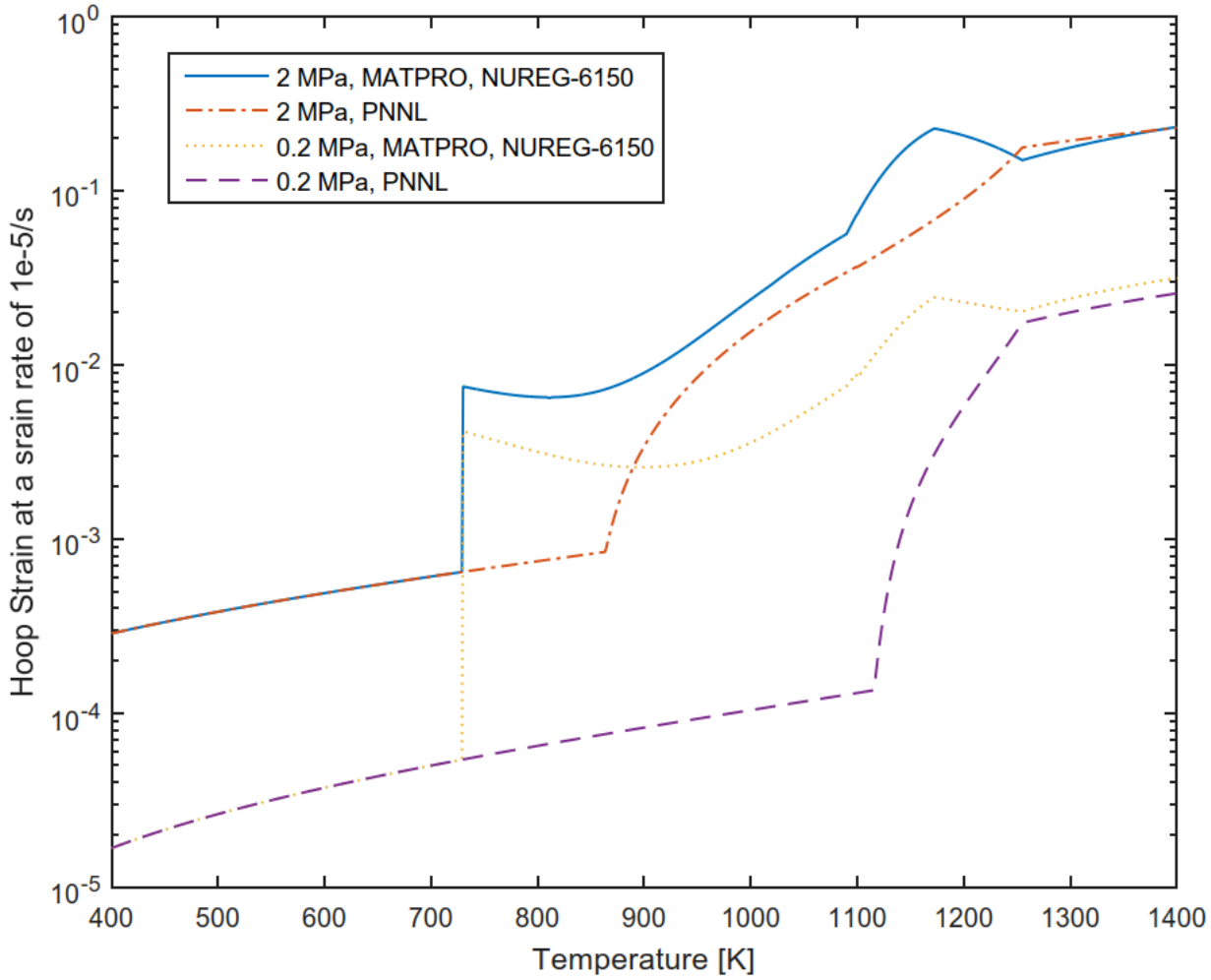

Figure 18: Comparison of the predicted hoop strain between PNNL [70] and MATPRO NUREG-6150 [68] data when a strain rate of 10^{-5}/s has been reached

There is also a peak between 1093 K and 1253 K predicted in the MATPRO report NUREG-6150 based data, which corresponds to the temperature range at which zircaloy transitions from the alpha to beta phase. This peak is not shared in the PNNL predicted strains and is a direct result of the differences in the strain sensitivity curve as previously shown in Figure 14. However, there are uncertainties as to whether the MATPRO report NUREG-6150 or PNNL data are more applicable to CANDU fuel sheaths. Although both behaviours shown in this region appear plausible, these data in NUREG-6150 have been focused on since it produces more conservative results.

By assuming the strain rate continually decreases, the time to reach the 'max' strains, Δt, shown in Figure 17 data can be estimated by Equation 5.7.12.

$$\Delta t = \sum_{i=1}^{i \to n} \frac{\varepsilon_i - \varepsilon_{i-1}}{\dot{\varepsilon}_i} \qquad 5.7.12$$

It is assumed that $\varepsilon_0 = 0$ and the strain, ε_i corresponds to the deformation predicted at the i^{th} largest strain rate, $\dot{\varepsilon}_i$. The equation estimates the time elapsed through dividing the incremental strain by the strain rate for each step, and then sums them. Increasing the number of steps, n, will increase the accuracy of the elapsed time prediction.

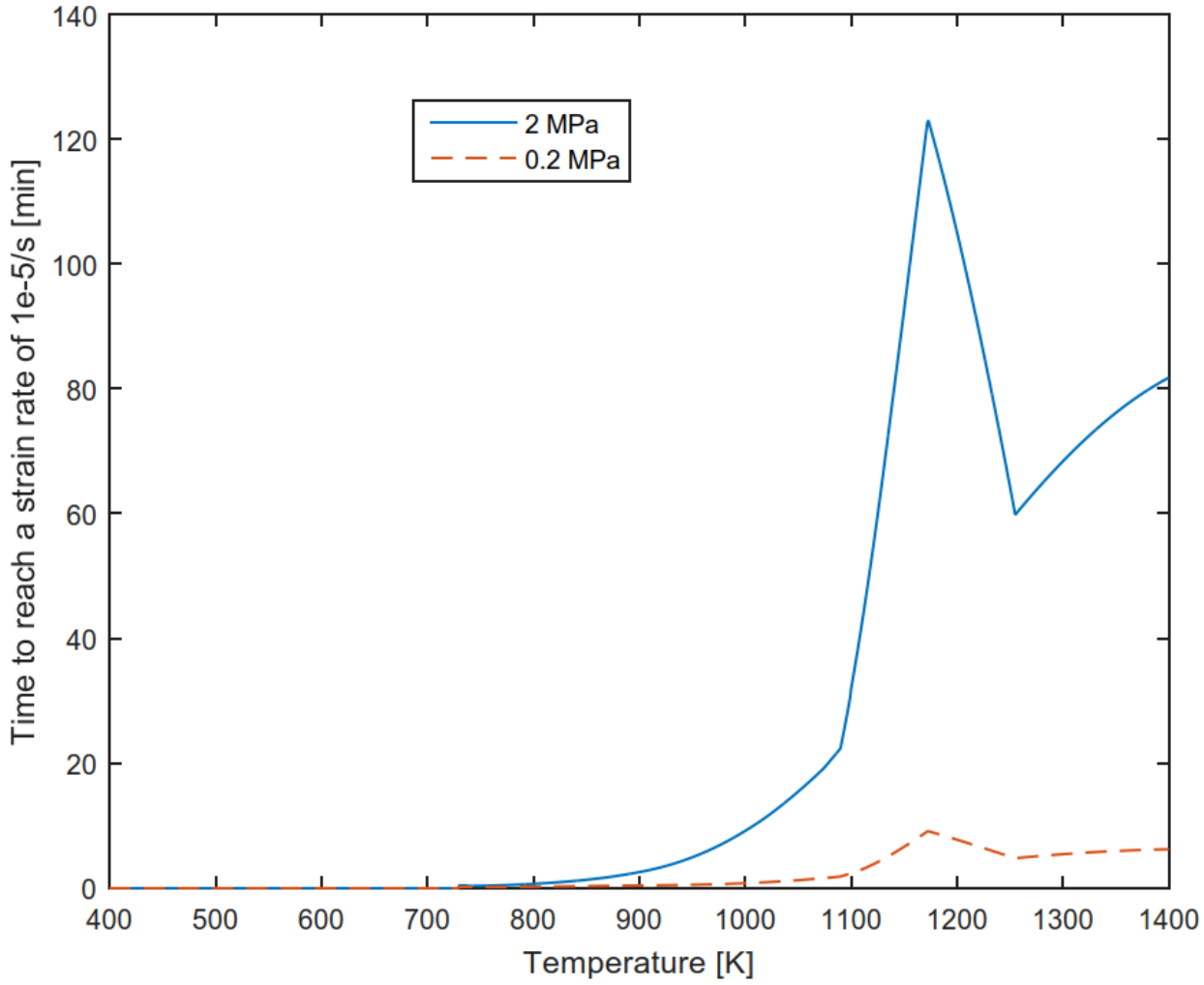

Figure 19: Time elapsed to reach a strain rate of 10^{-5}/ s for the MATPRO report NUREG-6150 material properties.

The time for the fuel sheath to reach a strain rate of 10^{-5}/ s has been approximated in Figure 19 using Equation 5.7.12 for $n = 3$ steps. The response in the elastic region is instantaneous, however the plastic deformation of the sheath is predicted to take several minutes before settling to a strain rate of 10^{-5}/ s for the 0.2 MPa case and hours for the 2 MPa internal pressure case at high temperatures.

The results of the analysis have been summarized in Table 4. The strain was sampled at 873 K (600 °C) to predict the likelihood of overstrain before embrittlement and again at 800 °C to demonstrate how a rise in temperature causes an expansion of the sheath. For the even highly pressurized elements at 873 K, the sheaths reached diametral strains of less than 1%, which would not be considered indicative of a failure. Note that the analysis predicts only the plastic deformations due to strain rates greater than or equal to 10^{-5}/s, and thus does not preclude the possibility of further expansion due to creep.

As previously discussed [64], strain rates of 5% may be used as a failure criteria threshold in safety analysis of unoxidized zircaloy. However according to the ELOCA theory manual [60], macroscopic cracks begin to form and grow when the diametral strain is equal to about 2% for oxygen embrittled surfaces. This then provides a pathway for oxygen to penetrate the sheath. Since the fuel will be expected to react in air, the 2% sheath strain was considered to better represent when a defect could more

realistically be expected. Both the temperature at which the 2% and 5% strains are reached was used to relate the temperature and pressure to the strain failure criteria of an element.

Table 4: Summary of stress-strain calculations. Strain calculations were carried out up to 1400 K (1127 °C).

Material Data Properties	Initial Internal Pressure [MPa]	Diametral Strain at a 10^{-5}/s strain rate at 873 K (600°C) [%]	Diametral Strain at a 10^{-5}/s strain rate at 1073 K (800°C) [%]	Temperature to cause a 2% diametral strain at a 10^{-5}/s strain rate [K]	Temperature to cause 5% diametral strain at a 10^{-5}/s strain rate [K]
MATPRO NUREG-6150	2	0.8717	5.62	983	1075
PNNL	2	0.1623	3.44	1011	1121
MATPRO NUREG-6150	0.2	0.2619	0.6498	1153	>1400
PNNL	0.2	7.744×10^{-3}	0.0123	1299	>1400

As shown for the highly pressurized spent fuel, defects could be produced at temperatures as low as 983 – 1011 K (710 – 738 °C). However, it should be reiterated that such high pressures are not expected to be observed in the IFB. For low pressure fuel (much closer to what is realistically expected), failures are predicted to occur between 1153 – 1299 K (880 – 1026 °C). This compares favourably to the 900 °C temperatures at which the onset of significant fission product release is stated to occur in a USNRC *Technical Study of Spent Fuel Pool Accident Risks at Decommissioning Nuclear Power Plants* [76].

Based on the discussed research, it is not completely certain how much ballooning would realistically occur and adversely impact the progression of a LOCA in an IFB. The temperature of the fuel is a critical parameter for determining the amount of expansion and the integrity of the sheath, and presently remains unknown. In steam environments, experiments and simulations suggest that fuel integrity can be maintained for potentially days below 873 K for typical burn-ups. There are also a couple abnormal cases where sheath expansion and potential oxidation of the uranium oxide pellets would be of an elevated concern in freshly discharged fuel: 1) fuel with high internal pressures due to fission gas release and 2) defected fuel. Fortunately, this would only apply to a small fraction of bundles in an IFB. The overarching conclusion is that fuel deformation is a complex phenomenon that, similar to breakaway oxidation, will become increasingly pertinent at high fuel temperatures and has the potential to further aggravate accident conditions. As shown, the initial internal pressure and the temperature can be used to directly determine when the fuel would fail and serve as a simple failure criterion. Better quality information on the internal pressures, fluence and material properties of CANDU irradiated fuel is needed to enhance the accuracy and reliability of predictions. If a significant number of bundles in the bay are predicted to defect, adjustments may be necessary to more accurately account for ballooning and its effect on the heat transfer in IFBs.

6. THEORETICAL TOOLS BACKGROUND

A brief description of the tools and theory used in the body of the thesis is provided in the following section.

6.1. Multiphysics Finite Element Analysis Platforms

Numerical simulation has become an indispensable asset for safety analysis and efficient design in the nuclear industry. Compared to experimental results, simulations offer distinct advantages in terms of worker safety, costs and predictive power over a variety of initial conditions [77]. Multiphysics platforms are becoming a more common way to leverage the advantages of numerical simulation. COMSOL Multiphysics is a simulation environment that is designed to model interacting physical phenomena through the use of a finite element analysis (FEA) solver. This method uses a numerical approach for finding the approximate solutions to boundary value problems. This is useful for systems with complex geometries described by partial differential equations that cannot be solved analytically.

FEA is performed by generating a grid-like representation of the geometry composed of many nodes connected by elements to create a mesh. Afterward, the boundary conditions such as forces can be applied at nodes between the elements to reproduce situations of interest and predict their behaviour over time. The solution is calculated from global matrix equations via either a direct or iterative solver. Post-processing then is used to retrieve information from the model and present the results in an easily understandable manner.

COMSOL Multiphysics is a commercial software package that has a number of features meant to enhance its usability and robustness. It has built-in material databases, automatic mesh generation, a geometry builder, the ability to import CAD drawings and options for visualization of results. However, where COMSOL differentiates itself from other fully developed FEA platforms is in its versatility. Physics models that are common in science and engineering, such as CFDs, are provided and offer predefined functions to streamline analysis. The ability to implement arbitrary equations, differential or integral, also greatly increases the amount of flexibility in modelling.

Multiphysics FEA platforms are becoming a more important tool for regulators and researchers in nuclear. Traditionally, simulation of reactors and fuel was accomplished by patching multiple existing domain-specific codes together and coordinating their finite difference outputs in a modular framework [78]. The use of multiphysics software simplifies the integration process and allows easy coupling between phenomena and modification of existing geometries. In effect, implementation times for developers can be greatly diminished. This concept has been the driving force behind the MOOSE-BISON-MARMOT project to create nuclear-focused multiphysics FEA platforms by the United States Department Nuclear Energy Fuels Modelling and Simulation (NEAMS). COMSOL specifically is used at the CNSC and academic institutions specializing in nuclear research across Canada.

6.2. Uncertainty Analysis

There are many types of errors in conventional CFD calculations, many of which can be generalized to other types of models. Inclusion of error ranges provides a valuable tool for interpretation of results and numerous reputable organizations have released detailed standards for quantifying uncertainty. However, a discussion of errors is frequently omitted in literature, especially if there is no experiment for direct comparison [79]. This work refers to uncertainty as the range, more or less than the predicted output, within which the true answer likely falls. The chosen definition is consistent with that published by the American Society of Mechanical Engineers [80], but it is known to vary between standards [79] [81]. The uncertainty in a simulation is from three discrete components (1) error due to modelling assumptions, (2) error due to numerical solution and (3) error due to inaccurate input parameters [80] .

Although many of the components of simulation uncertainty are intuitive, it will be valuable to further explain and clarify the sources of these errors. Error due to modelling assumptions includes approximations in boundary conditions and geometric simplifications. Modelling errors need to be addressed through validation by comparison to experiments for a specific set of validation variables [79].

The error in the numerical solution is quantified in the verification process. Numerical errors include those arising due to computer round-off, iterative convergence error, spatial discretization and temporal discretization error. The errors due to input parameters may be due to the stochastic nature of a variable or a lack of knowledge. The uncertainty analysis in this work will be conducted through verification and sensitivity tests, as again a proper validation exercise remains impossible without experimental data.

The two key steps to model verification are: (1) code verification and (2) solution verification [80]. The code verification step ensures the code is mistake-free and solves the intended equations properly. The recommended manner of achieving this is by benchmarking against a precise analytical solution. However, when exact analytical solutions are unavailable, code verification can also be performed by code-code comparisons. As a step towards this goal, the CFD models presented in this thesis have been compared either against models in literature or analytical models.

The other step, solution verification, primarily regards quantification of the discretization errors and arises from limited computational resources. Often it is assumed that round-off and iteration errors are negligible. For the present work, the CFDs have been considered converged when their relative error falls below COMSOL's default value of 0.001. In the finite difference model, simulations were repeated until the variation was less than 0.1 K in the output temperature. The majority of models shown in the following section were not complex enough to challenge the modelling hardware and force the use of coarse meshes that introduce significant numerical errors. The only potential exception was identified as the 3D laminar model presented in Section 8.2, where a Richardson's extrapolation [82] has been performed to estimate the error's magnitude. As shown in the analysis, numerical errors are well below one Kelvin.

Rather than focusing on errors in the numerical solution (which are small) or errors from modelling assumptions (which cannot be addressed without experiments), more attention should be placed on uncertainties arising due to the input parameters. Accordingly, sensitivity studies have been created for variables such as the fill gas and gap size. In scenarios where the input dataset has not been fully characterized, determining a mean and uncertainty range for the outputs would require further assumptions and would ultimately end in poorly substantiated estimations. Due to this complication, the use of error bars has been forgone because the total uncertainty on an output cannot be adequately quantified by simulation alone. Instead where limited data exist, bounding analyses have been performed.

7. INDIVIDUAL FUEL BUNDLE ANALYSIS

7.1. Model Description

A 2D CFD has been developed on the COMSOL platform to study the rise in temperature of a single fuel bundle over time. As discussed in Section 6.1, COMSOL Multiphysics is FEA software that is optimized to deal with coupled phenomena; version 5.3 has been used in the development of the model for this thesis. The model was created using the Non-isothermal Flow Multiphysics option in COMSOL. The fuel bundle was setup to replicate the scenario in which a rapid drainage in the IFB would expose a single bundle on a rack. This is effectively equivalent to a bundle being removed from the water and suspended in a well-ventilated environment. Decay heats from 1 kW to 4 kW were chosen to represent bundles with a discharge time ranging from two weeks to two days, respectively [48]. The ambient temperature of the bundle's surroundings (to which it radiates), the temperature of the replenishing fluid at the inlets, and the initial temperature of the fluid and sheath were all set to the maximum normal operating temperature of an IFB (305 K) [17].

7.2. Geometry

The cross-section of a standard 37-element bundle, disregarding the endcaps, bearing pads and spacer pads, was taken as the geometry for the model as shown in Figure 20. Selecting this simplified geometry assumes no heat transfer occurs along the bundle's length, allows for direct comparisons to Krasnaj [16], and greatly decreases the computational demands of the model.

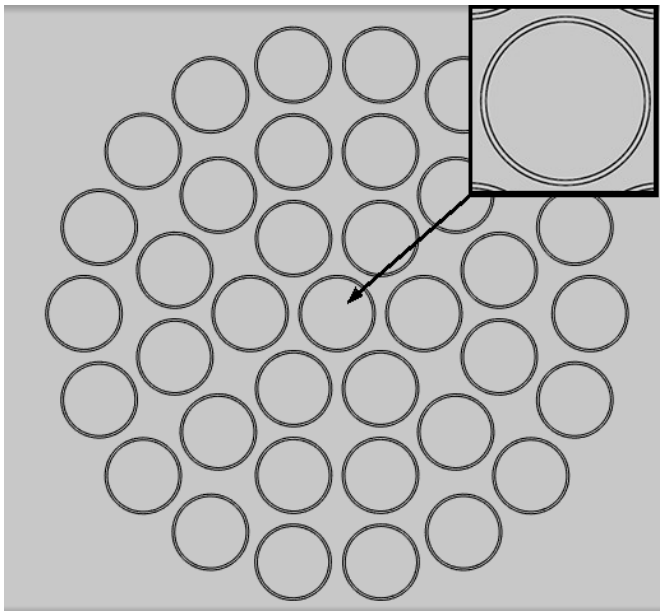

Figure 20: Geometry of the fuel bundle and close-up of an individual element is shown [83].

The dimensions of the sheath thickness, element pitch, and radius were based on publicly available sources [24] [59] [84]. All dimensions remained fixed during the modelling. The bundle was centred inside of a 200 mm by 200 mm square control volume, which was split in half by a thin line. The main purpose of the cut was to construct a symmetrical mesh which would thereby improve the solution's stability. Modelling half the bundle using symmetry was tested to reduce the computational demands, but not implemented in the final model.

7.3. Materials

The material properties for the Zircaloy-4 alloy cladding and the ceramic uranium dioxide fuel were based on relationships from the MATPRO [85] and the IAEA thermophysical properties database [86], common libraries used in nuclear accident codes. The property values for the conductivity, specific heat capacity, density, emissivity and burn-up of uranium oxide (UO_2) are summarized in Table 5.

Table 5: Summary of uranium dioxide properties used and assumed in the 2D transient spent fuel model.

UO_2 Property	Source	Expression
Burnup	[24]	7.29 [MWd/kgU]
Specific Heat Capacity	[85]	$\frac{302.27\left(\frac{548.68}{T}\right)^2 e^{\frac{548.68}{T}}}{\left(e^{\frac{548.68}{T}}-1\right)^2} + \frac{8.741\text{x}10^7(18531.7)e^{-\frac{18531}{T}}}{T^2} + 2(8.463 \text{ x } 10^{-3})T$ [J/(kg K)]
Emissivity (Unoxidized)	[35]	$0.7856+1.5263 \text{ x } 10^{-5}$ T [K]
Density	[24]	$10.6 \text{ x } 10^{-3}$ [kg/m^3]
Conductivity	[86]	$.013e^{0.00188T} + \frac{1}{.1148+.0035B+2.475 \text{ x } 10^{-4}(1-0.00333B)T}$ [W/(m K)]

As shown, most of these properties depend on temperature, *T*, while the conductivity of the fuel also depends on the burnup, *B.* A similar table for the property of the zirconium is provided in Table 14 of the Appendix. The surrounding fluid in the modelled scenario was air and based on the COMSOL material library.

7.4. Boundary Conditions

Finite Element Analysis relies on the specification of boundary conditions to form a matrix and solves for the discrete points specified by the mesh. The Heat Transfer and CFD packages in COMSOL offer typical boundary conditions for scenarios that commonly arise in thermal-hydraulic analysis. The following section provides a brief outline of the boundary conditions applied, starting with those on the interior of the fuel and looking outward.

Inside the elements, the pellets were defined as a volumetric heat source. Each ring's power output normalized to follow the same relative distribution as exhibited during operation [84] as shown in Table 6.

Table 6: Relative radial power output of fuel in each ring of the bundle. A relative power of 1.000 corresponds to an element which emits 1/37th of the total power [84].

Inner Pitch Circle	Relative Power
Centre Pitch	0.8218
Inner Pitch	0.8538
Middle Pitch	0.9308
Outside Pitch	1.1048

This effect is from the thermal neutron flux depression that occurs due to shielding of the bundle's interior elements. A bundle with a thermal power of 2 kW was used for the steady-state tests, which corresponds to a typical bundle that is approximately four days removed from the reactor [11].

Since the decay heat is generated inside the fuel, it is necessary to model the heat transfer process across the fuel-sheath gap. For this purpose, the thin layer option was used to represent the heat transfer coefficient of the gap, h_{gap}, as shown by Equation 7.4.1.

$$\hat{n} \cdot q = h_{gap}(T_f - T_{sh}) \tag{7.4.1}$$

Here $\hat{n}$ represents the outward normal direction, q represents the heat transfer across the gap, and T_f and T_{sh} the temperature of the fuel and the sheath, respectively. The heat stored inside the gap was assumed to be negligible and therefore was not considered in the above equation.

On the fuel sheath, diffuse radiation with the surface-to-surface radiation option was enabled. The ambient temperature of the surrounding environment was set to 305 K, which is approximately the maximum normal operating temperature of the bays. A distributed ordinary differential equation was used to calculate the growth rate of the oxide layer. The heat generated by the oxidation was then expressed as a boundary heat source on the element's surface. The bundles were assumed to start out with a pre-oxidation layer thickness of 2 µm, which is approximately the minimum expected for irradiated fuel. The oxidation relation selected was determined by Natesan and Soppet [50] and is offered in the 2.1 version of MELCOR. The sheaths were defined as no-slip walls, as is standard for the objects in laminar flow.

The fluid was modelled as a laminar fluid because the Grashof number was found to be below that required for a turbulence transition according to work by Yang [87] and calculations using thermodynamic data for air [88]. The fluid was also specified as a compressible and non-isothermal flow as this is a necessary condition for natural convection in CFDs. The air was set as transparent. The buoyancy volume force was applied in the form of Equation 7.4.2 where g represents gravity and ρ_a represents the ambient density.

$$F = (\rho_a - \rho)g \tag{7.4.2}$$

The force of buoyancy, *F*, is applied throughout the entire air domain and is consistent with that defined previously in the Navier-Stokes momentum equation (Equation 5.4.1). To be consistent with the work done by Krasnaj [16], the boundary conditions of the control volume were chosen to simulate a bundle placed in an infinitely large reservoir and thereby minimize the effect of the boundary's geometry on the solution. For this purpose, the sides and bottom were defined as inlets with air at 305 K and the top was specified as an outlet. It has been assumed that the surroundings experience no change in ambient temperature. The pressure of the external boundaries was set to zero to be consistent with the definition of the net buoyancy force. For a more thorough description of the theory for the heat generation, oxidation and heat transfer processes, see Section 5.

7.5. Mesh

The mesh was generated using predominately free triangular elements. Near the fuel-sheath gap and perimeter of the sheath, boundary layers with mapped quadrilateral elements were specified to ensure the natural convection process was properly characterized and accurate continuity across the sheath. Each mesh element was of first order in the pressure and velocity fields. A symmetrical mesh was generated by mirroring the left side of the mesh onto the right. This was found to be important to prevent tilting of the plume (at the top of the bundle) in the simulation.

The entire mesh consisted of 186,014 elements with a minimum quality of 0.3572 and an average quality of 0.8432. Quality is a mesh metric based on the skewness of elements that ranges from one to zero,

where higher quality meshes tend to converge easier. There was a maximum element size of 2.5 mm, and a minimum size of 0.01 mm, and a maximum element growth rate of 1.2. The curvature factor, defined as the ratio between the element size and the radius of curvature, was set to 0.05. Parametric studies were performed on each of these mesh characteristics to ensure convergence.

7.6. Solution

Stationary and transient runs were completed on the model using built-in COMSOL solvers. Coupled solvers rather than segregated ones were chosen due to the interacting nature of the velocity, pressure and temperature fields. The 'automatic highly nonlinear' method was used in the transient case, which is a damped form of Newton's method. The steady-state solver used the double dogleg method [89] to account for nonlinearities. The direct solver PARADISO was preferred over the default MUMPS due to its noted improvements in stability and speed. A technique called 'viscosity ramping' [90], wherein a factor is applied to the kinematic viscosity to slowly increase the fluid's freedom of movement, was used to improve the solution's stability and achieve convergence.

In the time-dependent study, the initial temperature of the fuel pellet was calculated by fixing the surface temperature of the fuel sheath at the normal pool operating temperature. The starting temperature profile is thus similar to the bundle's equilibrium temperature in the IFB water. The models were run for three hours of simulated time with data sampled every 30 seconds. Transient effects such as oxidation were included in this study. Conversely in the time-independent study, the oxidation growth and lifetime integral function for predicting transition were disabled. This is because oxidation is an inherently time-dependent phenomenon.

7.7. Steady-State Model Results

An important step of the modelling process is to ensure the discretization of the mesh is fine enough to accurately resolve the outputs. The curvature factor was found to have the most influence on the maximum temperature of the sheath. Conversely variation of the growth rate, element size limits did not produce discernable changes. Figure 21 shows the convergence with a finer curvature factor by showing the steady-state maximum temperature as a function of the number of elements.

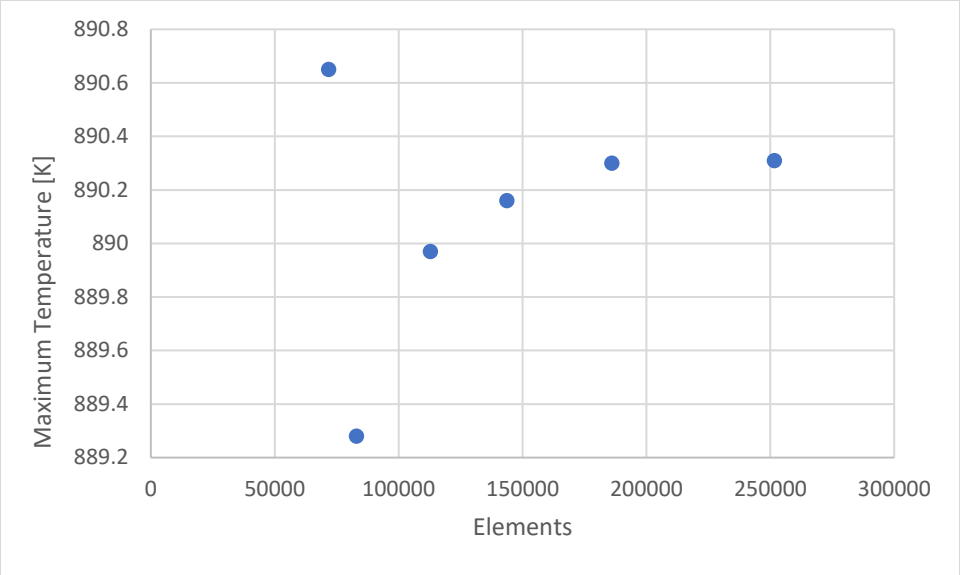

Figure 21: Convergence study of temperature with an increasing mesh density. Curvature factors of 0.4, 0.2, 0.075, 0.0625, 0.05 and 0.0375 were used respectively, where a smaller curvature factor indicates a finer mesh.

The maximum temperature observed for the 2 kW bundle was 890.3 K and convergence is achieved after 186, 014 elements, or a curvature factor of 0.05. It is clear that low-resolution meshes still produce relatively accurate results, which are on the order of a degree Celsius. This convergence study was not repeated for the transient model as they both used the same discretization scheme.

As stated earlier, the maximum temperature was 890.3 K for the steady-state model. As shown in Figure 22, there is a vertical plume rising from the bundle and little airflow through the interior elements. It is also apparent that the hottest elements are those located in the upper centre area.

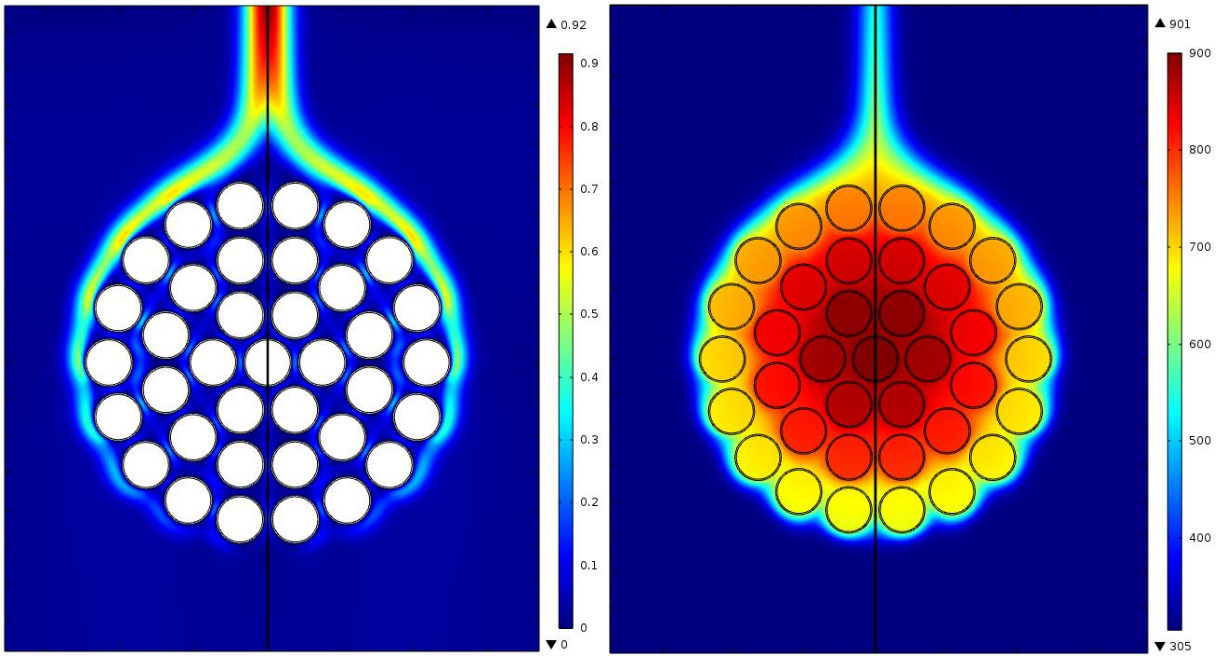

Figure 22: Fluid absolute velocity in metres per second (left) and temperature in Kelvin (right) are shown for a single fuel bundle with a decay heat of 2 kW after 3 hours of simulated time.

The fastest moving air is at the top of the plume and if the control volume were extended, higher velocities would be reached. However, this was not a variable of interest.

One of the primary sources of uncertainty in the model was due to the characterization of the fuel to sheath gap. The assumption of an open gap with a fission gas fill is conservative. Trials were also conducted using a helium gas fill to simulate bundles with low fission gas releases to the gap. However, the thickness of the gap varies considerably in the spent fuel database. A parametric study has been designed to examine the uncertainties related to the gap size as shown in Figure 23.

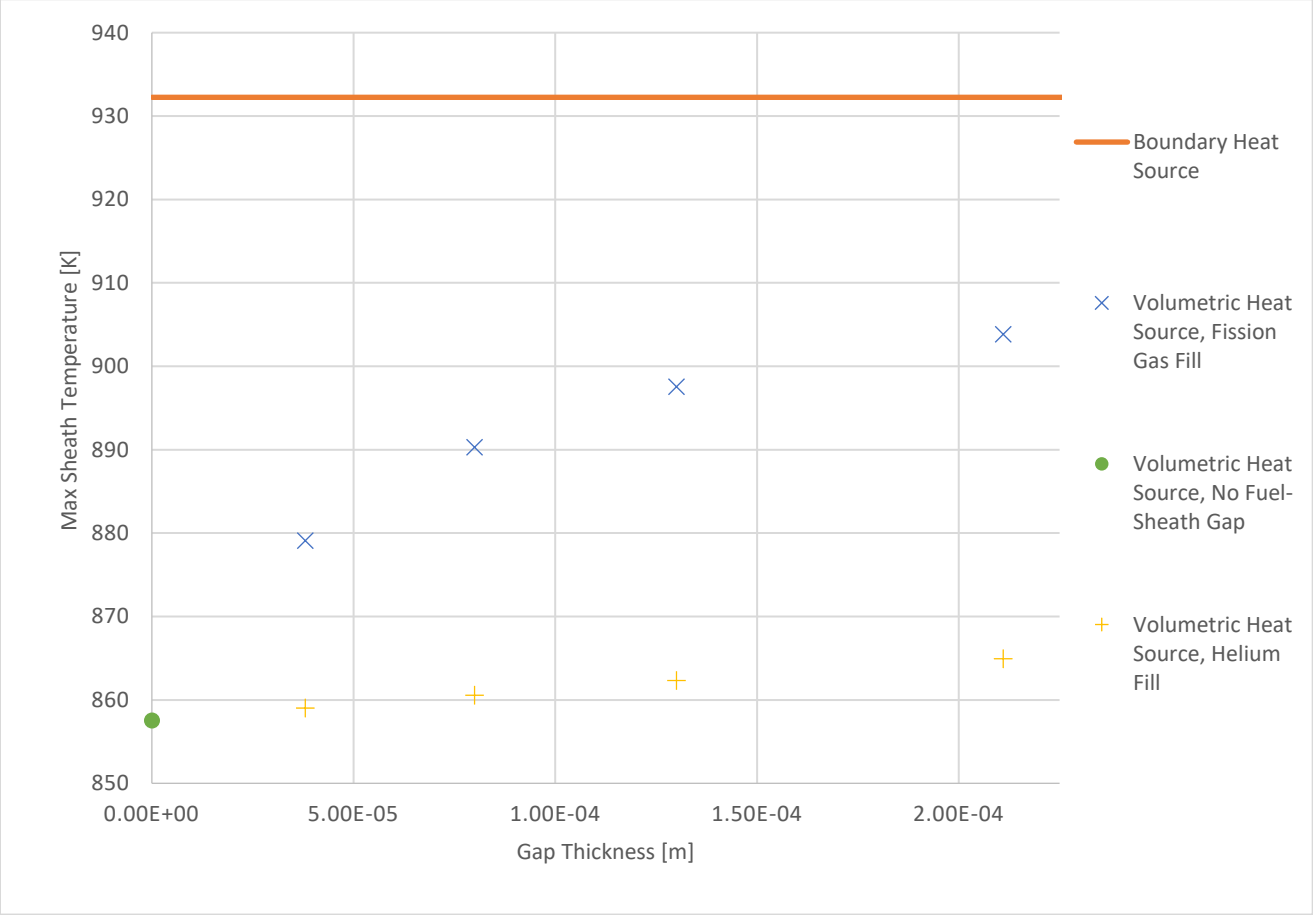

Figure 23: Maximum sheath temperatures with various gap thickness (and therefore thermal resistivities). The boundary heat source trial uses the same heating scheme as that employed by Krasnaj in his model [16]

The outer diameter of the sheath was not varied for the trials. The gap thicknesses chosen were 38 µm, 80 µm, and 130 µm representing the low, middle and high range values of irradiated CANDU fuel according to one reference [59]. The last value of 211 µm was intended to simulate the gap of a slightly ballooned element. To examine the behaviour of the curve at its limits, additional trials were completed. The model by Krasnaj [42] was reproduced where the heat is instead applied as a boundary source which resulted in the highest temperatures. Another trial was completed where the thin thermally resistive layer was removed entirely, which resulted in the lowest value as expected. The temperature of the trials using a helium gas fill resulted in lower temperatures than the one with a fission gas fill and was almost as low as the model which did not explicitly model the fuel-sheath gap.

An investigative study on ballooned elements was also completed as there is expected to be significant swelling of the rods at higher temperatures [65]. Since there would be a high degree of uncertainty with regards to the fuel-sheath gap, a boundary heat source via the Krasnaj model [42] was used to predict temperatures. The results are shown in Figure 24.

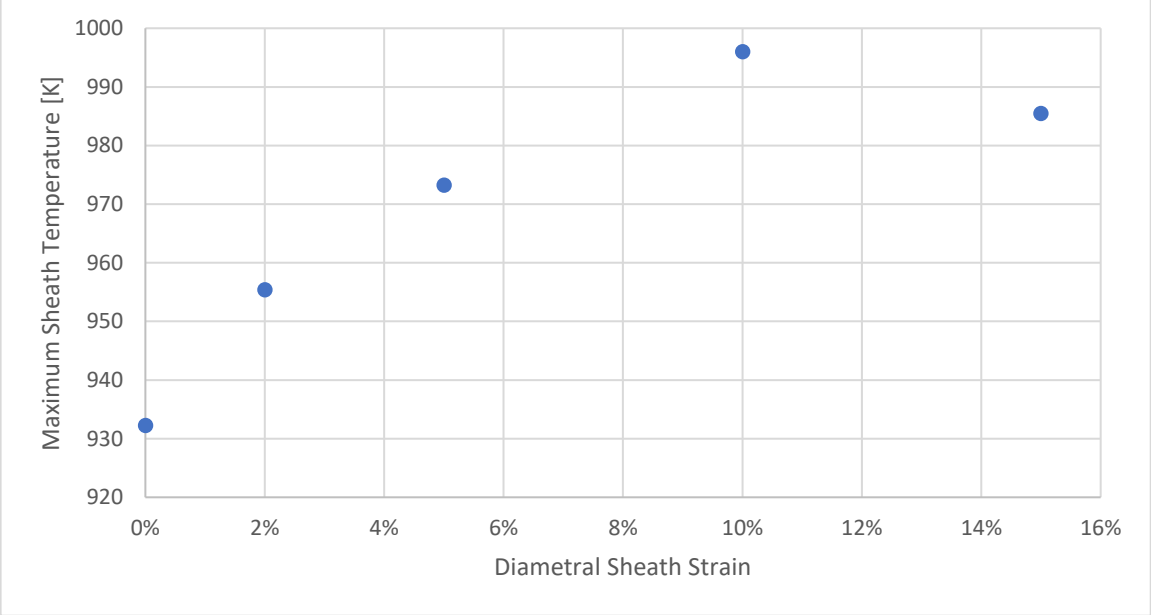

Figure 24: Maximum sheath temperature experienced by the fuel at different strains for a 2 kW bundle.

The peak temperature in the trials was observed for the fuel with a 10% strain rate. For this trial, the ballooned elements were not yet in contact with one another and the maximum sheath temperature was 996 K. The steady-state temperature profile for the ballooned elements for a 15% strain rate is shown in Figure 25.

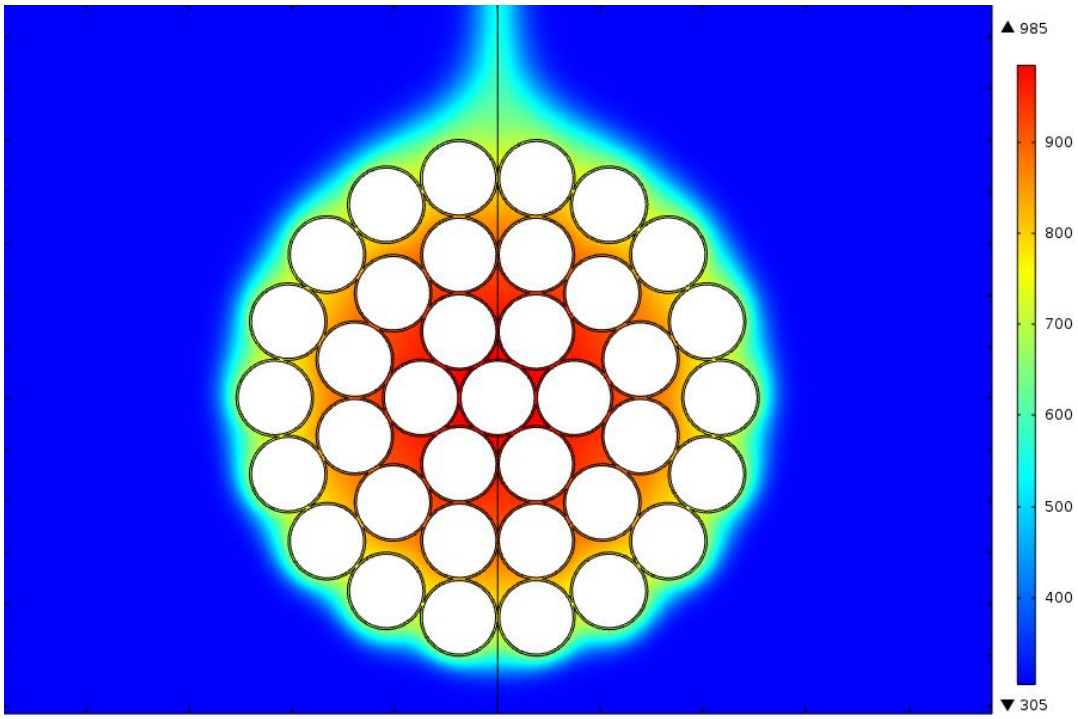

Figure 25: Temperature profile for a 2 kW bundle with ballooned elements that have undergone a 15% strain rate.

In creating the geometry, the radius was expanded and the overlapping sections were merged into a single domain. The same general discretization scheme was used which resulted in a similar number of elements as the previous trials. The interior spaces were modelled as a solid transparent medium with the same properties as air. The maximum sheath temperature was 985 K, which represents a 10 K drop in temperature from the previous trial.

7.8. Transient Model Results

To investigate how much time is available before a severe fuel failure occurs, the 2D CFD was extended to a transient analysis. Figure 26 shows the bundle's maximum sheath temperature in air for decay heat loads from 1 to 4 kW over time. An additional trial was completed without oxidation for the 4 kW bundle, which showed that not including oxidation caused only a 10-20 degree decrease in temperature during the first three hours. As per a previous analysis [16], the bundles with a decay heat above 873 K (600 °C) were considered to be at risk of transitioning to the post-breakaway oxidation phase.

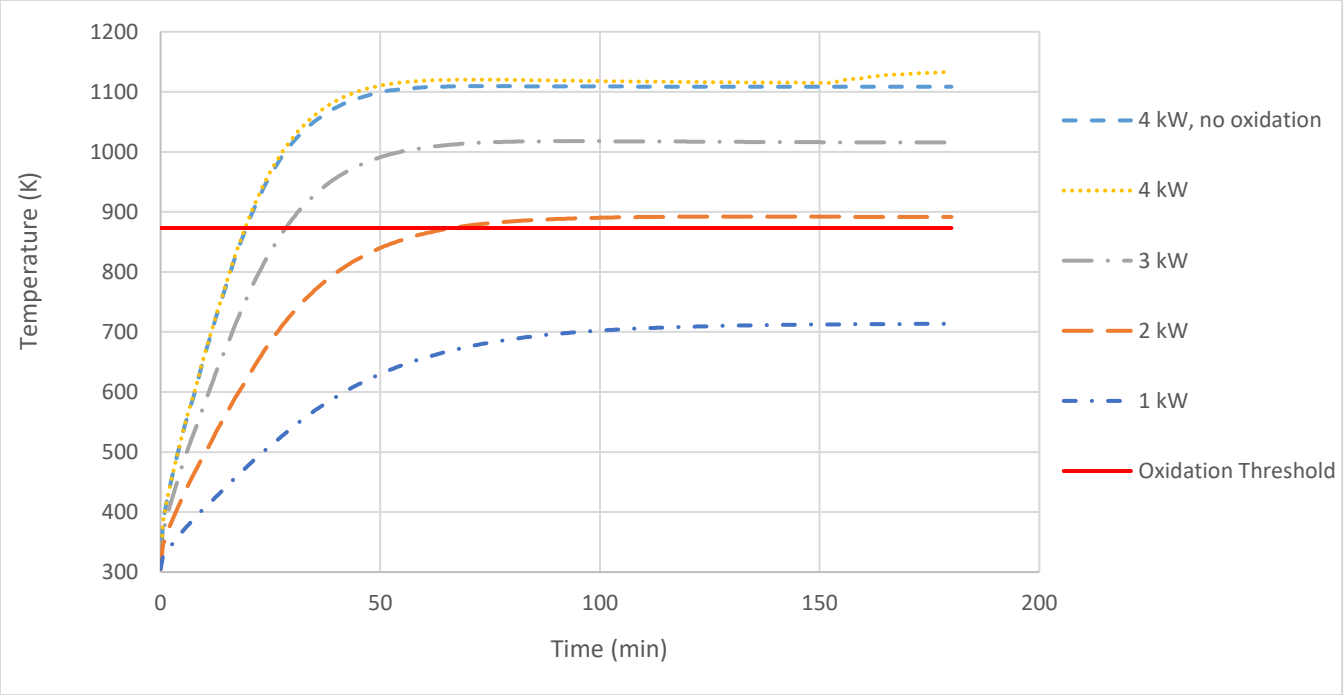

Figure 26: Maximum surface temperature of the fuel bundle cross section over time.

As shown in Table 7, the average internal temperature of the fuel was estimated to range from 323 K to 372 K depending on the bundle's thermal power. The breakaway threshold was surpassed by the 2 kW, 3 kW, and 4 kW bundles after 66, 28, and 19 minutes, respectively. However, more sophisticated techniques were also employed to predict the breakaway time through the lifetime integral, LF (described in Section 5.2). This method is empirically based on separate effect tests and has been implemented in MELCOR 2.1.

Table 7: Summary of the initial conditions and the time before fuel damage is expected to occur.

Bundle Thermal Output	Average Initial Fuel Temperature (K)	Time to surpass oxidation threshold, >873 K (minutes)	Time to breakaway (hours)
1 kW	322.9	-	545.9
2 kW	340.0	66	34.2
3 kW	356.3	28	7.2
4 kW	372.0	19	2.6

The time to breakaway was calculated by taking the gradient of LF with respect to time of the last two points and extrapolating to when the maximum LF value on the sheath is equal to one. After a breakaway occurs on a part of the sheath, the reaction is expected to also begin to occur in neighbouring elements. The 4 kW bundle was the quickest to approach the breakaway regime at 2.6 hours. Conversely breakaway was not a significant issue for the 1 kW bundle, which is predicted to reach breakaway after 545.9 hours, or about 23 days.

The oxide layer's growth from the initial thickness of 1 μm was also examined for each of the four bundle powers. As shown in Figure 27, the 1 kW bundle undergoes relatively little increase in oxide thickness.

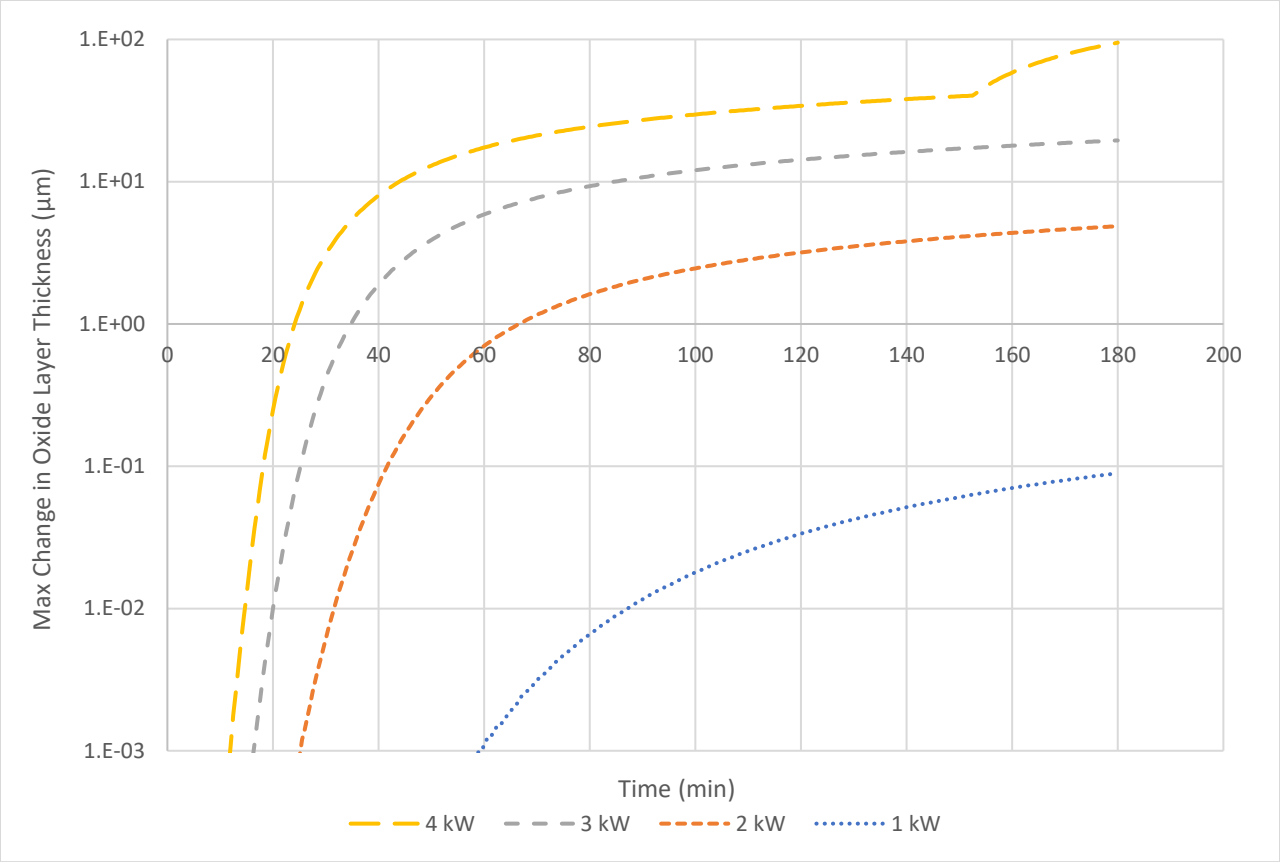

Figure 27: Oxide thickness at the upper centre of the bundle (which corresponds to the area of the max temperature in the bundle) is shown over a 3 hour period.

However, the 4 kW bundle shows a significant increase in the oxide layer's thickness, especially after undergoing breakaway at 154 minutes. The maximum of the lifetime integral, LF, as a function of time is shown in Figure 28.

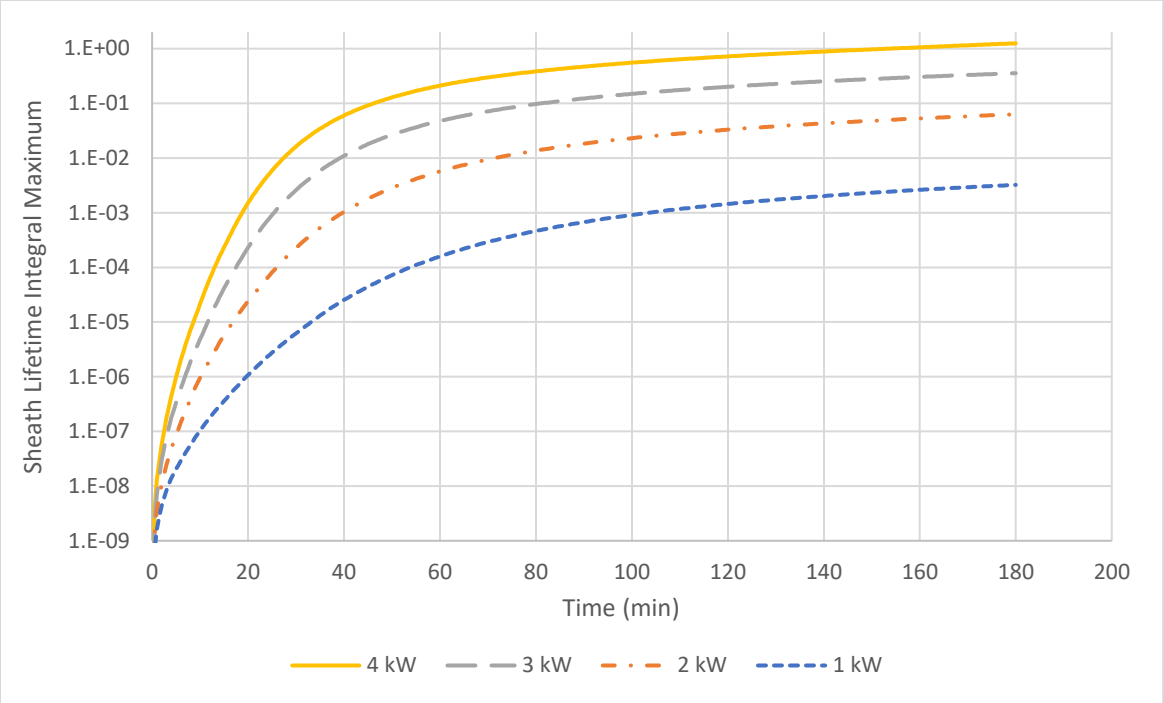

Figure 28: Value of the sheath lifetime integral over three hours for various bundle powers. When this value reaches one, the oxidation is expected to transition from parabolic to linear reaction kinetics.

The sheath's oxidation kinetics enters the post-breakaway regime after the lifetime variable reaches one. This transition was observed in the 4 kW bundle after approximately two and a half hours, while the other bundle powers were relatively far from breakaway.

7.9. Discussion

After a bundle's thermal power has dropped below 1 kW (approximately 14 days [48] after being discharged from the reactor), the fuel was not predicted to enter the high-risk temperatures for a breakaway oxidation. The results suggest that a severe fuel failure due to oxidation is highly unlikely for the vast majority of bundles in a fuel bay if maintained within an open environment. According to work by Fan [11], there is expected to be approximately 200 bundles with powers higher than 0.6 kW for the potential 45,000 spent fuel bundles in an IFB. The results of this model might be applicable to a small number of bundles (< 0.5%) at the top of a rack when they are first exposed, or a single bundle in the fuel machine.

As demonstrated by Krasnaj [42] and confirmed here, bundles that have been discharged earlier than two weeks will reach temperatures sufficient for a breakaway oxidation. However, there is some time before this occurs as shown in Table 7. Operator intervention may also be credited in 30 minutes for actions outside the control room [91] and thereby should be able to prevent the occurrence of a breakaway oxidation reaction. The results indicate that operator intervention should be assured in the event of the exposure of a single bundle or small number of spaced bundles inside a well-ventilated environment.

Comparisons can be made with earlier iterations of the model and those in literature to verify the model and investigate different effects. The improvements that have been made from earlier iterations of the model have been summarized in Table 8.

Table 8: Summary of changes between the current model presented in this thesis and previously published model [83]

	Previous Model	Current Model	Justification
Control Volume size	170 mm by 140 mm box; bundle was centred 65 mm from the bottom	200 mm by 200 mm box; Bundle centred	More accurately simulates flow
Control Volume side-wall and bottom boundary conditions	Frictionless and adiabatic walls	Inlets at zero pressure	More accurately simulates flow
Conductivity Coefficient of the Fill Gas	Correlations [92] for 15% krypton and 85% xenon mixture at STP	ELOCA correlations [60] for fission gas at 488 kPa [75]	New correlation can account for different pressures
Fuel-Sheath Gap thickness	180 µm	Parametric Study with values of 38 µm, 80 µm, 130 µm and 211 µm	Updated for more detailed dataset
Oxidation Correlation	Benjamin [25] (MELCOR v1.8 and prior)	Soppet and Natesan [50] (MELCOR v2.1 and onwards)	Original reaction coefficients were overestimated
Determination of Breakaway	600 °C threshold	Lifetime (LF) variable	More accurate prediction of the breakaway time

The results of the earlier model are shown in Figure 29.

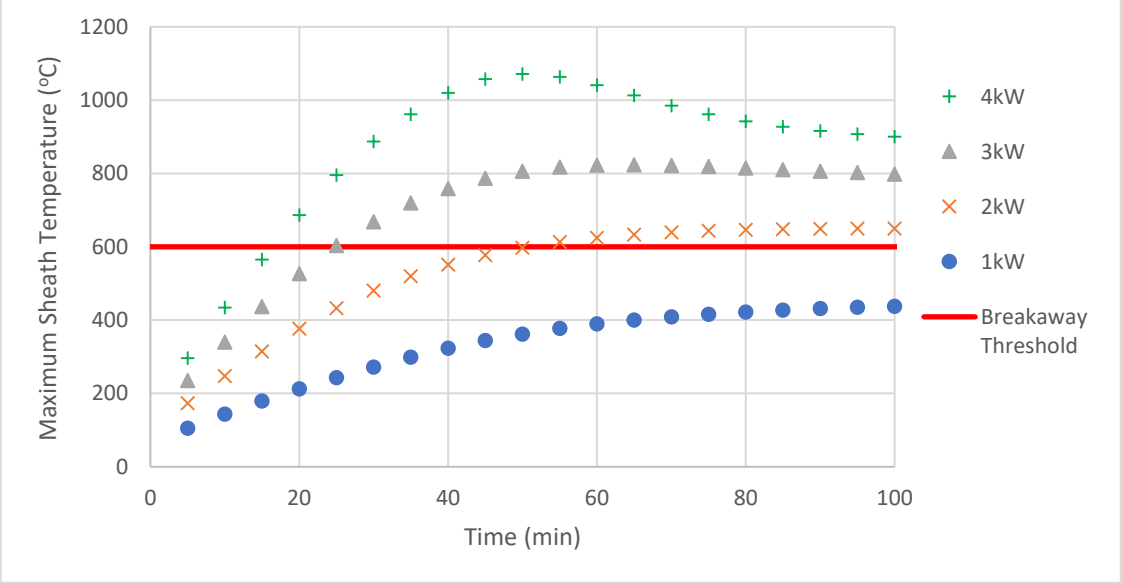

Figure 29: Maximum surface temperature of the fuel bundle cross section over time.

The most significant difference between the previous and current version is in the oxidation model. While the previous iteration used correlations from Benjamin [25] as implemented in MELCOR 1.8, the new one uses more recent data from Natesan [50] for pre- and post-breakaway, which is the default in MELCOR 2.1. The reaction constant used in the original model was extremely energetic as shown in Figure 10 of Section 5.2, and accordingly, the temperature increase was 194 ℃ for the 4 kW bundle, compared to the 25 ℃ increase in the current model.

The other subtler, but still noticeable change is in how the gap was modelled. It was determined that the previously assumed gap size of 200 μm was larger than what is realistically expected for discharged spent fuel at standard temperature and pressure [59]. A parametric study was instead conducted over a range of high, mean and low values for the gap thickness, which resulted in slightly lower temperatures. The conductivity coefficient of the fill gas was also updated to use correlations from ELOCA [60], which can account for variations in pressure. Overall there were only slight differences between the steady-state temperatures of the models.

The major distinction between this model and those existing in literature are: (1) it models the fuel temperature over time and (2) it models the fuel behaviour on the interior of the sheath. As has been demonstrated, modelling conduction within the interior of the fuel element is not essential in steady-state scenarios. Previous authors, Krasnaj [42] and Seimens [93], represented the decay heat as a boundary heat source and achieved satisfactory agreement with experiments. The work produced by Krasnaj matches well with the results of this study, as shown in Table 9. The model also compared favourably to the single bundle experiments by AECL [94], but the data are proprietary and cannot be shared in the body of this report.

Table 9: Comparisons of the results from the Krasnaj model [42] and that produced in this work.

	Current Work		Krasnaj		Difference	
Bundle Thermal Power	Average [K]	Max [K]	Average [K]	Max [K]	Average [K]	Max [K]
1 kW	617	713	613	730	4	-17
2 kW	765	892	779	929	-14	-37
3 kW	868	1016	895	1068	-27	-52
4 kW	946	1134	984	1177	-38	-43

Modelling of element interior increases the computational complexity and run times, so a simple boundary source is more practical for estimation in many applications. However, the specification of a uniform boundary heat flux results in overestimated temperatures, as the heat is unable to conduct through the cooler areas of the sheath from the pellet.

Models that use volumetric heat generation can account for different radial heat fluxes on the inside of the sheath and can be used to observe the effects of the fuel-sheath gap. As shown in Figure 23, a larger, more resistive gap resulted in higher sheath temperatures, which approach that of the Krasnaj model.

Lower temperatures have similarly been observed when using volumetric heat sources instead of boundary heat sources in CFD simulation of moderator circulation [95]. To understand the difference in heat transfer around the gap's circumference, the definition of the thermally thin layer presented in Section 7.4 (Equation 7.4.1), Boundary Conditions will be revisited in Equation 7.9.1.

$$n \cdot \Delta q = h_{gap}\left(T_{fuel} - T_{sh}\right) \tag{7.9.1}$$

For the heat transfer around the element to be uniform, there must be a consistent temperature difference between the fuel and the sheath. Although the sheath temperature, T_{sh}, is influenced by the surrounding elements, a highly resistive gap will greatly increase fuel temperatures and diminish the effect of thermal

variations around the sheath. In the limit where we have an infinitely resistive gap or uniform sheath temperatures, the volumetric heat source model's behaviour will match that of the boundary heat source and there will be uniform heat transfer along the element's radius.

The most important motivator for modelling the fuel's interior, however, is in transient analysis. Since the fuel absorbs energy after exposure to air, part of the heat load is directed to increasing the fuel's temperature and part is transferred through to the sheath. It is not until later that the temperatures approach steady-state and the entire decay heat is transferred through the sheath to the surroundings. Ignoring this effect will generate errors in the temperature as a function of time, and these errors will propagate through phenomena such as oxidation, which depend on these values. Therefore, there are two primary applications for the detailed model: (1) during transient simulation and (2) when there are high demands on accuracy.

Although the presented model represents a step forward in modelling of irradiated CANDU fuel, there are limitations in the study. One issue that was investigated was the effect of the mechanical deformation on the bundle. It was found that a bundle with a uniform sheath strain of 10% would experience a maximum sheath temperature of 996 K, which is about 64 K hotter than an un-deformed bundle. The temperature predictions for the bundle with a 10% strain were also higher than that of the 15% strain case. This is because conduction will begin to occur directly between the touching sheath surfaces of ballooned elements within a bundle, which compensates for the loss in convective heat transfer. Data show that the expected increase in temperature due to ballooning is limited to 100 K for recently discharged 2 kW bundle, even with complete closure of radial flow paths. If more CANDU specific data could be obtained as to the degree of thermal fuel pellet radial expansion, the analysis could be extended to transiently model the conduction across the fuel-sheath gap and the fuel sheath's integrity.

Other potential areas for improvement are in the oxidation model. Presently the breakaway is still modelled by parabolic reaction kinetics, which will not be able to simulate a self-sustaining reaction as effectively. It would be better if linear kinetics were used. Another effect that could potentially be included is the thermal resistivity of the sheath's oxide layer, as this may further elevate temperatures for highly oxidized surfaces.

However, it is more important that the effects of neighbouring bundles be accounted for as this has the potential to have a much more dramatic effect on the temperature. In the theoretical limit of an effectively adiabatic environment, as assumed in the preliminary analysis of the Korean FUELPOOL severe accident code plan [26], a year-old fuel will be capable of reaching the temperatures required for breakaway. The boundary conditions applied in this model are idealized and not representative of a bundle located within a rack; therefore the analysis is not bounding when applied to the entire spent fuel bay. To more accurately predict the ambient temperatures for the convective and radiative heat transfer, the modelling of CANDU racks is crucial. It will also be necessary to implement techniques that reduce the model's computational loads, as it has been found that COMSOL modelling of a detailed full rack is not possible with the current hardware. Simplifications such as the approximation of the bundles as cylinders, a porous lump or, as has been done in the following section, ignoring flow resistance will be needed to estimate the temperature inside a fuel rack.

8. INDIVIDUAL FUEL RACK ANALYSIS

In the first stage of modelling, it was recognized that the effect of neighbouring bundles in a rack would present a significant increase in temperature that was not included. This was confirmed in the PKPIRT, where the convection process was identified as a poorly understood, but highly important phenomenon [22]. It was imperative that the characteristics of the bulk flow were understood, and to this effect a basic model was created to predict the outlet temperatures of a rack at steady-state. However, issues were noted in the physics that necessitated a re-analysis.

The initial conditions for this analysis are based on the original work performed with minor changes to make the model more realistic. The original analysis presented in the PKPIRT [45] assumed steady-state in saturated steam at 373 K, but the analysis here instead uses air to be consistent with the ideal gas law and acknowledges that steam will not likely be the coolant in long term, especially if the IFB building is damaged. LOCA SFP analyses completed by the USNRC [96] [97] and CNSC [16] assume air as the coolant, thus the change was considered warranted. Air has a higher density than steam, but a much lower specific heat capacity, which results in less effective cooling and higher temperatures. It is still valid to use steam as a coolant (especially early in an accident when pool boil-off would release saturated steam), but a correlation or lookup table relating the density and temperature at 101.325 kPa would be required in the analytical models. The reasons supporting a steady-state analysis are numerous: (1) it simplifies a complex problem, (2) using consistent initial conditions allows comparisons to previous work, and (3) an IFB severe accident code needs to be able to calculate the equilibrium temperature.

The decay heat of the rack has also been recalculated as a range of values by interpolating data by Fan et al. [11] in Figure 9. Assuming 16 bundles are added to a rack per day (which corresponds to the upper range of bundles being fuelled each day on an individual reactor [12]), a rack will take 29 days to load. If the rack is uncovered 3 days after it is loaded fully, the rack's thermal power will be approximately 0.5 MW. It is worthwhile to note that this rack would be located in the reception bay, and not the primary IFB. If the rack is uncovered 12 days after it is loaded, the rack will have a thermal power of 0.35 MW. After additional 50 days since being loaded (79 days in total), the power will have reduced to 0.20 MW and after 300 additional days (329 days in total), it will only be emitting 0.05 MW of heat.

8.1. Analytical Model Description

The cooling of a rack of spent fuel is essentially a natural convection problem with horizontal and vertical openings. This phenomenon has been studied for building ventilation in different types of structures. Although there are a few stratified buoyancy models [98], the fully mixed model presented by Andersen [99] was chosen for its simplicity. The theory describes the interior as a single stagnant zone with a constant temperature and uses Bernoulli's equation to determine the flow rates across the openings. For a rack, the cooling air passes through the sides of the rack control volume and exits via the top as shown in Figure 30. Note that the model assumes that the flows are unobstructed through the interior of the enclosure.

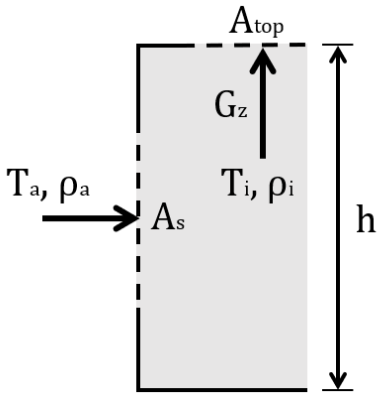

Figure 30: Diagram of buoyancy-driven flow paths through a rack

The temperature and density are represented by T and ρ as per convention, where the a and i subscripts indicate the ambient or internal zone, respectively. The top area, A_{top}, side area, A_s, and height of the rack, h, are also shown in the diagram. The mass flux at the outlet is represented by G_z.

The net average pressure at the outlet and inlet are solved using the neutral plane, which is defined as the effective level where internal and ambient zone's pressures are equal. The neutral zone simplifies the momentum equations by allowing the average pressure differences between the two zones to be expressed as a function of density difference, gravity and the distance between the neutral zone height and an opening's mid-height. This relation is shown explicitly in Equation 8.1.1, where H_{out} represents the difference in height between the outlet and the neutral zone height.

$$\Delta P_{out} = \Delta \rho g H_{out} \tag{8.1.1}$$

Andersen derived Equation 8.1.2 for an outlet with the conservation equations across the openings, in conjunction with the hydrostatic pressure equations for the interior and exterior zones.

$$H_{out} = \frac{\frac{h}{2}\rho_a C_{d\_top}^2 {A_s}^2}{\rho_i A_{top}^2 C_{d\_s}^2 + \rho_a C_{d\_top}^2 {A_s}^2} \tag{8.1.2}$$

However, since the rack's side area is much greater than the top area, H_{out} is well approximated by the height difference between the openings.

$$H_{out} \approx \frac{h}{2} \tag{8.1.3}$$

The orifice equation may be applied with the pressure difference due to buoyancy (Equations 8.1.1 and 8.1.3) to solve for the volumetric flow of air, q_{out}, through the rack. This result agrees with the relation produced by Li [100] for a single zone building with two openings.

$$q_{out} = C_d A_{top} \sqrt{\frac{(\rho_a - \rho_i) g h}{\rho_i}} \tag{8.1.4}$$

Note, C_d represents the discharge coefficient and describes the pressure losses across an opening due to inertial and frictional forces. Although there is a void of experimental data to directly determine C_d, solar chimneys and other types of ventilation openings present a well-studied theoretical equivalent to the discussed problem. Relations developed for the flow rates of solar chimneys completed by Bansal [101] are also consistent with that derived in Equation 8.1.4. Akbarzadeh [102] and Andersen [103] have recommended a discharge coefficient of 0.57, while a discharge coefficient of 0.6 was suggested by Flourentzou for chimney systems [104]. This value was used in the base case, but was also expanded on in a parametric study to estimate the model's uncertainty.

By applying the ideal gas law assuming the absolute pressure is relatively constant and substituting the volumetric flow, the average mass flux G_z may be expressed according to Equation 8.1.5.

$$G_z = C_d \rho_a \sqrt{\frac{T_a}{T_i} g h \left(\frac{T_i - T_a}{T_i}\right)} \quad (8.1.5)$$

The conservation of energy is used in conjunction with Equation 8.1.5 to solve for the temperature. In Equation 8.1.6, Q_{tot} is the total thermal power of the rack and $C_{P\,avg}$ is the specific heat capacity at constant pressure evaluated at the average of the ambient and internal temperature.

$$Q_{tot} = C_{p\_avg} G_z A_{top} (T_i - T_a) \quad (8.1.6)$$

Equations 8.1.5 and 8.1.6 can be easily solved for low temperature systems by assuming the $T_i \approx T_a$ in the denominators. However, it is more appropriate to use numerical methods for high outlet temperatures. For a complete derivation of natural ventilation in a one-zone enclosure with two openings, readers are recommended to refer to Andersen's paper [99].

The described model is similar to that presented in the PKPIRT panel [45]; however, pressure differences across the outlet were not considered leading to overestimated flow velocities. Although Andersen's analysis was derived with a focus on vertically aligned apertures, experimental work has shown that his work is still applicable for horizontal openings when the inlet to outlet area ratio is between 0.28 and 11 [105]. The single-zone theory remains logically consistent for a horizontal opening, as an energy change in Bernoulli's equation due to the difference in the flow's elevation will be balanced by an increase in hydrostatic pressure.

The ambient temperature was selected to be 373 K (100 °C) based on the PKPIRT analysis in saturated steam. Full-scale calculations of an IFB are required to conclusively determine a value for the ambient temperature, but they presently do not exist. Upon comparison with a LWR study of SFPs [96], it was determined that taking 373 K as the ambient temperature is acceptable.

8.2. Computational Fluid Dynamics (CFD) Model Description

To compare with the previous results, a 3-D model has been developed in the COMSOL platform with the Heat Transfer and CFD modules to study the rise in temperature of a single fuel rack over time. COMSOL version 5.3 [106] is a finite element analysis simulation software that is designed to deal with coupled phenomena, and as such is well suited to thermal hydraulic problems with the potential to integrate more complicated effects. Although nuclear plants carry their own variant of fuel rack, a typical rack tray design in use by one of the Canadian CANDU stations was chosen for its simplicity. Similar to the bundles, the racks will contribute to the flow resistance. Analysis from the PKPIRT concluded that a more open structure should make convection cooling more efficient in the tray design compared to the other types of racks [45].

Flow resistances created by the supporting frame and the bundles have been omitted so direct comparisons can be made to the analytical theory. Modelling the complexity of a fully loaded rack in a 3D model was found to be unfeasible with the presently available computing resources. Superimposing the model by Krasnaj on an analytical model without flow resistance will only provide a lower bound estimate for the fuel sheath temperatures unless the models are coupled. Due to the long run-times for the Krasnaj model [42], this is not expected to be practical. The use of simplified geometries or porous media approximations will make the problem amenable to CFD techniques, but a non-trivial amount of work is required to determine the porous media parameters and qualify the effects of geometric simplifications.

One simplification that was employed was symmetry, as it is only necessary to model one quarter of a rack as shown in Figure 31. The heated volume representing the rack is specified as an air-filled rectangular prism with a base of approximately 0.5 m by 0.7 m and a height of about 2.5 m.

It is assumed that there is an empty bottom compartment with a height of 0.13 m to prevent the temperature from diverging at the floor and to represent the approximate spacing expected in a fuel bay. The rack is modelled inside of a cylinder quarter with a radius of 1.5 m to minimize the modelled volume. A height of 5 m was specified to capture effects related to the plume.

The floor of the control volume used a no-slip wall boundary condition in the laminar model. The boundary conditions on the curved sides and top of the cylinder were specified as a zero-pressure inlet and outlet respectively. The cylinder's inner walls were set using the symmetry boundary condition within both the fluid and heat transfer interfaces.

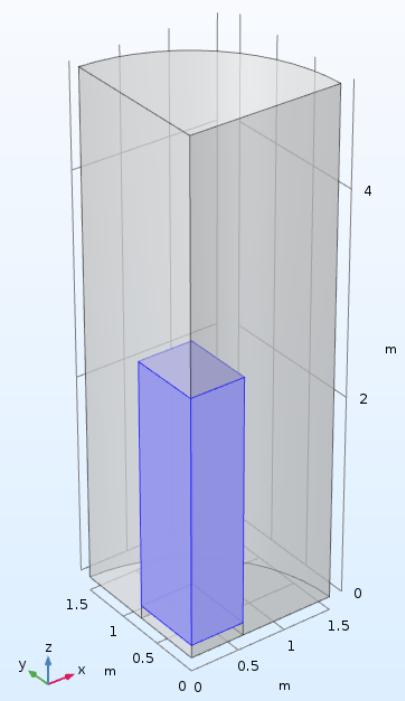

Figure 31: Geometry of a quarter of the fuel rack (highlighted in blue) and the surrounding control volume.

The thermodynamic material properties of the air were based on relationships from the built-in COMSOL library [106]. The rack and bottom compartment were filled with a fine swept hexahedral mesh while the surrounding volume was coarsely defined with tetrahedrons. Linear elements are used for both the velocity components and pressure field. A boundary layer mesh was created with 8 layers and a first layer thickness of 1 mm, which is similar to the default values provided in the COMSOL user manual [106]. No formal sensitivity study has been performed on the boundary layer mesh because the model is laminar (i.e., the monitoring of mesh dependent turbulent values such as $y+$ is unnecessary) and outputs at the floor were generally not of interest. The entire mesh consisted of 239,896 elements.

The model was created using the physics options laminar flow, heat transfer in fluid and coupled isothermal flow in COMSOL. The weakly compressible, steady-state formulation of the Navier-Stokes Equation, shown in Equation 8.2.7, was solved via the finite element solver wherein u represents the velocity vector, ρ represents the fluid density, I is the identity vector, and μ is the fluid's dynamic viscosity [106].

$$\rho(u \cdot \nabla)u = \nabla \cdot \left[-pI + \mu(\nabla \cdot u)^T - \frac{2}{3}\mu(\nabla \cdot u)I\right] + F \qquad (8.2.7)$$

The volume force, *F*, in this case, is equal to the force of buoyancy acting on the fluid elements and is responsible for driving the natural convection process. The compressible forms of the heat transport and continuity equations were used for solving the fluid flows.

Additional trials were completed to estimate the effect of turbulence on the system. The standard *k-ε* model [106] was chosen due to its widespread use, ease-to-run and comparatively light computational demands. The *k-ε* model uses wall functions at boundaries and the Reynolds-Averaged Navier-Stokes (RANS) equation to solve for the time-averaged and fluctuating velocity components. However, negligibly small differences were observed as expected between the laminar and turbulent model results.

8.3. Finite Difference Model Description

As in the analytical equation, there are five variables that must be numerically solved: the pressure, temperature, density, and the vertical and horizontal mass fluxes. The finite difference method was used with the equations for the conservation of mass, energy, and momentum in the *xy* and *z* directions, and then combined with the Bernoulli equation and ideal gas law to solve. The height of the rack was discretized into *n* evenly spaced sections and the number of each section is indicated by *i*. A square rack was assumed to nullify any differences between the *x* and *y* directions, so they can effectively be collectively referred to as the horizontal *xy* direction. The velocities at the nodes indicated in Figure 32 are unidirectional; therefore fluxes at the side entrances of the rack will act only in the horizontal direction, while the fluxes at the centre are oriented upwards.

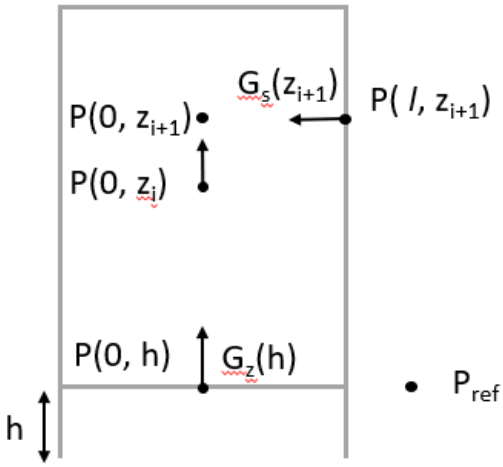

Figure 32: Pressures and mass fluxes of interest in the finite difference model.

The density of the air flowing in from the side is assumed to be at the same density as ambient fluid and uniform over the *xy* side area for a given *z* vertical slice. The temperature and density inside the stack act as an effective *xy* average for each vertical *z* slice, while the mass flux, G_z, represents the maximum at the centre.

The Navier-Stokes equation was used to solve for the momentum change in the *z* direction at the rack's centre by integrating over the step change as shown in Equation 8.3.1. The integral on the right side is evaluated by first applying the finite difference method, and then numerically via the trapezoid method.

$$\int_{z_i}^{z_{i+1}} G \frac{\delta}{\delta z}\left(\frac{G}{\rho}\right) dz = -\Delta P_{x=0}(z_{i+1}, z_i) - \int_{z_i}^{z_{i+1}} \rho g \, dz \qquad (8.3.1)$$

Note that since the flow evaluated at the centre is unidirectional in the *z* direction, the derivatives of the mass flux with respect to the *xy* directions that would normally appear in the Navier-Stokes equation are

zero. The system is in steady-state, which thus eliminated the time-dependent term. The viscous term has been assumed to be negligible as there are no walls or surfaces with which to interact.

A loop can be used to evaluate the pressure difference that arise from each vertical step shown in Figure 32. This is done by relating the pressures at the entrances and using the *xy* momentum equation to relate the pressure at the sidewall to the rack centre. In mathematical terms, it may be expressed according to Equation 8.3.2.

$$\Delta P_{x=0}(z_i, z_{i+1}) = \big(P(l, z_{i+1}) - P(0, z_{i+1})\big) + \big(P(0, h) - P(l, z_{i+1})\big) + \sum_{j=1}^{i} \Delta P_{x=0}(z_j, z_{j-1}) \quad (8.3.2)$$

Where:

- $z_0 = h$

The value of $\sum_{j=1}^{i} \Delta P_{x=0}(z_j, z_{j-1})$ is defined by previous steps and can be easily shown to be zero at the first step. A stagnant reference point outside the rack is used to relate the two pressures for the entrances at the rack's bottom and sides. Using Bernoulli's principle, Equation 8.3.3 is obtained.

$$P(0, h) - P(\, l, z_{i+1}) = \frac{1}{2\rho_o}(G_w(z_{i+1})^2 - \bar{G}_z(h)^2) \; + \; \rho_a g(z_{i+1} - \, h) \quad (8.3.3)$$

The pressure difference between the sidewall and rack centre is solved via the Navier Stokes equation in the *xy* direction.

$$\int_0^l G_s \frac{\delta}{\delta x}\left(\frac{G_s}{\rho}\right) dx = -\Delta P_{z_{i+1}}(l, 0) \quad (8.3.4)$$

As before, viscosity and time-dependent effects are ignored. The cross inertial terms evaluated at the centre and side each have a value of zero, and it was therefore assumed that the net value of their integrals was negligibly small.

As was done for the *z* direction, the finite difference and trapezoid integral methods may be used in the horizontal direction.

$$-\frac{G_s(z_{i+1})^2}{2\rho_o} \; = \Delta P_{z_{i+1}}(l, 0) \quad (8.3.5)$$

However, since there are only two discrete points, the solution will be approximate. The final part of the pressure equations is also defined in Equation 8.3.5.

The conservation of mass needs to be applied to relate the vertical and horizontal mass fluxes. The increase in the vertical mass flux through the rack as a function of the side flow was solved via Equation 8.3.6.

$$G(z_{i+1}) \; = G(z_i) \; + \bar{G}_{si}\left(\frac{A_{si}}{S_F A_{xy}}\right) \quad (8.3.6)$$

Here A_{si} represents the side area of a vertical step, A_{xy} represents the rack's *xy* area, S_F represents the ratio of the centre mass flux to the average mass flux through the rack, which will hereby be referred to as the 'shape factor'. The shape factor is an unknown constant but can be estimated using general knowledge of flows and mathematical averaging. A paraboloid profile was assumed based on the shape of fully developed flows in circular tubes, which resulted in a value of 4/9.

The conservation of momentum (Equation 8.3.3 and Equation 8.3.5) and mass equations (Equation 8.3.6) may be combined to form a quadratic equation of the next vertical step's side flow from the previous steps. The newly formed equation is then solved via the quadratic formula in conjunction with the conservation of energy, shown in Equation 8.3.7. The nonlinear solver chosen to complete this task was bisection method, which is documented in the Appendix A.

$$Q_i = C_p(T_i)\, S_F G(z_{i-1}) A_{bot}(T_i - T_{i-1}) + C_p((T_i + T_a)/2)\, G_s(z_i) A_{si}(T_i - T_a) \quad (8.3.7)$$

One necessary substitution is shown in Equation 8.3.8, which allows the expression of the density terms as a function of temperature. This relation follows directly from the ideal gas law by assuming the absolute pressure is relatively constant for the entire rack.

$$\rho(z_{i+1}) = \rho_a \frac{T_o}{T(z_{i+1})} \tag{8.3.8}$$

Using the outlined method, a temperature and velocity profile inside the rack can be numerically solved as a function of the rack's height.

8.4. Sensitivity Analysis of Results

For the primary test case, it is assumed that the total equivalent thermal output of the rack was 0.35 MW, or that each bundle emits on average 750 W of decay energy. If water is only lost due to evaporation, 0.35 MW is expected to be approximately the highest thermal power for a single rack after accounting for the time taken to load the fuel and boil off water to expose the rack. Although heat loads utilized are for a full rack, the models only provide a low bound for the outlet temperatures. The value is an underestimate because inclusion of flow resistance will slow down the air passing through the rack and thereby cause significantly higher outlet and fuel sheath temperatures.

As a first step, the fineness of the mesh in the CFD model was varied to ensure appropriate convergence had been achieved. The hexahedral mesh representing the rack was found to have the most effect on the temperature and the discretization scheme was varied from 'coarse' to 'extremely fine' inside this volume. The average outlet temperatures compared to the number of nodes resulting from the different meshes is shown in Figure 33.

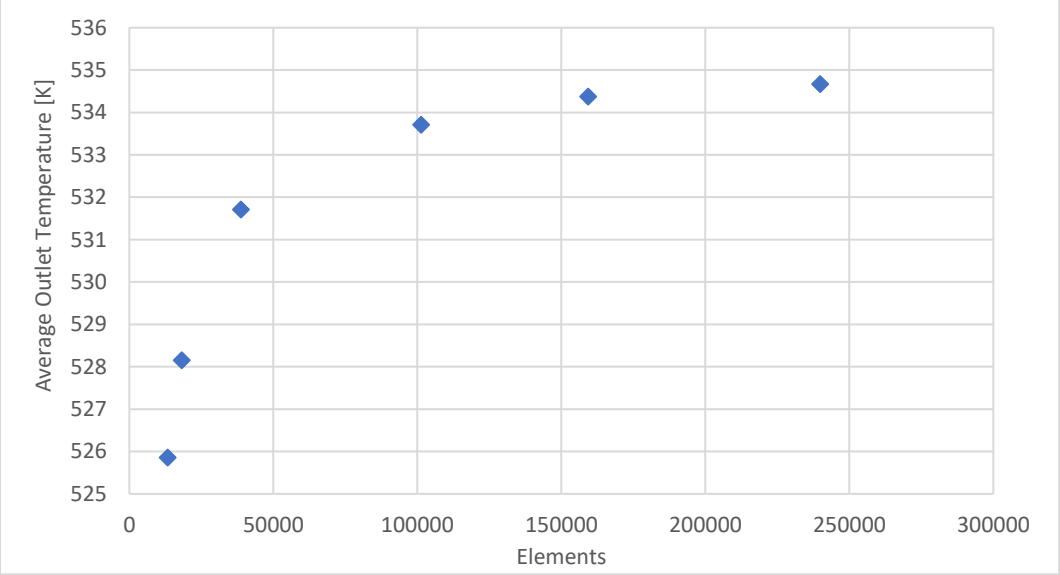

Figure 33: Convergence study of the average outlet temperature as a function of the number of elements for the CFD model.

Although acceptable convergence was achieved after 150,000 nodes, the finest mesh discretization scheme was used in the remaining trials which resulted in an average outlet temperature of 535 K for the 0.35 MW rack.

To quantify the numerical uncertainty on the simulation, a Richardson extrapolation has been performed. This practice has been recommended and discussed by multiple standards [79] [80] and [81]. Consider the functional solution of a grid, *f*, of which *h* is the step size and *C* is a constant. Assuming that the

solution is in the form of a power series, the error, *E*, between the grid-free solution and discretized solution can be expressed as the step size raised to a constant, *p*, with higher order terms denoted by $O(h^k)$. This is shown in Equation 8.4.1 where *k* represents constants greater than *p* and *h* is less than one [107].

$$E = f(h) - f_{exact} = C\,h^p + O(h^k) \tag{8.4.1}$$

The term *p* is defined as the order of grid convergence. The first and largest term of the power series for the error, Ch^p, is of particular interest.

Using multiple solutions of varying step size, the error arising from the largest term can be eliminated and a more exact solution can be determined after ignoring the higher order errors. The approximation in Equation 8.4.2 is known as a Richardson extrapolation [82].

$$f_{exact} \approx f(h_i) + \frac{f(h_i) - f(h_j)}{r^p - 1} \tag{8.4.2}$$

For the proper implementation of this technique, the solution must be within the asymptotic range.

The term on the right-hand side may be considered an estimator for the absolute uncertainty [107]. The error is expected to scale with the value of the solution, and for that reason, relative errors are more appropriate for estimating the error in temperatures and mass fluxes from other heat loads. The equation to calculate the relative error is shown in Equation 8.4.3.

$$E = \frac{|f(h_i) - f(h_j)|}{f(h_i)\,(r^p - 1)} \tag{8.4.3}$$

It should be noted that Equation 8.4.3 is equal to the absolute error shown in the Richardson extrapolation divided by the finest discretized solution.

The grid refinement ratio, *r*, is defined as the larger step size divided by the smaller one (i.e., $r = h_i/h_j$). If a uniform grid refinement ratio is used with three data points, Equation 8.4.4 may be used to calculate the grid refinement [107].

$$p = \ln\left(\frac{f(h_i) - f(h_j)}{f(h_j) - f(h_k)}\right) / \ln(r) \tag{8.4.4}$$

Alternatively, the logarithm of Equation 8.4.1 and regression techniques may be used to determine the grid convergence if a sufficient number of well-behaved points exist.

The functions $f(h_i)$, $f(h_j)$, and $f(h_k)$ represent progressively more coarse solutions, respectively, with the differences between step sizes h_i, h_j and h_k specified by a constant grid refinement ratio. To ensure that errors are indeed due to their discretization rather than other numerical errors such as computer round-off or iteration errors, a minimum refinement ratio of $r \geq 1.3$ is recommended [80].

In the application of the described uncertainty analysis to heat transfer calculations, the solution $f(h_i)$ is considered the difference between the outlet and the ambient temperature. The step size in the simulations has been assumed to be inversely proportional to the number of elements.

Table 10: Summary of results from examining the CFD result's numerical uncertainty due to grid convergence

	Value
Grid refinement ratio	1.54
Order of convergence	1.939
Absolute error estimate	0.2 K

Relative error estimate	0.1%

For the three most detailed simulations in the convergence study shown in Figure 33, the grid refinement ratio is approximately 1.54. The order of convergence is 1.939 calculated via Equation 8.4.4. The approximation of the outlet temperature using Equation 8.4.2 yields 534.9 K with a numerical discretization error of 0.2 °C. This discretization error translates to a relative error of 0.1%. Uncertainties for the numerical discretization are not reported in the following tables and plots because it is known that the discretization error represents only a small part of the simulation uncertainty. The uncertainties arising due to modelling assumptions and input uncertainty will likely be greater than 1%, and for that reason instead only three significant digits are shown in the CFD results.

The results for the analytical and CFD model are summarized in Table 10 and Table 11. The additional mass flux through the bottom of the rack for the CFD model is also indicated in Table 12.

*Table 11: Summary of average temperatures and average mass fluxes for the analytical and CFD model for a 0.35 MW fuel rack. The average net bottom mass flux has been assumed to be zero for the analytical and finite difference models**

	Analytical	CFD	Finite Difference
Avg. Outlet Temperature [K]	539	535	558
Avg. Top Mass Flux [kg/s/m^2]	1.29	1.33	1.16
Avg. Side Mass Flux [kg/s/m^2]	0.163	0.154	0.147
Avg. Outlet Density [kg/m^3]	0.655	0.660	0.633
Avg. Specific Heat Capacity [J/kg/K]	1022.8	1024.1	1020.1
Maximum Top Mass Flux [kg/s/m^2]	-	2.65	2.61
Avg. Net Bottom Mass Flux [kg/s/m^2]	0*	0.102	0*

An average outlet temperature of 535 K (262 °C) and average top mass flux of 1.33 kg/s/m^2 was observed in the CFD model. Alternatively, the throughput may be expressed as a mass flow of 2.1 kg/s or average velocity of 7.2 km/h. The average outlet temperature was calculated using the values in Table 11 and conservation of energy (see Equation 5.3.1).

The temperatures predicted by the finite difference model were significantly higher than the CFD and analytical model. It was initially suspected that the higher temperatures could have been due to an under predicted inlet velocity. However, Figure 34 shows that a higher inflow at the bottom inlet has little influence on the outlet temperatures. For an average mass flux inflow of 0.3 kg/m^2 s (three times the inflow predicted by the CFD) the average vertical mass flux is approximately equivalent to the zero-mass flux inflow at a height of 0.5 m. Therefore, temperatures will be slightly lower at the base of the rack where there is a high mass flux at the bottom, but the outlet temperature will be unaffected.

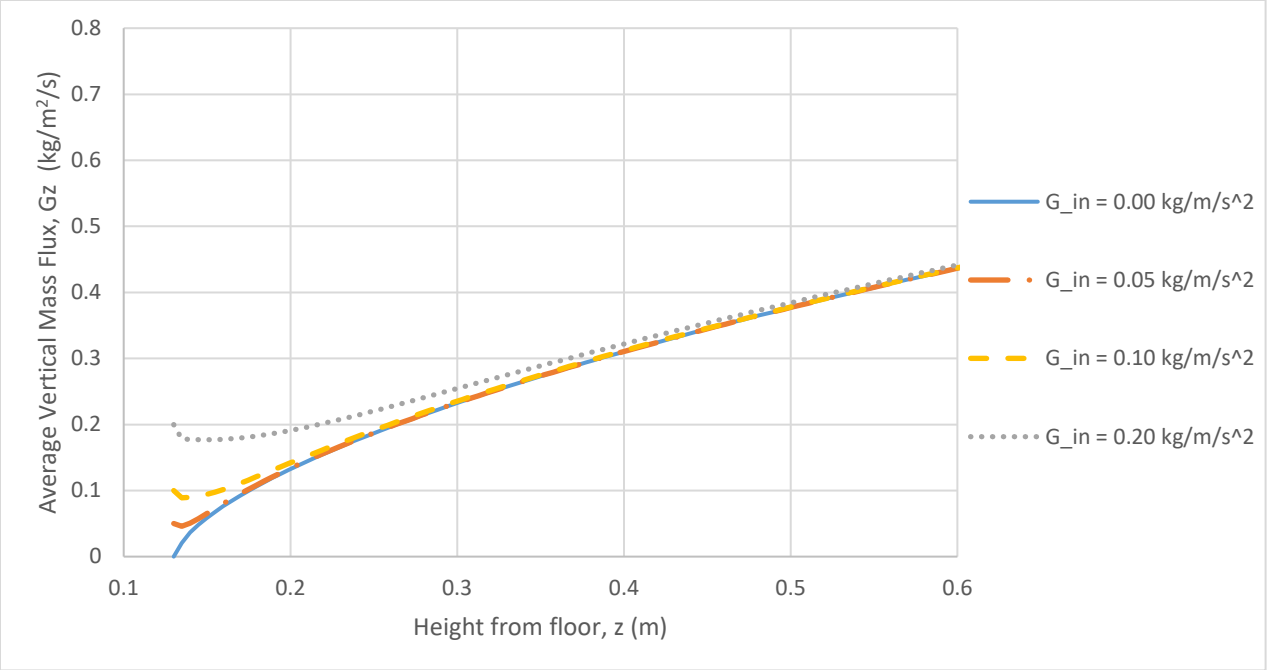

Figure 34: Vertical mass flux as a function of height for a 0.35 MW racks with various inlet mass fluxes.

Another suspected cause for the disagreement between models was due to difficulties in determining the shape factor (which is defined by the ratio of the average to max mass flux in the *xy* plane of the rack). As previously discussed, a paraboloid with zero flux at the edges and its maximum value at the centre will have a maximum to average ratio of 4/9. This is an appropriate assumption for a fully developed flow, but it is uncertain whether rack flows meet such criteria.

To explore its effect of different shape factors, the average vertical mass flux as a function of height was modelled in Figure 35. The CFD data points were created by extracting data from slices in COMSOL post-processor, which resulted in some distortion due to the smoothing and averaging.

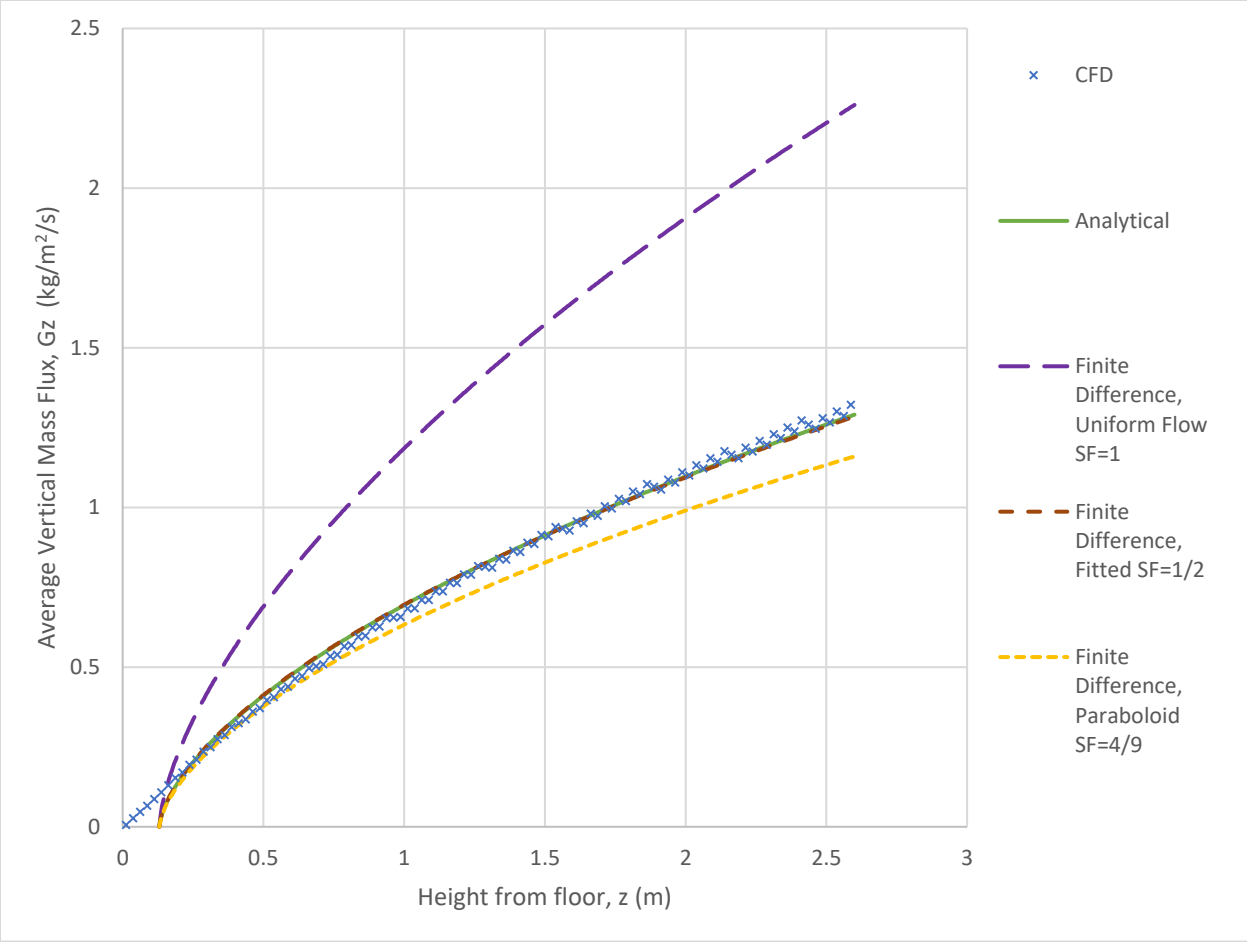

Figure 35: Comparison of finite difference models' (with various shape factors), analytical model's and CFD model's vertical mass flux as a function of height.

The analytical and CFD models agree well with each other across the height of the rack. However, the finite difference model was highly influenced by the shape factor. Assuming a flow profile was perfectly uniform resulted in a much higher outlet flux rate at 2.26 kg/m^2 s and lower average outlet temperature 469 K was predicted. Conversely, a paraboloid-shaped flow profile predicted an outlet mass flux of 1.16 kg/m^2 s which overestimates the outlet temperature at 558 K. An intermediary shape factor of ½ was chosen based on the maximum to average flow ratio of the CFD (perhaps this could be derived). The resulting temperature of 540 K and mass flux 1.28 kg/m^2 s agreed with the CFD model, and especially well with the analytical model.

To further evaluate the consistency of the models, the thermal power of the rack and the discharge coefficient, C_d, in the analytical model was varied to examine its effect on the outlet temperature as shown in Figure 36. Varying the discharge coefficient was justified as there were some slight discrepancies between values reported in literature for the thermal chimneys and large openings in enclosures. Akbarzadeh has recommended a discharge coefficient of 0.57 for their experimental setup [102] as previously noted, while Andersen suggested a typical value of 0.65 in his original paper [99]. Alternatively, correlations based on the Reynolds number for thin walled openings [108] may be used to determine a value for the discharge coefficient. Assuming the Reynolds number is $\approx 1 \times 10^5$, the discharge coefficient can still be taken as about 0.6 [14].

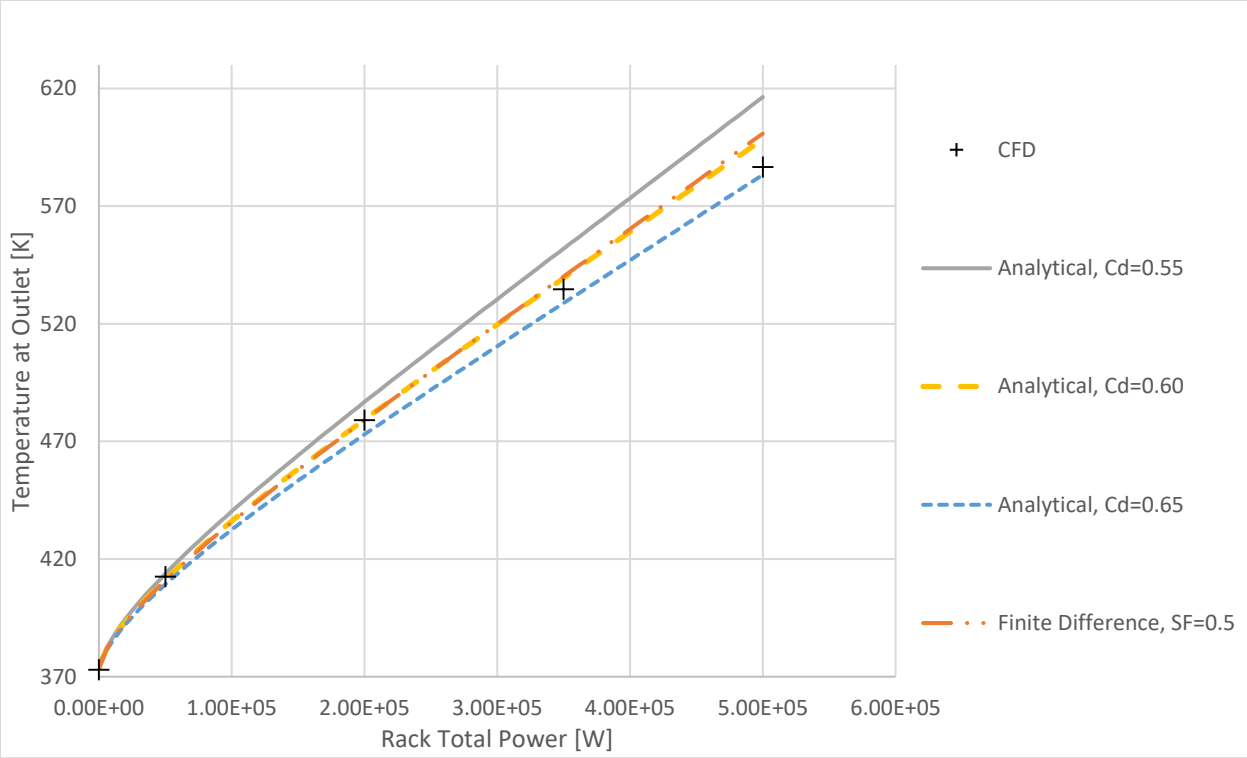

Figure 36: Comparison of finite difference model's, analytical models' (with various discharge coefficients (C_d)) and CFD model's outlet temperatures as a function of the rack thermal output.

The change in temperature was within ±13 K in response to a ± 0.05 change to the discharge coefficient for the base case of 0.35 MW. A higher coefficient resulted in more airflow through the rack and therefore lower temperatures, as expected. The difference between the analytical model and the CFD increased at higher rack powers. It was found the finite difference model with a shape factor of 1/2, matched extremely well with the analytical model when the discharge coefficient, C_d, was at its default value 0.6.

One of the primary advantages of the CFD model is that it allows for the spatial temperature and velocity fields to be resolved. As shown in Figure 37 and 38, and Table 12, the maximum temperature of the air within the rack was about 575 K and located at the centre of the outlet.

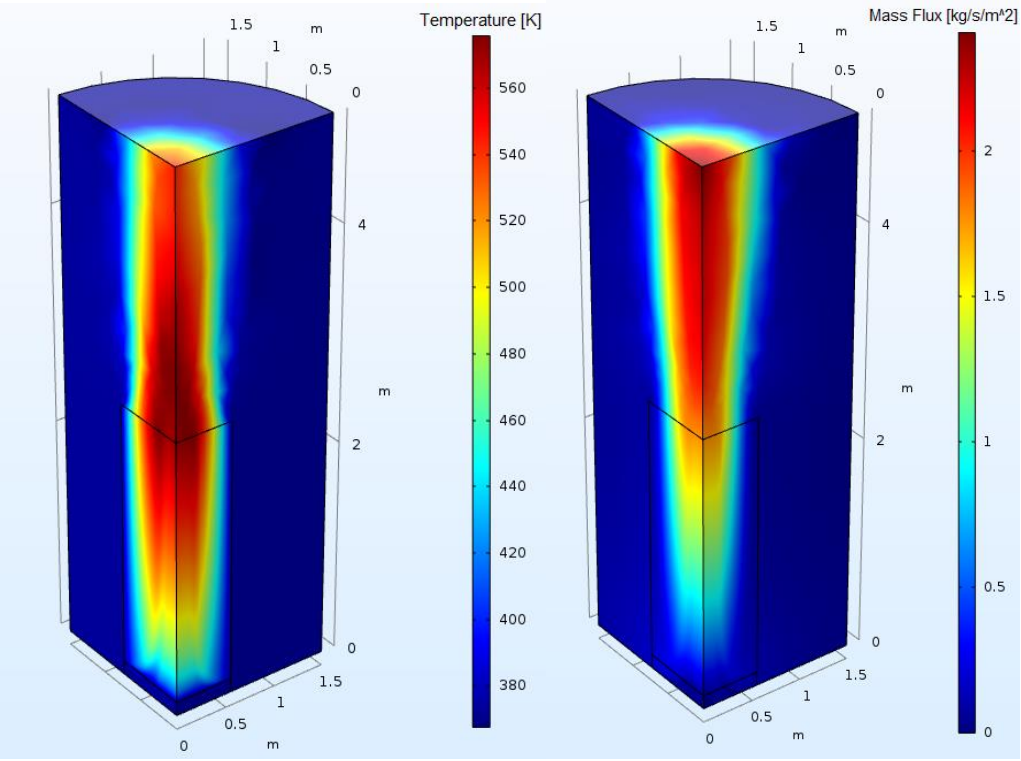

Figure 37 and 38: Steady-state temperature (left in Kelvin) and mass flux (right in kg/s/m^2) profiles are shown for the laminar CFD model.

The rack's maximum mass flux was similarly located at the intersection of the symmetry planes and increased with the height as it approached the outlet.

Table 12: Comparison of local mass flux and temperatures in the laminar CFD model for a 0.35 MW fuel rack.

	CFD
Avg. Wide Side Mass Flux [kg/s/m^2]	0.150
Avg. Narrow Side Mass Flux [kg/s/m^2]	0.160
Avg. Net Bottom Mass Flux [kg/s/m^2]	0.102
Total Mass Backflow in Bottom [kg/s]	4.70 x10^{-4}
Maximum Temperature [K]	576

The flow was unidirectional through the main openings, entering through the sides and exiting through the top. The wide 0.7 m side had a slightly lower inflow than the narrow 0.5 m side. The net flow through the bottom of the rack was 0.1 kg/s/m^2 in the upward direction. The gross backflow at the bottom of the rack was about 5 x10^{-4} kg/s, potentially due to vortices at the base of the rack.

8.5. Discussion

The analytical model estimated slightly higher outlet temperatures than the CFD model for the tested cases. The differences between the models could be due to the opening at the rack bottom in the CFD geometry, simplifications implicit in the single zone theory or error in the discharge coefficient. The CFD model is considered to be more accurate because it simulates the unheated bottom compartment and

makes the least assumptions about the direction of the flow. The finite difference model over predicted the outlet temperatures relative to the others when a parabolic flow profile is assumed. If the maximum to average ratio is taken directly from the CFD as 1/2 instead of the assumed 4/9 value based on a paraboloid flow profile, excellent agreement is obtained with the analytical model over the height of the rack and the applicable range of thermal outputs. Good predictions of the max and average values of the heat flux are also achieved at the outlet. The paraboloid shape was originally chosen because it was similar to fully developed flow in tubes, however further research has shown that the proposed flow profile does not match numerical solutions for fully developed flow through a rectangular cross-section by White [109]. His solution for a fully developed, laminar flow profile through a square pipe is graphically shown in its non-dimensionalized form in Figure 39.

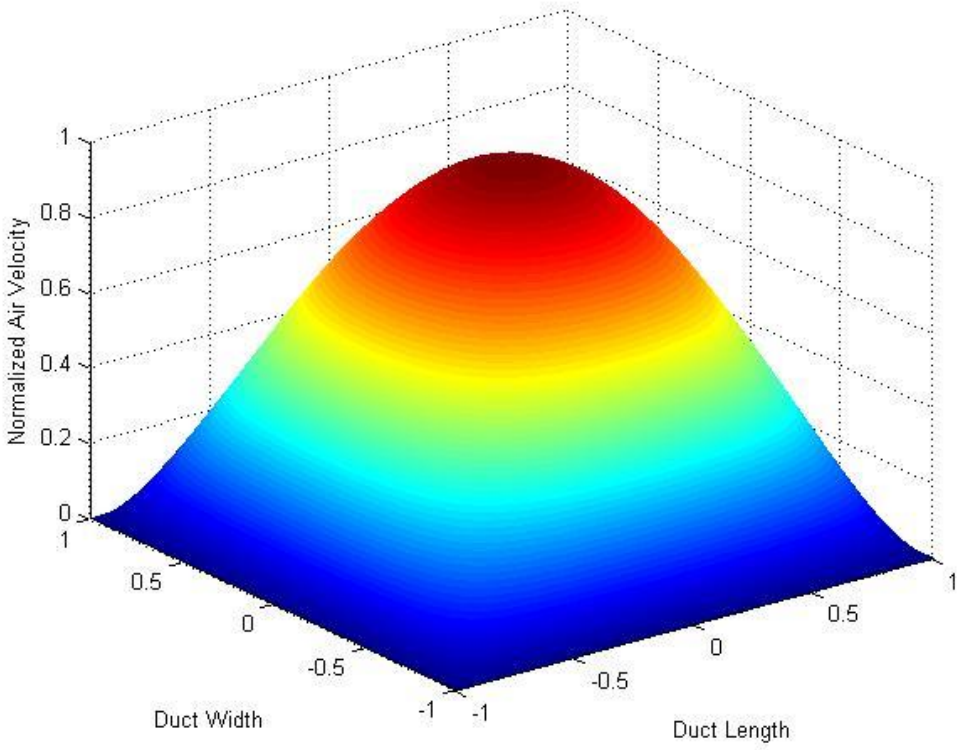

Figure 39: Velocity profile for laminar, fully developed flow in a rectangular duct. The maximum velocity has been normalized to one, as have the extents of the duct's width and length.

Using the more accurate profile, the maximum to average velocity ratio may be calculated to be 0.476 which is closer to the expected result of 1/2. Other possibilities for the deviation could be due to its many simplifications, such as the use of a shape factor which is uniform over the entire height of the rack and the approximate evaluation of the *xy* direction Navier-Stokes equation. The results of the finite difference model were considered to be the least accurate.

While comparisons of the models to previous experiments (which are limited) would be a useful validation exercise, there are several concerns, which prevent this from being practicable and applicable. A clear problem is that a heated volume source without any resistance to flow is an unphysical system. Heated boundary conditions are normally implemented in experiments via resistance heating; however the best-case use of wires in an evenly distributed grid would then introduce flow resistance and lead to errors. Chemically heating the volume would not be effective either due to the poor spatial control of the reactants in the air. Specialized instrumentation would be required to closely reproduce the results of the

proposed models. To the author's knowledge, there are no existing experiments in literature that are suitable for validation purposes.

Another fundamental issue with validation is that the proposed models are already known to not fully describe a spent fuel rack after a loss of coolant. Flow impedance is a geometry specific phenomenon that is extremely important in natural convection problems. Preliminary models have demonstrated the mass fluxes through the rack will be lower than those determined in this simplified analysis. Instead of a final product, the models should be considered as a first step toward the solution and lower bound for expected temperatures. The models provide an important clarification on previous work [45] and reaffirms the importance of work in this area. The model, indeed, could be used for supporting experimental design.

Again, it must be emphasized that the direct applicability of the study would be limited to scenarios where the internal flow resistance does not constitute a significant effect. This means only scenarios where a small number of freshly discharged bundles are sparsely distributed on a rack. Although the models consistently showed that the ambient temperatures in a freshly loaded fuel rack will be higher than previously assumed [16] [45] and this will negatively affect the maximum fuel sheath temperature (e.g., the figure of merit of the accident), the maximum temperature of the air within the rack was about 575 K and located at the centre of the outlet.

9. CONCLUSIONS

The presented work examined the maximum sheath and air temperatures incurred by a LOCA in an IFB. The examination of an individual bundle under transient and steady-state conditions suggested that the vast majority of bundles in a pool would not undergo a breakaway reaction if the ambient temperatures remain low and only the freshest (less than two weeks since discharge) were at risk of a severe fuel failure. Results suggest there is sufficient time for operators to intervene and prevent a breakaway oxidation for the hottest bundles from an IFB, provided they are isolated. Comparisons were also made to earlier published iterations of the model [83], those existing in open literature [16] [93] and experiments [94], which confirmed the validity of the model's temperatures at steady-state. Differences in the model's results were primarily due to the use of different oxidation correlations, and the specification of a uniform boundary heat flux instead of a volumetric heat source. More realistic modelling in both of these areas indicate that there is slightly more safety margin than previously indicated due to internal conduction within the elements. Ballooning of the bundle rods may challenge the passive cooling capacity of the bundle, but this behaviour is only expected for highly pressurized or defected elements. For highly deformed elements with strains up to 10%, the temperature increase induced was less than 100 K for a 2 kW bundle in air. Therefore, although both strain (and its effect on cooling) and conduction inside fuel elements were listed as highly important phenomena in the PKPIRT, it may not be necessary to model these effects depending on the accuracy required for a given application. Temperature criterions may be used to predict the onset of defects due to overpressure as was shown in this work. If it is found that a large number of bundles in the bay are expected to defect, more study may be warranted to fully understand the effect of ballooning on convection.

The current 2D cross-section model represents the first published model that simulates the transient behaviour of a CANDU bundle during an IFB LOCA. While there is still potential for improvement in the oxidation modelling process (through the implementation of a semi-empirical prediction of breakaway and post-breakaway linear reaction kinetics), accounting for neighbouring bundles was identified as the most important phenomena to be included.

As a first step towards quantifying the flow for multiple bundles in a rack and verifying a previous analysis [45], the problem was simplified by ignoring flow resistances. A finite difference, analytical and CFD model were then developed to predict the air temperatures in a rack. The agreement between the three model's outlet temperatures over the range of rack powers and spatially over the rack's height offers a strong verification case. The finite difference model was observed to have issues regarding its dependence on the unknown shape factor. The temperatures observed were well below that required for a breakaway reaction, but higher than previous analysis suggested [45]. The flow resistance of the bundles and rack, once accounted for, will impede the mass flux through the rack and thereby further increase the temperatures at the outlet. The models demonstrate that the air will heat up significantly and move discharged fuel temperatures closer to the threshold at which breakaway oxidation may occur during a severe LOCA in an IFB.

Preliminary work qualitatively indicates flow resistance has a crucial role in determining the final outlet temperatures and therefore it must be incorporated before the impact on the maximum fuel sheath temperature is fully understood. The primary goals of future work is to create models based on vertically arranging 2D bundle cross-section in a CFD analysis to better understand the bulk flow and temperature of the air in a rack. The model may then be extended to porous media representations to understand the entire IFB. If it is found that temperatures in the porous media models and the severe accident code developed by CNL reach temperatures of elevated concern, it may be advisable to distribute hot bundles on the racks as done in American LWR SFPs. However, no unreasonable safety issues have yet been identified for LOCA in CANDU wet storage, and it remains an area of ongoing research.

10. FUTURE WORK

While no analyses in the body of this report demonstrated unacceptable risks associated with a LOCA in the IFB, it does support the notion that further work is needed to define the existing safety margins. In the individual bundle cross-section model, some of the assumptions that characterized the analysis could have arguably been interchanged or refined for more realistic results. The existence of such limitations does not alter the conclusions of the presented work, but are listed here for completeness and to ensure future researchers are aware of these shortcomings. For the most part, the issues arose from identifying and accessing high quality oxidation model data, the omission of important phenomena (i.e. flow resistance) and uncertainties with regards to heat transfer characteristics of spent fuel.

As mentioned in the stress-strain analysis, better quality information on the internal pressures, fluence, voidage, and material properties of CANDU irradiated fuel would have enhanced predictions. For example, the material was assumed to be unirradiated, which translates to a higher than normal ductility in the sheath of the spent fuel. Another limitation was in using low and upper bounds for the internal pressure. Had a realistic initial pressure been known, it could have been used to estimate when a best estimate of what temperatures would induce fuel sheath overstrain. Since the event is categorized as a BDBA, the use of best estimate with uncertainty methods is more acceptable in safety analyses and such best-estimate techniques will assuredly be utilized in the severe accident code in development by CNL.

One additional issue is that the effect of appendages has not been considered. With regards to temperature, appendages tend to increase the amount of turbulence and thereby may enhance heat transfer in the bundle. In the stress-strain analysis however, it is hypothesized that spacer and bearing pads restrict the element's ability to expand and reduce its internal pressure. This will lead to higher stresses and the initiation of defects earlier than predicted via these methods. However, more advanced studies in finite element studies or experiments would be required to confirm this notion. After the aforementioned issues have been resolved, the methods applied here could be used to predict the temperature at which fuel failures from sheath overstrain would occur, ideally with comparisons made to the stress-strain parameters from the AECL code ELESTRES.

In the 2D single bundle analysis, a few improvements could be made. The assumption that the fuel-cladding gap was effectively filled with fission gas greatly degraded the thermal conductivity compared to a helium gas fill. A best-estimate simulation may have assumed the pellet retained the majority of fission products and that a mix closer to the original fill gas would remain. However, there is a poor amount of data openly available to describe the internal pressure and content of the fill gas in spent CANDU fuel. For this reason, a sensitivity study for the steady-state scenario was performed and the conservative approach was taken in the transient analyses.

There are also shortcomings in the current oxidation model. Firstly, it does not fully describe the breakaway transition. The model applies a parabolic growth profile for pre-breakaway oxidation and then uses modified reaction constants and the same parabolic relations to represent a breakaway reaction, as done in MELCOR 2.1. However, the post breakaway regime is most commonly described by linear reaction kinetics phenomena according to literature [40] [110]. For long reaction times, the model will diverge from the real solution as the oxide layer's thickness increases. This results in a peak, rather than an asymptotic or runaway temperature as would be expected. COMSOL offers the versatility to describe a range of ordinary differential equations and functions, so linear kinetics could be easily implemented in theory. The issue lies in acquiring the correlations and experimental data to precisely describe the reaction constants. The data for LWR cladding exist and have been already integrated in severe accident codes such as ASTEC and ATHLET-CD [110], but the theory manuals for such severe accident codes are not freely available. Summaries of their oxidation models are available in literature [51] [111] and could have likely been used to replicate their models, but this would have been beyond the intended scope of the project.

The current formulation of the oxidation process also employs a purely empirical approach to breakaway through the lifetime integral. This method integrates the amount of time spent at a temperature and compares it to the total amount of time for breakaway to occur at that same temperature. It is a highly intuitive procedure, but its validation basis is only for isothermal conditions. Semi-empirical approaches such as those developed by the Paul Scherrer Institute (PSI) [109] [110] with a critical oxide thickness [112] [113] would represent a step forward in the modelling process and have been included in MELCOR. However, as with the parabolic versus linear kinetics issue, additional information is required to implement this. Experiments also may be necessary to assure accurate results are obtained, as CANDU sheaths are of a lower thickness than those in LWRs, which is a characteristic that may affect the critical oxide thickness.

However, the overarching conclusions drawn remain largely unchanged. The propensity for breakaway reactions in an IFB during a loss of coolant has not been established and thus the correlations from the MELCOR theory manual have been considered acceptable. If it can be shown breakaway on a large scale would be likely, it would be worthwhile to request additional information to extend the model's capabilities.

In the individual rack analyses, the incorporation flow resistance remains an area of future work and will need to be included in a severe accident code. The most straightforward extension is to stack the 2D bundle cross-sections with either symmetry boundary conditions or open boundaries on the sides and designate the top and bottom as open boundaries in a Multiphysics analysis software. These two scenarios respectively represent a rack with an infinite row width and unidirectional flow from the bottom to top, and a single bundle in each row and maximized side flow. The case where the channel is closed by symmetry planes will be a conservative representation of IFB convection ignoring the effect of racks and granted there is a wide spacing between the racks and the surrounding walls and floors. The open single stack will be another lower bound representation of temperatures expected. Afterwards, the analysis may be extended to multiple racks using 2D porous media models and eventually 3D models. The 3D porous media model treatment has already been conducted by the USNRC to study the flow patterns expected in a LWR SFP [96] and would give valuable insight for CANDU IFB. Once properly calibrated, it would be the ideal comparison tool for a severe accident code.

However, a major challenge associated with such an analysis would be accurately determining the constants for its flow resistance. Due to the different flow resistances associated with different orientation of the bundles, an anisotropic model would be required. The constants would also change dramatically depending on the types of fuel racks as shown in Figure 40.

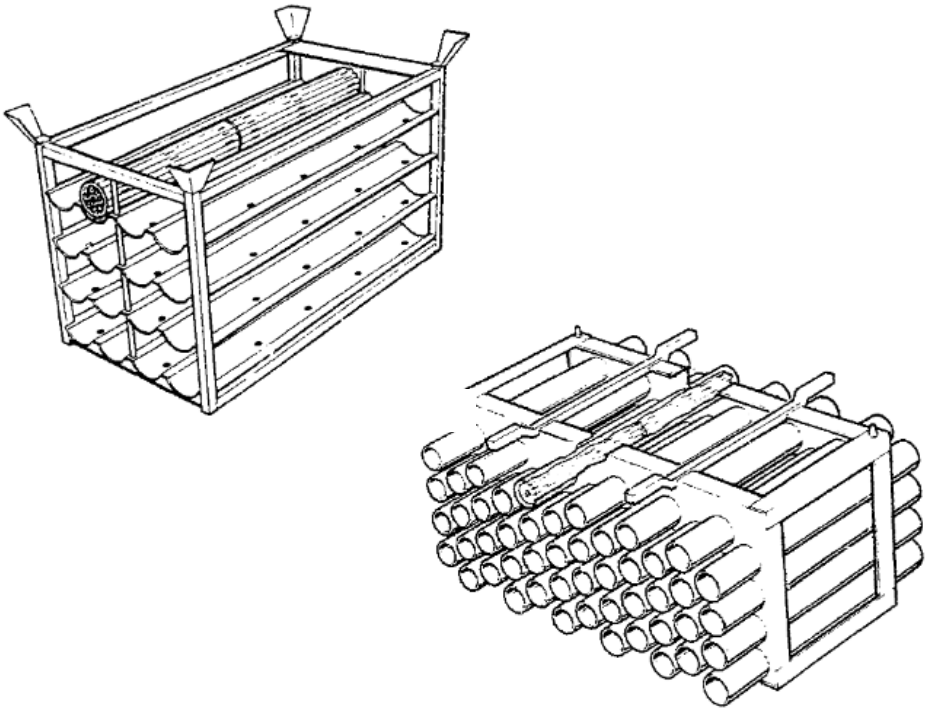

Figure 40: IFB storage racks for CANDU nuclear generating stations [114]. Due to the closed nature of certain modules, airflows and thus convective heat transfer would become constricted.

Performing isothermal simulations with specified inlet mass flows could be used to determine the pressure drop and thus the porous media parameters, but accounting for turbulence in the model is not an easy task. Furthermore, effects such as radiative heat transfer and oxidation are not well suited to steady-state or porous media model, so its applicability may be limited to the low temperature regime. The benefits of such a model however, include the ability to examine flows on a larger scale than would be accessible using detailed representations of the geometry and could reliably determine whether an accident would escalate and in how long.

REFERENCES

[1] World Nuclear Association, "Nuclear Power in the World Today," WNA, Jan 2017. [Online]. Available: http://www.world-nuclear.org/information-library/current-and-future-generation/nuclear-power-in-the-world-today.aspx.

[2] International Atomic Energy Agency, "Energy, Electricity and Nuclear Power Estimates for the Period up to 2050," IAEA, Vienna, 2016.

[3] S. Schlömer, T. Bruckner, L. Fulton, E. Hertwich, A. McKinnon, D. Perczyk, J. Roy, R. Schaeffer, R. Sims and P. Smith, "Annex III: Technology-specific Cost and Performance Parameters," in *Climate Change 2014: Mitigation of Climate Change. Contribution of Working Group III to the Fifth Assessment Report of the Intergovernmental Panel on Climate Change*, New York, Cambridge University Press, 2014, pp. 1329-1356.

[4] European Nuclear Society, "Nuclear power plants, world-wide," ENS, largest nuclear society for science and industry, 2016. [Online]. Available: https://www.euronuclear.org/info/encyclopedia/n/nuclear-power-plant-world-wide.htm. [Accessed 2018].

[5] World Nuclear Association, "Nuclear Power in Canada," WNA, Nov 2016. [Online]. Available: http://www.world-nuclear.org/information-library/country-profiles/countries-a-f/canada-nuclear-power.aspx.

[6] Canadian Nuclear Association, "CANDU Technology," CNA, 2015. [Online]. Available: https://cna.ca/technology/energy/candu-technology/.

[7] Bruce Power, "Life-Extension Program," BP, 2016. [Online]. Available: http://www.brucepower.com/about-us/life-extension/.

[8] Ontario Power Generation, "Darlington Refurbishment," OPG, 2016. [Online]. Available: http://www.opg.com/generating-power/nuclear/stations/darlington-nuclear/darlington-refurbishment/Pages/default.aspx.

[9] Independent Electricity System Operator, "Ontario Energy Report Q3," IESO, Toronto, 2016.

[10] Canadian Nuclear Safety Commission, "High-level Radioactive Waste," Government of Canada, 5 Dec 2016. [Online]. Available: http://nuclearsafety.gc.ca/eng/waste/high-level-waste/index.cfm.

[11] H. Fan, R. Aboud, W. Z. E. Choy and H. Liu, "Spent Fuel Response after a Postulated Loss of Spent Fuel Bay Cooling Accident," in *33rd Annual Conference of the Canadian Nuclear Society, 36th Annual CNS/CNA Student Conference*, Saskatoon, 2012.

[12] NEA Committee on the Safety of Nuclear Installations, "Status Report on Spent Fuel Pools under Loss-of-Cooling and Loss-of-Coolant Accident Conditions Final Report.," Organisation for Economic Cooperation and Development, 2015.

[13] N. Foust, "The Future Of Fukushima Daiichi Spent Fuel," SimplyInfo.org, 2012. [Online]. Available: http://www.fukuleaks.org/web/?p=8638.

[14] U.S. Nuclear Regulatory Commission, "NUREG-2157 Generic Environmental Impact Statement for Continued Storage of Spent Nuclear Fuel," Washington, D.C, 2014.

[15] World Nuclear Association, "Fukushima Accident," WNA, Jan 2017. [Online]. Available: http://www.world-nuclear.org/information-library/safety-and-security/safety-of-plants/fukushima-accident.aspx.

[16] W. G. C.J. Krasnaj, "Development of a 2-D Finite Element Model to Examine Both Natural Convection and Radiative Cooling of a Spent Bundle in Air," in *The 19th Pacific Basin Nuclear Conference (PBNC 2014)*, Vancouver, 2014.

[17] W. G. C.J. Krasnaj, "Finite Element Analysis of Heat Transfer between Spent CANDU Fuel Bundles in Spent Fuel Pools," in *The 19th Pacific Basin Nuclear Conference (PBNC 2014)*, Vancouver, 2014.

[18] C. K. M. S. W. Grant, "CNSC – Irradiated Fuel Bay Loss of Cooling Severe Accident Work," in *The 13th International Conference on CANDU Fuel*, Kingston, 2016.

[19] M. G. Mukesh Tayal, "Chapter 17 Fuel," in *The Essential CANDU, A Textbook on the CANDU Nuclear Power Plant Technology*, Hamilton, UNENE, 2014, pp. 1-72.

[20] Nuclear Waste Management Organization, "Ensuring Safety: Multiple-Barrier System," NWMO, Toronto, 2015.

[21] B. Ade and I. Gauld, "Decay Heat Calculations for PWR and BWR Assemblies fuel with Uranium and Plutonium Mixed Oxide Fuel Using Scale," Oak Ridge National Laboratory, U.S. Department of Energy, Oak Ridge, 2011.

[22] J. Baschuk, "Summary Of The Second PKPIRT Panel On Severe Accidents In A CANDU Irradiated Fuel Bay [memo]," Canadian Nuclear Laboratories, Ottawa, 2016.

[23] Nuclear Engineering International, "Transnuclear racks up the orders," Global Trade Media, May 2010. [Online]. Available: http://www.neimagazine.com/news/newstransnuclear-racks-up-the-orders.

[24] R. Page, "Canadian Nuclear Fuel," Atomic Energy of Canada Limited, Sheridan Parks, ON, 1974.

[25] A. Benjamin, D.McCloskey, D. Powers and S. Dupree, "Spent Fuel Heatup Following Loss of Water during Storage," Sandia Laboratories, U.S. Nuclear Regulatory Commission, Washington, 1979.

[26] Y. Song, J. Jung and S. Nijhawan, "Assessment of Spent CANDU Fuel Bundle Behaviour Following a Pool Loss Of Coolant and Consideration of Potential Zircaloy Fires Using KAERI's Dedicated CANDU Spent Fuel Bay Computer Code FUELPOOL," in *Water Reactor Fuel Performance Meeting*, Jeju, Korea, 2017.

[27] B. Hamilton, "Fukushima 5 years later: 2011 disaster by the numbers," CBC News, 10 Mar 2016. [Online]. Available: http://www.cbc.ca/news/world/5-years-after-fukushima-by-the-numbers-1.3480914.

[28] International Atomic Energy Agency, "Energy, Electricity and Nuclear Power Estimates for the Period up to 2050," IAEA, Vienna, 2010.

[29] C. K. M. S. W. Grant, "CNSC - Irradiated Fuel Bay Loss of Cooling Severe Accident Work," in *13th International Conference on CANDU Fuel*, Kingston, 2016.

[30] Canadian Nuclear Safety Commission, "“CNSC Integrated Action Plan On the Lessons Learned

From the Fukushima Daiichi Nuclear Accident”," Government of Canada, Ottawa, 2013.

[31] National Research Council, Committee on the Safety and Security of Commercial Spent Nuclear Fuel Storage , "Chapter 3: Spent Fuel Pool Storage," in *Safety and Security of Commercial Spent Nuclear Fuel Storage: Public Report*, Washington D.C., The National Academies , 2006, p. 44.

[32] P. Chatelard and N. Reinke, "Overview of the integral code ASTEC V2.0," Institut de Radioprotection et de Sûreté Nucléaire, Gesellschaft für Anlagen- und Reaktorsicherheit (GRS) gGmbH, Fontenay-aux-Roses, 2009.

[33] Gesellschaft für Anlagen-und Reaktorsicherhei (GRS) mbH, "ATHLET Mod 3.1 Cycle A Program Overview," 2016. [Online]. Available: https://www.grs.de/sites/default/files/fue/overview31a.pdf.

[34] Electric Power Research Institute, "Modular Accident Analysis Program," July 2012. [Online]. Available: https://www.epri.com/#/pages/product/000000000001025795/.

[35] Sandia National Laboratories, "MELCOR," U.S. National Research Council, 2015. [Online]. Available: http://energy.sandia.gov/energy/nuclear-energy/nuclear-energy-safety-technologies/melcor/.

[36] Committee on Lessons Learned from the Fukushima Nuclear Accident for Improving Safety and Security of U.S. Nuclear Plants; Nuclear and Radiation Studies Board; Division on Earth and Life Studies; National Academies of Sciences, Engineering, and Medicine, "Lessons Learned from the Fukushima Nuclear Accident for Improving Safety and Security of U.S. Nuclear Plants: Phase 2," National Academies Press (US), Washington, 2016.

[37] S. Durbin, E. Lindgren, A. Goldman, M. Zavisca, Z. Yuan, A. Krall, M.Khatib-Rahbar, G. A. Zigh and S.Gonzalez, "Spent Fuel Pool Project Phase I: Pre-Ignition and Ignition Testing of a Single Commercial 17x17 Pressurized Water Reactor Spent Fuel Assembly under Complete Loss of Coolant Accident Conditions," United States National Regulatory Commission, 2016.

[38] S. Durbin, E. Lindgren, L. Humphries, Z. Yuan, M. Zavisca, M. Khatib-Rahbar, R. Beaton, G. A. Zigh and S.Gonzalez, "NUREG/CR Spent Fuel Pool Project Phase II: Pre-Ignition and Ignition Testing of a 1x4 Commercial 17x17 Pressurized Water Reactor Spent Fuel Assemblies under Complete Loss of Coolant Accident Conditions," United States National Regulatory Commission, 2016.

[39] M. Steinbrück and M. Böttcher, "Air oxidation of Zircaloy-4, M5 and ZIRLO™ cladding alloys at high temperatures," *Journal of Nuclear Materials*, vol. 414, p. 276–285, 2011.

[40] C. Duriez, M. Steinbrück, D. Ohai, T. Meleg, J. Birchley and T. Haste, "Separate-effect tests on zirconium cladding degradation in air ingress situations," *Nuclear Engineering and Design*, no. 239, pp. 244-253, 2009.

[41] C. Duriez, T. Dupont, B. Schmet and F. Enoch, "Zircaloy-4 and M5 high temperature oxidation and nitriding in air," *Journal of Nuclear Materials*, vol. 380, pp. 30-45, 2008.

[42] C. Krasnaj and W. Grant, "Development of a 2-D Finite Element Model to Examine Both Natural Convection and Radiative Cooling of a Spent Fuel Bundle in Air [Poster]," in *19th Pacific Basin Nuclear Conference*, Vancouver, 2014.

[43] I. Hastings, "Post irradiation Stability and Fission Product Behaviour of Defected UO2 fuel at 400°, 600° and 900°C in Air,," in *American Ceramic Society Annual Meetingm May 5-9*, Cincinnati, 1985.

[44] J. Baschuk., "Summary of the Second PKPIRT Panel on Severe Accidents in a CANDU Irradiated Fuel Bay," Canadian Nuclear Laboratories (Memo)., Chalk River, 2016.

[45] R. Henry, "Phenomena Assessment Worksheet [Supporting Descriptions for the REH PIRT Tables]," Second PKPIRT Panel on Severe Accidents in a CANDU Irradiated Fuel Bay, 2016.

[46] J. Novak and G. Miller, "Dry Fuel Handling Station Experience and Ontario Hydro (CNS) Programs," International Conference on CANDU Fuel, Chalk River, 1986.

[47] S. B. Author, "Will nuclear fission bring world fusion?," Science Museum of Minnesota, [Online]. Available: http://www.sciencebuzz.org/buzz-tags/uranium-235. [Accessed January 2017].

[48] R. A. E. C. W. Z. a. H. L. H.Z. Fan, "Spent Fuel Response after a Postulated Loss of Spent Fuel Bay Cooling Accident," in *33rd Annual Conference of the Canadian Nuclear Society, 36th Annual CNS/CNA Student Conference*, Saskatoon, 2012.

[49] United States Nuclear Regulatory Commission, "Oxidation of Zircaloy by Steam and Oxygen, ML010670322," 2012. [Online]. Available: https://www.nrc.gov/docs/ML0106/ML010670322.pdf.

[50] K. Natesan and W. Soppet, "Air Oxidation Kinetics for Zr-Based Alloys," United States Nuclear Regulatory Commission, Argonne National Laboratory, Washington, 2004.

[51] E. Beuzet, F.Haurais, C. Bals, O. Coindreau, L. Fernandez, A. Vasiliev and S. Park, "Cladding oxidation during air ingress. Part II: Synthesis of modeling results," in *The 7th European Review Meeting on Severe Accident Research*, Marseille, 2015.

[52] E. T. Hayes and A. H. Roberson, "Some Effects of Heating Zirconium in Air, Oxygen, and Nitrogen," *Journal of The Electrochemical Society,* vol. 96, no. 3, pp. 142-151, 1949.

[53] S. Leistikow and H. Berg, "Investigation under nuclear safety aspects of zircaloy-4 oxidation kinetics at high temperatures in air," in *Proc.of the 2nd Workshop of German and Polish Research on High Temperature Corrosion of Metals*, Juelich, 1989.

[54] COMSOL, "COMSOL Multiphysics Reference Manual Version 4.3," 2012.

[55] A. G. Y. Cengel, Heat and Mass Transfer: Fundamentals & Applications Fourth Edition, New York: McGraw Hill, 2011.

[56] D. G. M. Cohen, "The Hemicube Method: A Radiosity Solution for Complex Environments," *SigGraph,* vol. 19, no. 3, pp. 31-40, 1985.

[57] A. Ross and R. Stoute, "Heat Transfer Coefficient Between UO2 and Zircaloy-2," Atomic Energy of Canada Limited, Chalk River, 1962.

[58] D. Olander, Fundamental Aspects of Nuclear Reactor Fuel Elements, Berkeley (USA): California University. Dept. of Nuclear Engineering, 1976.

[59] S. Palleck, R. Sejnoha and B. Wong, "Bundle Uranium Content And Performance Of Candu Fuel," AECL Fuel Design Branch, Mississauga, 1997.

[60] R. William, "CANDU Owners Group Reports ELOCA 2.2 Theory Manual 153-113400-COG-012 Revision 0," Atomic Energy of Canada Limited, Mississauga, 2008.

[61] H. Von Ubisch, S. Hall and R. Srivastav, "Thermal Conductivities of Mixtures of Fission Product Gases With Helium and Argon," in *International Conference on Peaceful Uses of Atomic Energy,*

Geneva, 1958.

[62] J. Lenoir and e. al., "Measurement and Correlation of Thermal Conductivities of Gases at High Pressures," *Chemical Engineering Prog.*, vol. 49, p. 539, 1953.

[63] C. Westbye, A. Brito, J. Mackinnon, H. Sills and V. Langman, "Fuel Thermal/Mechanical Behaviour under Loss Of Coolant Accident Conditions as Predicted by the FACTAR Code," Ontario Hydro Reactor Safety and Operational Analysis Department, Toronto, 1995.

[64] P. Reid and R. Gibb, "Fuel Sheath Integrity For Fuel Bundles at Decay Power Levels at 600 C in steam," Point Lepreau Nuclear Generating Station, Saint John, 1995.

[65] D. Hardy, "High Temperature Expansion and Rupture Behaviour of Zircaloy Tubing," Fuel Engineering Branch, AECL, Chalk River, 1973.

[66] T. K. Sawarn, S. Banerjee, S. S. Sheelvantra, J. Singh and V. Bhasin, "Study of clad ballooning and rupture behaviour of Indian PHWR fuel pins under transient heating condition in steam environment," *Journal of Nuclear Materials*, vol. 495, pp. 332-342, 2017.

[67] D. Hagrman, "Zircaloy Cladding Shape at Failure (BALON2)," Idaho National Engineering Laboratory, Idaho Falls, 1981.

[68] Idaho National Engineering and Environmental Laboratory, "NUREG/CR-6150, SCDAP/RELAP5/MOD 3.3 Code Manual MATPRO a Library of Material Properties for Light Water Reactor Accident Analysis," U.S. Nuclear Regulatory Commission, Idaho Falls, 2001.

[69] Idaho National Engineering Laboratory, "NUREG-1180 MATPRO Version 10: A Handbook of Material Properties for use in the analysis of Light Water Reactor Fuel Rod Behaviour," U.S. Nuclear Regulatory Commission, Idaho Falls, 1978.

[70] K. Geelhood, C. Beyer and W. Luscher, "PNNL Stress/Strain Correlation for Zircaloy," Pacific Northwest National Laboratory (PNNL), Richland, Washington, 2008.

[71] R. S. W. Shewfelt, "The Ballooning of Fuel Cladding Tubes: Theory and Experiment," AECL, Whiteshell Nuclear Research Establishment, Pinawa, Manitoba, 1987.

[72] MATLAB, "fzero, Zero of a function of one variable," MATLAB Function Reference, [Online]. Available: http://www.thphys.nuim.ie/CompPhysics/matlab/help/techdoc/ref/fzero.html. [Accessed 2018].

[73] Atomic Energy of Canada Limited (AECL), "Computer Code Documentation for Calculation & Analyses, ELESTRES-CANFLEX 1.2 Theory Manual," AECL, Mississauga, Ontario, 2004.

[74] U. Viswanathan, S. Anantharaman and K. Sahoo, "Measurement of Fission Gas Release from Irradiated Nuclear Fuel Elements, Report BARC/2005/E/026," Bhabha Atomic Research Centre, Mumbai, 2005.

[75] I. Tuturici, M. Parvan, R. Dobrin, M. Popov, R. Radulescu and V. Toma, "The Post-Irradiation Examination of CANDU Type Fuel Irradiated in the Institute for Nuclear Research Triga Reactor," Romanian Power Authority, Nuclear Energy Group, Pitesti, 1996.

[76] T. Collins and G. Hubbard, "NUREG-1738, Technical Study of Spent Fuel Pool Accident Risk at Decommissioning Nuclear Power Plants," United States Nuclear Regulatory Commission, Washington, DC, 2001.

[77] R. W. R. M. M.R. Tonks, "Chapter 22: Finite Element Modelling," in *State-of-the-Art Report on Multi-scale Modelling of Nuclear Fuels*, Nuclear Energy Agency of the OECD (NEA), 2015, pp. 337-343.

[78] D. Gaston, C. Permann, J. Peterson, A. Slaughter, D. Andrš, Y. Wang, M. Short, D. Perez, M. Tonks, J. Ortensi, L. Zou and R. Martineau, "Physics-based multiscale coupling for full core nuclear reactor simulation," *Annals of Nuclear Energy,* vol. 84, pp. 45-54, 2015.

[79] W. L. Oberkampf and T. G. Trucano, "Verification and Validation in Computational Fluid Dynamics," Sandia National Laboratories, Albuquerque, New Mexico, 2002.

[80] American Society of Mechanical Engineers, "Standard for Verification and Validation in Computational Fluid Dynamics and Heat Transfer," ASME International, New York, 2009.

[81] National Aeronautics and Space Administration, "Uncertainty and Error in CFD Simulations," NPARC Alliance CFD Verification and Validation Web Site, 2008. [Online]. Available: https://www.grc.nasa.gov/www/wind/valid/tutorial/errors.html.

[82] L. F. Richardson, "The approximate arithmetical solution by finite differences of physical problems including differential equations, with an application to the stresses in a masonry dam," *Philosophical Transactions of the Royal Society,* vol. 210, p. 307–357, 1911.

[83] D. Logtenberg, P. Chan and E. Corcoran, "Fuel Behaviour After a Loss of Coolant in an Irradiated Fuel Bay," in *37th Annual Conference of the Canadian Nuclear Society and 41st Annual CNS/CNA Student Conference [Pending Acceptance]*, Niagara Falls, 2017.

[84] J. Park, J. Jung and E. Ryu, "CHF Enhancement of Advanced 37-Element Fuel Bundles," *Science and Technology of Nuclear Installations,* vol. 2015 , p. 10, 2015.

[85] SCDAP/RELAP5-3D Code Development Team, "Volume 4: MATPRO - a library of Materials Properties for Light-Water-Reactor Accident Analysis," Idaho National Engineering and Environmental Laboratory, Idaho Falls, 2003.

[86] International Atomic Energy Agency, "Thermophysical properties database of materials for light water reactors and heavy water reactors, Final report of a coordinated research project," IAEA-TECDOC-1496, Vienna, Austria, 2006.

[87] S. Yang, "Improvement of the basic correlating equations and transition criteria of natural convection heat transfer," *Heat Transfer - Asian Research,* vol. 30, no. 4, pp. 293-300, 2001.

[88] J. C. Dixon, "Appendix B Properties of Air," in *The Shock Absorber Handbook Second Edition*, West Sussex , John Wiley & Sons, 2007, pp. 375-378.

[89] J. E. Dennis and .. H. W. Mei, "Two new unconstrained optimization algorithms which use function and gradient values," *Journal of Optimization Theory and Applications,* vol. 28, no. 4, p. 453–482, 1979.

[90] A. Straccia, "Viscosity Ramping Improves the Convergence of CFD Models," COMSOL Inc., 2016. [Online]. Available: https://www.comsol.com/blogs/viscosity-ramping-improves-the-convergence-of-cfd-models/.

[91] Atomic Energy Control Board, "Draft Regulatory Guide C-006 Safety Analysis of Candu Nuclear Power Plants," AECB, Ottawa, 1999.

[92] H. Kampf and G. Karsten, "Effect of Different Types of Void Volumes on the Radial Temperature Distribution of Fuel Pins," *Nuclear Applied Technology,* vol. 9, p. 288, 1970.

[93] P. Sermer, "An Analytical Model for Heat Transfer Within a CANDU Fuel Bundle residing in Air," in *International Conference on CANDU Fuel*, Chalk River, 1986.

[94] J. Schenk, J. Whelan and R. Graham, "Investigation of the Decay Heat-Up of two 37-element Electrically Heated Fuel Bundles in a Bruce and Darlington Air Chamber," AECL Research, Thermalhydraulics Development Branch, Chalk River, 1993.

[95] A. Sarchami, "Investigation of Thermal Hydraulics of a Nuclear Reactor Moderator," Mechanical and Industrial Engineering Department, University of Toronto, Toronto, 2011.

[96] C. Boyd, "Predictions of Spent Fuel Heatup After a Complete Loss of Spent Fuel Pool Coolant," U.S. Nuclear Regulatory Commission, Washington, DC, 2000.

[97] H. Nourbakhsh, G. Miao and Z. Cheng, "Analysis of Spent Fuel Heatup Following Loss of Water in a Spent Fuel Pool, A Users' Manual for the Computer Code SHARP," U.S. Nuclear Regulatory Commission, Washington, 2002.

[98] Y. Li, "Buoyancy-driven natural ventilation in a thermally stratified one zone building," *Building and Environment,* no. 35, pp. 207-214, 2000.

[99] K. T. Andersen, "Theory for natural ventilation by thermal buoyancy in one zone with uniform temperature," *Building and Environment,* no. 38, pp. 1281-1289, 2003.

[100] Y. Li, A. Delsante and J. Symons, "Prediction of natural ventilation in buildings with large openings," *Building and Environment* , no. 35, pp. 191-206, 2000.

[101] N. K. Bansal, R. Mathur and M. Bhandari, "Solar Chimney for Enhanced Stack Ventilation," *Building and Environment,* vol. 3, no. 28, pp. 373-377, 1993.

[102] A. Akbarzadeh, W. Charters and D. Lesslie, "Thermocirculation characteristics of a Trombe wall passive test cell," *Solar Energy,* vol. 6, no. 28, pp. 461-468, 1982.

[103] K. Andersen, "Theoretical considerations on natural ventilation by thermal buoyancy," *ASHRAE 101,* vol. 2, pp. 1103-1117, 1995.

[104] F. V. d. M. J. R. C. Flourentzou, "Natural Ventilation for passive cooling: measurement of discharge coefficients," *Energy and Buildings,* vol. 27, pp. 283-292, 1998.

[105] Z. Li, "Characteristics of Buoyancy Driven Natural Ventilation through horizontal openings, PhD Thesis," Department of Civil Engineering, Aalborg University, 2007.

[106] COMSOL, "COMSOL Multiphysics Reference Manual Version 5.3," 2017.

[107] National Aeronautics And Space Administration, "Examining Spatial (Grid) Convergence," NPARC Alliance CFD Verification and Validation Web Site, 2008. [Online]. Available: https://www.grc.nasa.gov/www/wind/valid/tutorial/spatconv.html.

[108] I. E. Idelchik, Handbook of Hydraulic Resistance 3rd Edition, Boca Raton: CRC Press, 1994.

[109] F. M. White, Viscous Fluid Flow Third Edition, Boston: McGraw-Hill, 2006.

[110] J. Stuckert, Z. H. A. Kiselev and M. Steinbrück, "Cladding oxidation during air ingress. Part I:

Experiments on air ingress," *Annals of Nuclear Energy,* vol. 96, pp. 4-17, 2016.

[111] O. Coindreau, C. Duriez and S. Ederli, "Air oxidation of Zircaloy-4 in the 600–1000 °C temperature range: Modeling for ASTEC code application," *Journal of Nuclear Materials,* vol. 405, no. 3, pp. 207-215, 2010.

[112] J. Birchley and L. Fernandez-Moguel, "Simulation of air oxidation during a reactor accident sequence: Part 1 - Phenomenology and model development," *Annals of Nuclear Energy,* no. 40, pp. 163-170, 2011.

[113] L. Fernandez-Moguel and J. Birchley, "Simulation of air oxidation during a reactor accident sequence: Part 2 – Analysis of PARAMETER-SF4 air ingress experiment using RELAP5/SCDAPSIM," *Annals of Nuclear Energy,* vol. 40, p. 141–152, 2012.

[114] H. N. Isaac, "Session 1 - Irradiated Fuel Management Strategies, Written Contribution," in *Irradiated Fuel Storage: Operating Experience and Development Programs, International Workshop*, Toronto, ON, 1984.

[115] D. Logtenberg, "Spent Fuel Behaviour after a Loss of Coolant in an Irradiated Fuel Bay," in *UNENE Workshop Poster Session*, Waterloo, 2016.

[116] J. Choi, W. Ko and C. Kang, "Reference Spent Fuel and Its Characteristics for a Deep Geological Repository Concept Development," *Journal of the Korean Nuclear Society,* vol. 31, no. 6, pp. 23-28, 1998.

[117] A. Oussoren, "Towards a Mechanistic Model for Stress Corrosion Cracking in Nuclear Fuel Elements," A Thesis Submitted to the Division of Graduate Studies of the Royal Military College of Canada, Kingston, 2015.

[118] Energie NB Power, "Nuclear," 2018. [Online]. Available: www.nbpower.com/en/about-us/learning/learn-about-electricity/nuclear/.

[119] World Nuclear Association, "The Nuclear Fuel Cycle," 2017. [Online]. Available: www.world-nuclear.org/information-library/nuclear-fuel-cycle/introduction/nuclear-fuel-cycle-overview.aspx.

[120] D. Hardy, "High Temperature Expansion and Rupture Behaviour of Zircaloy Tubing," in *Specialist Meeting on Safety of Water Reactor Fuel Elements*, Saclay, 1973.

[121] N. M. Mohamed and A. Badawib, "Effect of DUPIC Cycle on CANDU Reactor Safety Parameters," *Nuclear Engineering and Technology,* vol. 48, no. 5, pp. 1109-1119, 2016.

[122] J. Birchley and L. Fernandez-Moguel, "Simulation of air oxidation during a reactor accident sequence: Part 1 – Phenomenology and model development," *Annals of Nuclear Energy,* vol. 40, p. 163–170, 2012.

[123] I. Idel'chik, "Handbook of Hydraulic Resistance, Coefficients of Local Resistance and of Friction," Israel Program for Scientific Translations, Jerusalem, 1966.

[124] A. Akbarzadeh, W. Charters and D. Lesslie, "Thermocirculation characteristics of a Trombe wall passive test cell," *Solar Energy,* vol. 6, no. 28, pp. 461-468, 1982.

APPENDIX A: MATLAB SCRIPT INPUTS AND OUTPUTS

Sheath Stress-Strain Calculations

The purpose of this code is to predict the sheath expansion at a given temperature due to the internal pressure of an element. The code is supporting work for a Master's Level Thesis at the Royal Military College which was supervised by P.Chan and E.Corcoran. Last modified October 21st, 2018.

```
%Clean up, clear previous results and models
clear all
close all
clc

%%%%%%%%%%%%%%%%%%%%%%%%%%%%%%%%%%%%%%%%%%%%%%%%%%%%%%%%%%%%%%%%%%%%%%%%%%%%%%%
% Initialize Constants of Stress-Strain Problem
disp('Strain stress')
Pa=1e5;                          %Pa, coolant pressure
P_int=[2e6,.2e6];                %Pa, fuel internal pressure (from high to low)
Ta=373;                          %K, ambient temperature
R=13.08e-3/2;                    %m, sheath external radius
rO=(13.1-.4)/1e3;                %m, sheath internal radius
rp=(13.1-.4-.08)/1e3;            %m, pellet radius
w=.38e-3;                        %m, sheath thickness
strain_rat=[1e-5,1e-4,1e-3];     %/s, true strain rate (from low to high)
A1=.5;          %anisotropy coefficient in axial direction for stress and strain
A2=.5;          %anisotropy coefficient in circumfrential direction for stress and strain
A3=.5;          %anisotropy coefficient in radial direction for stress and strain
t=400:1:1400;   %K, temperatures the fuel is subjected to
%t_cel=t-273.15;%degC, temperatures the fuel is subjected to


%%%%%%%%%%%%%%%%%%%%%%%%%%%%%%%%%%%%%%%%%%%%%%%%%%%%%%%%%%%%%%%%%%%%%%%%%%%%%%%
% Initialize temperature and strain dependent material properties of Zirc
% Note heavisides are used to connect the temperature dependent
% piecewise functions

% Young's Modulus
Youngs_mod_1=@(T) 114.8e9-.0599e9*T;  %[AECL, ELESTRES]

% Strength coefficient
K=@(T) heaviside(730-T).*(1.0884e9-T*1.0571e6)+... %[MATPRO, NUREG-6150]
    heaviside(T-730).*heaviside(900-T).*(-8.152540534e9+T*3.368940331e7-
T.^2*4.317334084e4+T.^3*1.769348499e1)...
    +heaviside(T-900).*exp(8.755+8663./T);
K2=@(T) heaviside(750-T).*(1.17628e9+4.54859e5*T-3.28185e3*T.^2+1.72752*T.^3)+... %[Pacific
Northwest National Laboratory (PNNL)]
    heaviside(T-750).*heaviside(1090-T).*(2.522488e6.*exp(2.8500027e6./T.^2))+...
    heaviside(T-1090).*heaviside(1255-T).*(1.841376039e8-1.4345448e5*T)+...
    heaviside(T-1255).*heaviside(2100-T).*(4.330e7-6.685e4*T+3.7579e1*T.^2-7.33e-3*T.^3);

% Strain rate sensitivity constant
m=@(T,k)heaviside(730-T).*.02+... %[MATPRO, NUREG-6150]
    heaviside(T-730).*heaviside(900-T).*(2.063172161e1-T*7.704552983e-2+T.^2*9.50484306e-5-
```

```
T.^3*3.860960716e-8)+...
    heaviside(T-900).*heaviside(1172.5-T).*(-6.47e-2+T*2.203e-4+...
    heaviside(T-1090)*6.78e-2*log(6.34e-3/(strain_rat(k))).*((T-1090)/82.6))+...
    heaviside(T-1172.5).*heaviside(1255-T).*(-6.47e-2+2.203e-4*T+...
    6.78e-2.*(1255-T)/82.6.*log(6.34e-3./(strain_rat(k))))+...
    heaviside(T-1255).*heaviside(2100-T).*(-6.47e-2+T*2.203e-4);

m2=@(T)heaviside(750-T).*.015+... %[PNNL]
    heaviside(T-750).*heaviside(800-T).*(7.458e-4*T-.544338)+...
    heaviside(T-800).*(3.24124e-4*T-.20701);

% Strain/work hardening exponent
n=@(T) heaviside(1099.0772-T).*(-9.490e-2+T.*1.165e-3-T.^2*1.992e-6+T.^3*9.588e-10)+... %[MATPRO,
NUREG-6150]
    heaviside(1600-T).*heaviside(T-1099.0772).*(-0.22655119+2.5e-4*T)+...
    heaviside(T-1600)*0.17344880;
n2=@(T) heaviside(850-T).*(-1.86e-2+T*7.110e-4-T.^2*7.721e-7)... %[MATPRO, NUREG-1180]
    +heaviside(T-850).*.027908;
n3=@(T) heaviside(419.4-T)*.11405+... % [PNNL without adjustments for fluence (same as NUREG-
6150)]
    heaviside(T-419.4).*heaviside(1099.08-T).*(-9.49e-2+T*1.165e-3-T.^2*1.992e-6+T.^3*9.588e-
10)+...
    heaviside(T-1099.08).*heaviside(1600-T).*(-.22655119+2.5e-4.*T)+...
    heaviside(T-1600)*.17344880;

% Calculating adjusted strain hardening exponent [MATPRO, NUREG-6150]
% Used to calculate nprime, little other documentation
ANL=@(T)heaviside(730-T)*.17+...
    heaviside(780-T).*heaviside(T-730).*(0.056*T-11.218)+...
    heaviside(T-780).*.95;
% The adjusted strain hardening exponent, nprime, replaces n in the
% stress-strain equations, when the strain is less than n^2/(1+m)
nprime=@(T, mE,k) min(ANL(T),n(T).^2./(1+m(T,k))/mE)

%%%%%%%%%%%%%%%%%%%%%%%%%%%%%%%%%%%%%%%%%%%%%%%%%%%%%%%%%%%%%%%%%%%%%%%%%%%%%%%
% Initialize stress variables in the axial (1), circumferential (2) and
% radial (3) directions, determine effective stress from those variables
% Other stresses are expressed as a function of the hoop stress
sigma_2= @(T, mE,P)(P.*T/Ta*(r0^2-rp^2)./((exp(mE)*r0).^2-rp^2)-Pa)*R/w;  %Circumferential/Hoop
stress, [Pa]
sigma_1= @(T, mE,P) sigma_2(T, mE,P)./2;                                  %Axial stress, [Pa]
sigma_3= @(T, mE,P) -sigma_2(T, mE,P)*w/R/2;                              %Radial stress, [Pa]
sigma_eff= @(T, mE,P)(A1*(sigma_1(T, mE,P)-sigma_2(T, mE,P)).^2+...       %effective stress, [Pa]
    A2*(sigma_2(T, mE,P)-sigma_3(T, mE,P)).^2+...
    A3*(sigma_3(T, mE,P)-sigma_1(T, mE,P)).^2).^.5;

% Convert from effective strain to hoop strain and radial strain
E_hoop=@(mE) mE*sqrt(2)*((A1+A3)-A1/2-A3*w/2/r0)/sqrt((1/2)^2+(1-w/2/r0)^2+(1/2-w/2/r0)^2); %
Hoop Strain
E_rad=@(mE) mE*sqrt(2)*(-A3-A2/2+(A3+A2)*w/R/2)/sqrt((1/2)^2+(1-w/2/r0)^2+(1/2-w/2/r0)^2);  %
Radial Strain

%%%%%%%%%%%%%%%%%%%%%%%%%%%%%%%%%%%%%%%%%%%%%%%%%%%%%%%%%%%%%%%%%%%%%%%%%%%%%%%
```

```
% Calculate maximum true strain

for i=1:length(strain_rat) % Cycle through all strain rates
    for k=1:length(P_int)  % Cycle through all internal pressures
        for j=1:length(t)  % Cycle through all temperatures
            %%%%%%%%%%%%%%%%%%%%%%%%%%%%%%%%%%%%%%%%%%%%%%%%%%%%%%%%%%%%%%%%
            %%MATPRO, NUREG-6150
            %Effective Plastic Strain Equation
            %Function is an equation of the maximum strain, max_Ep
            fun_1=@(max_Ep) max_Ep-
(sigma_eff(t(j),E_hoop(max_Ep),P_int(k))./K(t(j))./(max([strain_rat(i), 1e-
5])*1e3).^m(t(j),i)).^(1./n(t(j)));
            %Solved by taking the minimum root via the fzero function
            %note indexes are (strain rate, Internal pressure, temperature)
            sol_maxEp(i,k,j)= fzero(fun_1,0);

            %Effective Elastic Strain Equation
            %Function is an equation of the maximum strain (max_Ep)
            fun_2=@(max_Ee) max_Ee-sigma_eff(t(j),E_hoop(max_Ee),P_int(k))./Youngs_mod_1(t(j));
            %Solved by taking the minimum root via the fzero function
            sol_maxEe(i,k,j) = fzero(fun_2,0);

            %Effective Plastic Strain Equation with adjusted strain
            %hardening exponent
            %Function is an equation of the maximum strain (max_Ep)
            fun_3=@(max_Ep) max_Ep-
(sigma_eff(t(j),E_hoop(max_Ep),P_int(k))./K(t(j))./(max([strain_rat(i), 1e-
5])*1e3).^m(t(j),i)).^(1./nprime(t(j),max_Ep,i));
            %Solved by taking the minimum root via the fzero function
            sol_maxEp_adjusted(i,k,j) = fzero(fun_3,0);

            %Determine which solution is appropriate for each step
            %Adjusted strain hardening exponent solution replaces the
            %normal solution when the strain is less than n^2/(1+m)
            %The maximum strain between the elastic and plastic is taken
            %since their intersection is where it changes behaviour
            if(sol_maxEp(i,k,j)<n(t(j))/(1+m(t(j),i)))
                sol_maxE(i,k,j)=max(sol_maxEp_adjusted(i,k,j),sol_maxEe(i,k,j));
            else
                sol_maxE(i,k,j)=max(sol_maxEp(i,k,j),sol_maxEe(i,k,j));
            end

            %%%%%%%%%%%%%%%%%%%%%%%%%%%%%%%%%%%%%%%%%%%%%%%%%%%%%%%%%%%%%%%%
            %%PNNL
            %Effective Plastic Strain Equation
            %Function is an equation of the maximum strain, max_Ep
            fun_4=@(max_Ep) max_Ep-
(sigma_eff(t(j),E_hoop(max_Ep),P_int(k))./K2(t(j))./(max([strain_rat(i), 1e-
5])*1e3).^m2(t(j))).^(1./n3(t(j)));
            %Solved by taking the minimum root via the fzero function
            %note indexes are (strain rate, Internal pressure, temperature)
            sol_maxEp2(i,k,j)= fzero(fun_4,0);
```

```
            %Determine which solution is appropriate for each step
            %The maximum strain between the elastic and plastic is taken
            %since their intersection is where it changes behaviour
            sol_maxE2(i,k,j)=max(sol_maxEp2(i,k,j),sol_maxEe(i,k,j));
        end
    end
end

%%%%%%%%%%%%%%%%%%%%%%%%%%%%%%%%%%%%%%%%%%%%%%%%%%%%%%%%%%%%%%%%%%%%%%%%%%%%%%%
%%Display the MATPRO, NUREG-6150 results for each pressure and strain rate

Legend=cell(length(P_int)*length(strain_rat),1);% initialize legend variable
N=1;                                            % initialize legend counter
for j=1:length(P_int)        % sweep through internal pressures
    for i=1:length(strain_rat)  % sweep through strain rates
        %Auto add each data sweep to the plot with its unique colour
        semilogy(t,squeeze(E_hoop(sol_maxE(i,j,:))),'Color',[ i/(length(strain_rat)+1)
(length(P_int)-j)/(length(P_int)) j/(length(P_int))])
        hold on  %keep adding to plot until done sweeping
        %add to the legend variable
        Legend{N}=strcat(num2str(P_int(j)/1e6),' MPa, strain rate=',num2str(strain_rat(i)),'/s');
        N=N+1;
    end
end
legend(Legend); %add legend using legend variable
xlabel('Temperature [K]') %add labels
ylabel('Hoop Strain')
hold off %stop adding to this plot

%%Display results of MATPRO, NUREG-6150 compared to PNNL using Case 1
% (1st pressure and strain rate specified)
figure()
semilogy(t, squeeze(E_hoop(sol_maxE(1,1,:))), t,squeeze(E_hoop(sol_maxE2(1,1,:))),'-.',t,
squeeze(E_hoop(sol_maxE(1,2,:))),':', t,squeeze(E_hoop(sol_maxE2(1,2,:))),'--')
xlabel('Temperature [K]') %add labels and legends
ylabel('Hoop Strain at a srain rate of 1e-5/s')
legend('2 MPa, MATPRO, NUREG-6150','2 MPa, PNNL','0.2 MPa, MATPRO, NUREG-6150','0.2 MPa, PNNL')


%%Predict time to strain for the MATPRO, NUREG-6150 results using stepwise
% approximations
figure() %create new figure
delT=zeros(length(t),length(P_int)); %initialize solution variable
for j=1:length(P_int)
    for i=1:length(strain_rat)
        %assume that the time to reach the max strain for the smallest strain
        %rate is simply the max strain/strain rate (this will overpredict
        %the time)
        if i==length(strain_rat)
            delT(:,j)= delT(:,j)+squeeze(E_hoop(sol_maxE(i,j,:)))/strain_rat(i);
        %for other strain rates assume that the difference between the
        %max strains is estimated by dividing by the next smallest strain
        %rate
```

```
        else
            delT(:,j)= delT(:,j)+(squeeze(E_hoop(sol_maxE(i,j,:)))-
squeeze(E_hoop(sol_maxE(i+1,j,:))))/strain_rat(length(strain_rat)-i);
        end
    end
    Legend2{j}=strcat(num2str(P_int(j)/1e6),' MPa'); %prepare legend variable
    %Automatically plot the data for each internal pressure and convert to
    %minuts by dividing by 60s (Suppressed)
    %plot(t,delT(:,j)/60,'Color',[ j/(length(strain_rat)+1) (length(P_int)-j)/(length(P_int))
j/(length(P_int))])
    hold on
end

%Manually plot data for each internal pressure to differentiate lines for
%white and black plots
plot(t,delT(:,1)/60,t,delT(:,2)/60,'--')

legend(Legend2); %add labels and legends
xlabel('Temperature [K]')
ylabel('Time to reach a strain rate of 1e-5/s [min]')
box on
%Check whether calculation on strain time predictions was properly executed

%initialize variables for test
E_hoop_HP =squeeze(E_hoop(sol_maxE(1,1,:)));
E_hoop_HP_HS =squeeze(E_hoop(sol_maxE(2,1,:)));
E_hoop_HP_HHS =squeeze(E_hoop(sol_maxE(3,1,:)));

%predict time to strain
delT_test= E_hoop_HP_HHS/1e-3 + (E_hoop_HP-E_hoop_HP_HS)/1e-4+(E_hoop_HP_HS-E_hoop_HP_HHS)/1e-5;

%check difference (this value should be zero)
error_check=sum(delT(:,1)-delT_test)

%%%%%%%%%%%%%%%%%%%%%%%%%%%%%%%%%%%%%%%%%%%%%%%%%%%%%%%%%%%%%%%%%%%%%%%%%%%%%%%
% Debugging Functions

% Plot all effective strains
figure()
semilogy(t,squeeze(sol_maxEe(1,1,:)),'.',t,squeeze(sol_maxEp(1,1,:)),...
    t,squeeze(sol_maxEp_adjusted(1,1,:)),'-.',t,squeeze(sol_maxE(1,1,:)),...
    '--', t,n(t)./(1+m(t,1)),':')
%add legends and labels
legend('Elastic','Plastic','Plastic adjusted','Solution', 'Conditioner')
xlabel('Temperature [K]')
ylabel('Effective Strains @ a strain rate of 1e-5/s')

% Examine n,m and K through plots for PNNL and MATPRO data
% add labels and plots
figure()
semilogy(t,n(t),t,n2(t),'-.',t,nprime(t,.001,1),'--',t,nprime(t,.1,1),':');
legend('MATPRO [NUREG-1180] and PNNL', 'MATPRO [NUREG-6150]', 'Adjusted [NUREG-6150]
(strain=.001)', 'Adjusted [NUREG-6150] (strain=.1)')
```

```
ylabel('Work Hardening Coefficient, n')
xlabel('Temperature [K]')
figure()
plot(t,m(t,1),'b',t,m2(t),'r--')
ylabel('Strain Rate Sensitivity, m')
xlabel('Temperature [K]')
legend('MATPRO [NUREG-6150]','PNNL')
figure()
semilogy(t,K(t),'b',t,K2(t),'r--')
ylabel('Strength Coefficient, K [Pa]')
xlabel('Temperature [K]')
legend('MATPRO [NUREG-6150]','PNNL')

% Check for multiple roots in solution function
figure();
t_test=1051.85+273.15;
E=logspace(-3,2,1000);
fun_4=@(max_Ep) max_Ep-
(sigma_eff(t_test,E_hoop(max_Ep),P_int(1))./K(t_test)./(max([strain_rat(1), 1e-
5])*1e3).^m(t_test,1)).^(1./n(t_test));
fun_5=@(max_Ep) max_Ep-
(sigma_eff(t_test,E_hoop(max_Ep),P_int(2))./K(t_test)./(max([strain_rat(1), 1e-
5])*1e3).^m(t_test,1)).^(1./n(t_test));
loglog(E, fun_4(E),'b-',E, fun_5(E),'r--')
xlabel('Maximum Strain')
ylabel('Solution function')
solution_fun4= fzero(fun_4,0)
solution_fun5= fzero(fun_5,0)
legend(strcat('P_i_n_t =',num2str(P_int(1)/1e6),' MPa'),strcat('P_i_n_t
=',num2str(P_int(2)/1e6),' MPa'))
```

```
Strain stress
nprime =
    @(T,mE,k)min(ANL(T),n(T).^2./(1+m(T,k))/mE)

error_check =
   1.3685e-11

solution_fun4 =
    0.2205

solution_fun5 =
    0.0229
```

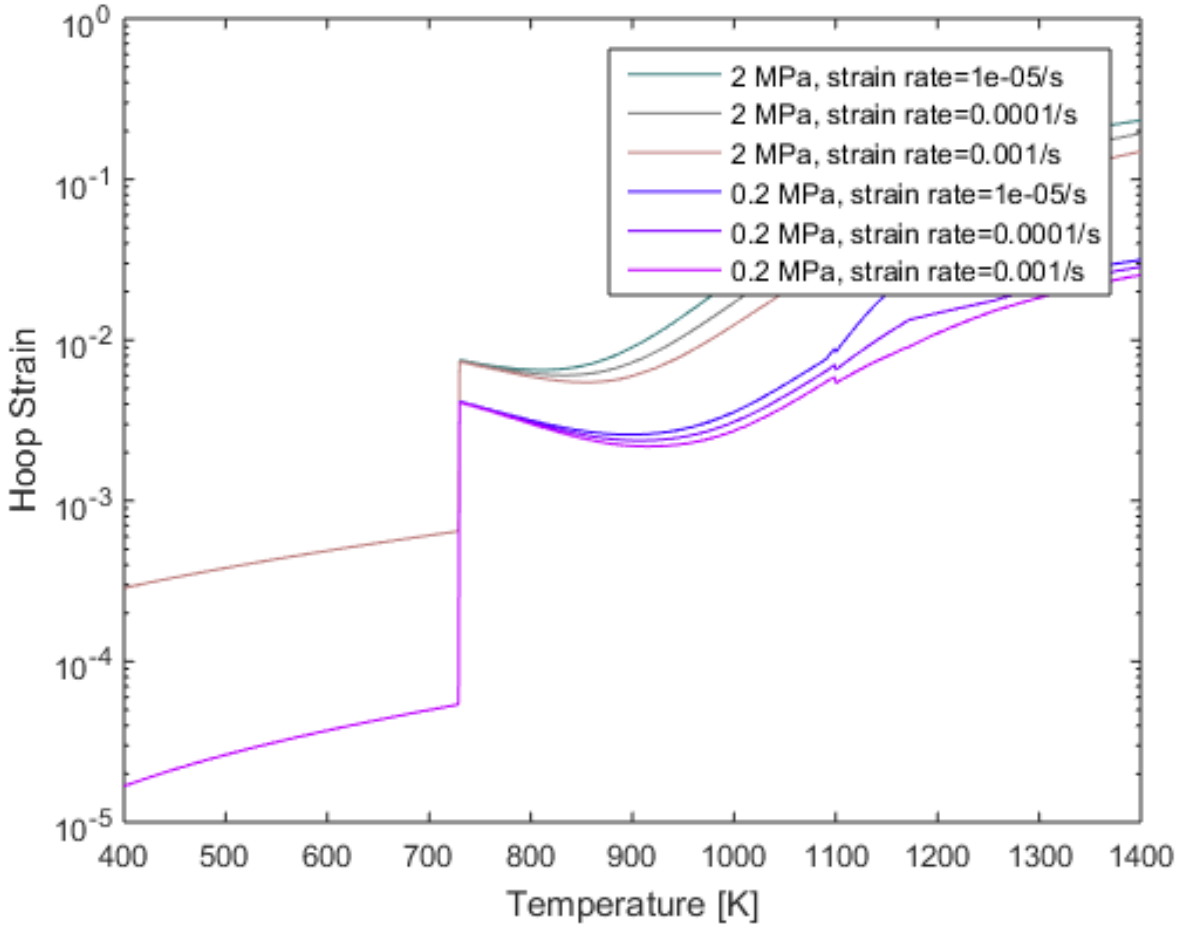

Figure 41: Hoop strains due to the fuel's internal pressure when the strain rate has diminished to between 10^{-3} and 10^{-5}

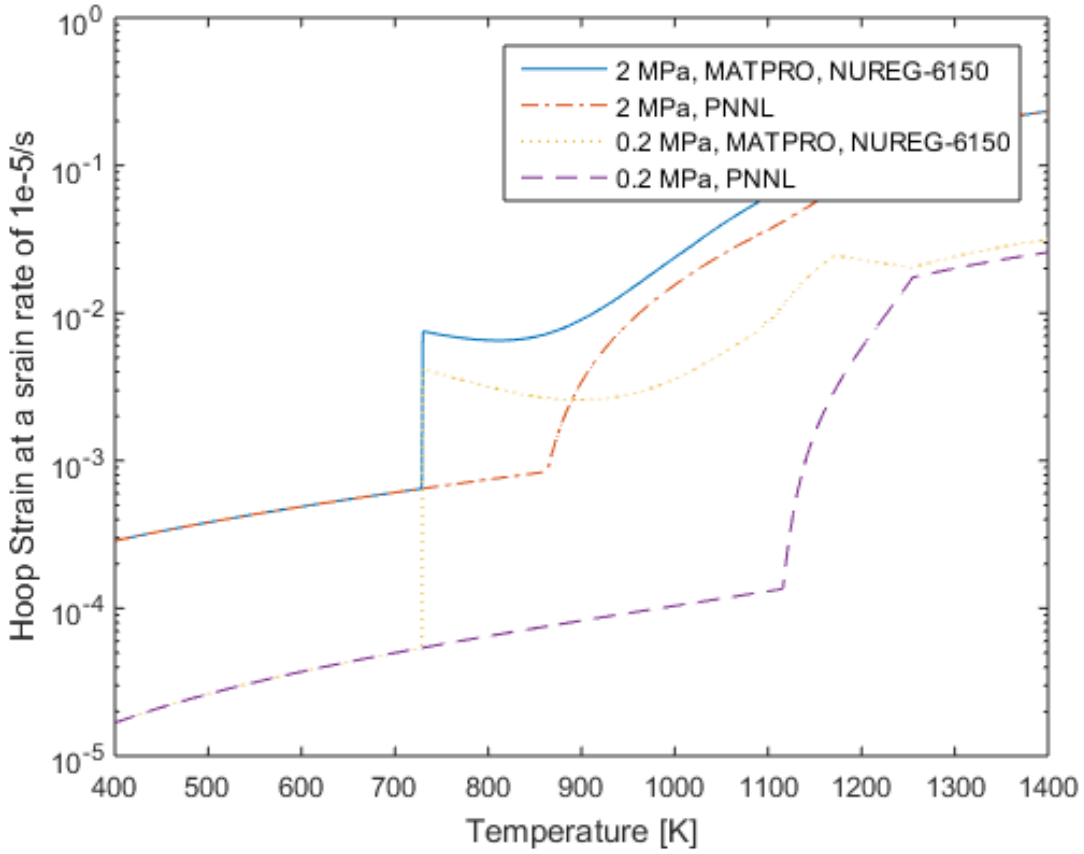

Figure 42: Comparison of the predicted hoop strain between PNNL [70] and MATPRO NUREG-6150 [68] data when a strain rate of 10^{-5}/s has been reached

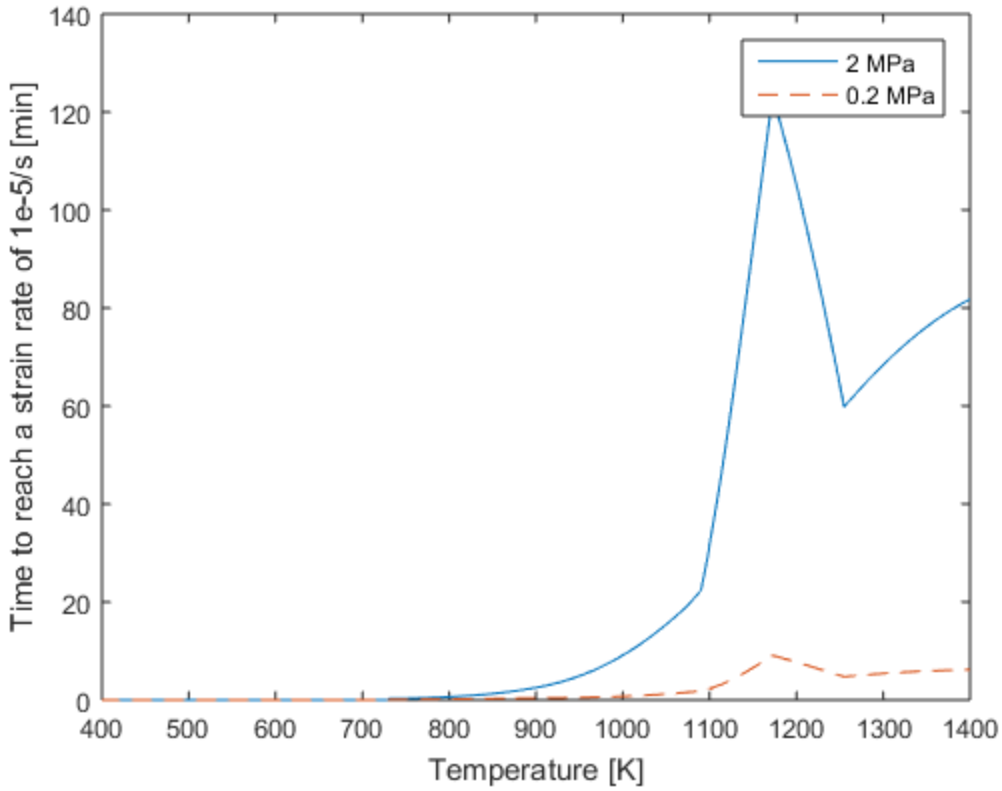

Figure 43: Time elapsed to reach a strain rate of 10^{-5}/ s for the MATPRO report NUREG-6150 material properties.

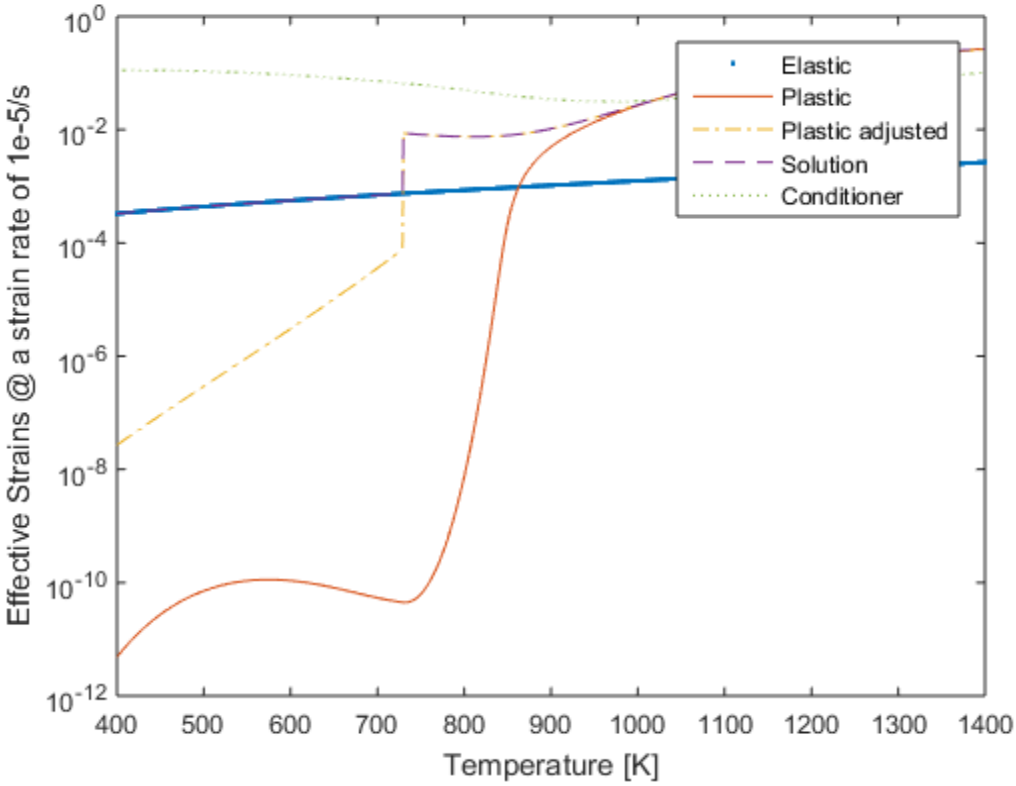

Figure 44:Debugging plot of elastic, plastic and plastic adjusted true effective strains. The function $n^2/(1+m)$ has been plotted against the strain to determine whether the condition for plastic strain adjustments has been met. The solution for the actual true effective strain has been plotted by selecting the appropriate calculation.

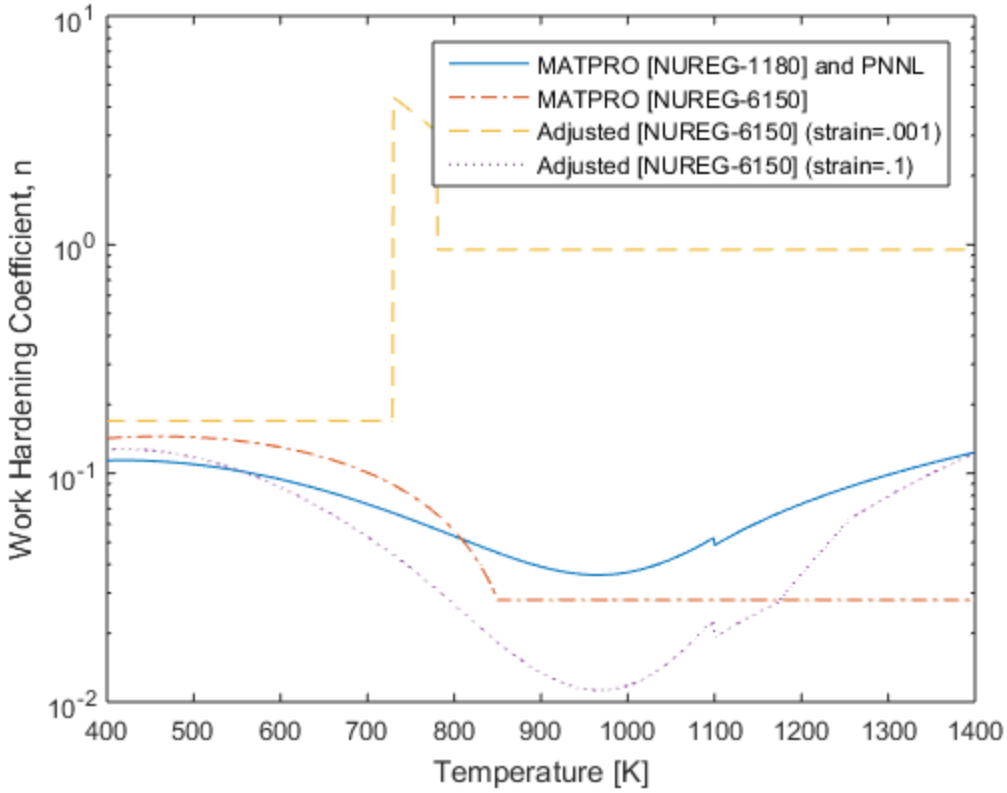

Figure 45: Work hardening coefficient, n, for the various versions of MATPRO and the adjusted values recommended by NUREG-6150 [68] for strains less than $n^2/(1+m)$. The relation recommended by the PNNL [70] is equal to that of NUREG-1180 [69].

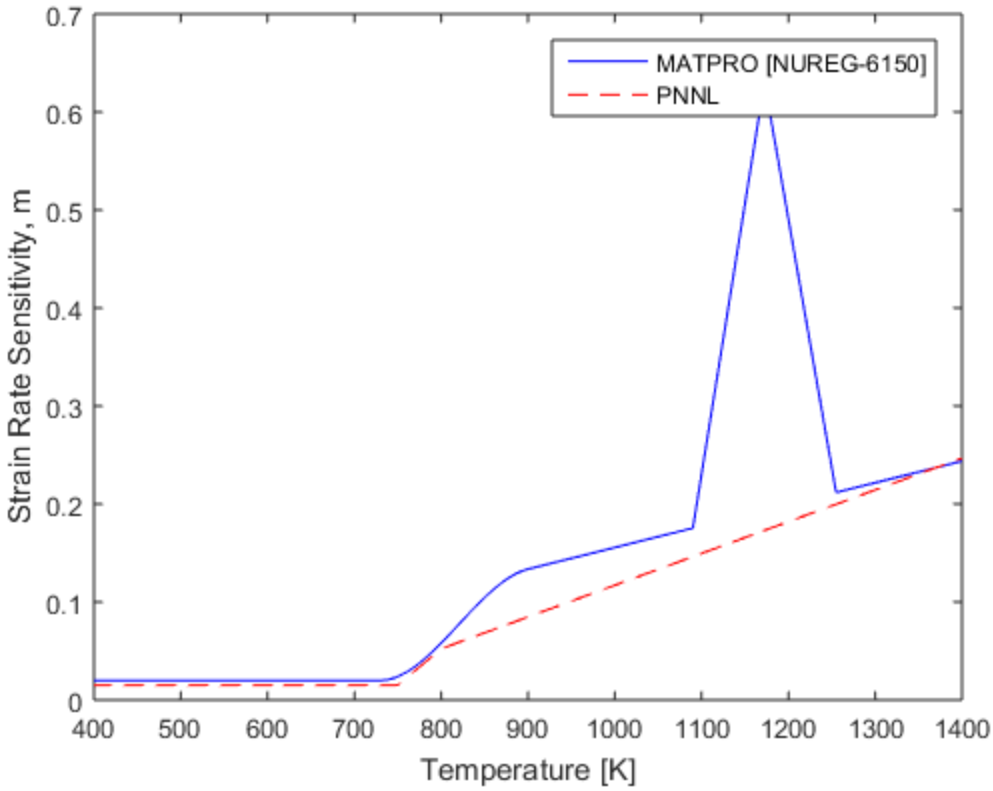

Figure 46: Strain rate sensitivity as a function of temperature (in Kelvin) provided by MATPRO NUREG-6150 [65] and the Pacific Northwest National Laboratory (PNNL) [67]. The strain rate, $\dot{\varepsilon}$, in the MATPRO correlation has been assumed to be equal to its minimum value, 10^{-5}.

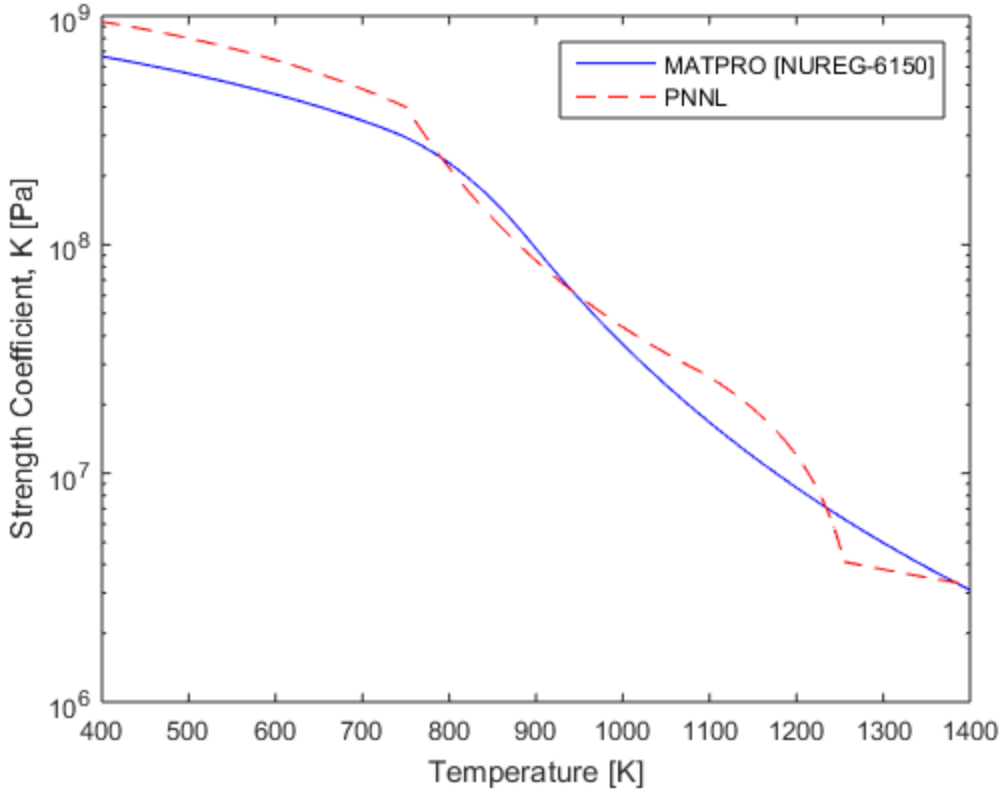

Figure 47: Correlations for the strength coefficient, K, provided by MATPRO [68] and the Pacific Northwest National Laboratory (PNNL) [70] as a function of temperature only

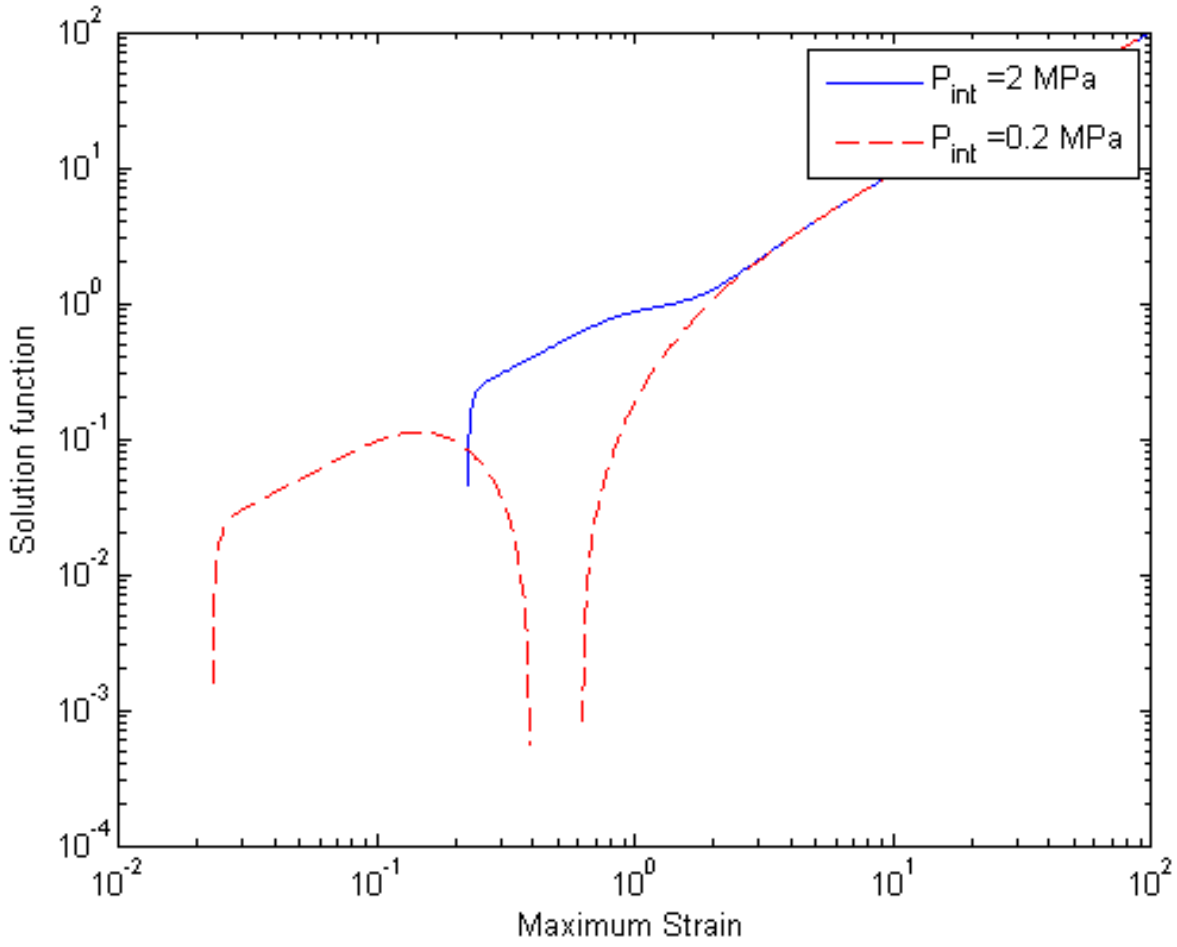

Figure 48: Debugging plot of the solution as a function of strain for the plastic strain equation (all curves are based on a strain rate of 10^{-5}/s). The maximum strain is determined from the roots of the solution function. This plot identifies multiple solutions for the 0.2 MPa case, which contradicts the assumption that the strain rate continually decreases. The minimum 'maximum strain' at which a strain rate of 10^{-5}/s is reached has been selected as the actual. The plot is discontinuous near zero due to the logarithmic plot's inability to show negative numbers.

Andersen Based Model

The MATLAB code and its associated outputs have been published in this appendix for a single rack without flow resistance. The section comprises of the analytical model based on literature for convection through large openings in buildings (Andersen [99] based model) and the finite difference model derived from the conservation equations.

Supporting Work for Master's Level Thesis at the Royal Military College Supervised by P.Chan and E.Corcoran By Derek Logtenberg. Last modified March 8th, 2018

```
clear all       %Clear previous workspace
close all
clc
disp('Andersen Based Model') %Title
disp(sprintf('\n'))

%Dimensions of Rack
Abot=1.595;     %m^2
h_=.13;         %m, gap between the floor and the bottom of the bundles
hmax=2.6-h_;    %m, assumes bottom compartment empty
As=(1.1+1.45)*hmax*2;   %m^2, total area with all four sides of the rack
Cd=[.65,.6,.55];        %Array of values for Coefficient of discharge

%Properties of the air at the inlet
pa=.94618;      %kg/m^3
Ta=373.15;      %K
Cp=@(T) heaviside(1600-T)*(1047.63657-0.372589265*T+9.45304214e-4*T^2-6.02409443e-
7*T^3+1.2858961e-10*T^4) ...
+heaviside(T-1600)* 1.246728323408001e3;%[relation from COMSOL material library for air]
approximately 1011 J/kg/K @373.15 K
eta_air=@(T)(1.1104e-07*T.^3-3.8687e-4*T.^2+6.9196e-1*T+7.335)*1e-7; %[relation from thermopedia
for dynamic viscosity of air]
g=9.81;         %m/s^2

%Determine Outlet values for a defined set of thermal rack powers, Q
Qmin=.001e6; Qmax=.5e6; %W, min and max rack powers in range
n=100;                   %Steps between min and max rack powers
Q=Qmin:(Qmax-Qmin)/n:Qmax;

%Solving constants
Tup=800; Tlow=375;      %Tmax and Tmin used by Bisection solver
m=length(Cd);           %number of values for the discharge coefficient
```

```
Andersen Based Model
```

Part 1: Calculate outputs for range of Rack powers and Discharge Coefficients

```
for j=1:m
    for i=1:n+1
        Gz=@(T) Cd(j)*pa*sqrt(Ta/T*g*hmax*(1-Ta/T)); %Momentum Equation
```

```
        Fun2=@(T) -Q(i)+Cp((T+Ta)/2)*Gz(T)*Abot*(T-Ta); %Energy Equation
        Ttop(i)=bisection(Fun2,Tup,Tlow); %Use bisection method to solve
        Gtop(i)=Gz(Ttop(i));
        Gside(i)=Gtop(i)*Abot/As;
    end

    %Loop Outputs
    disp(strcat('Cd value: ',num2str(Cd(j))))              % For each Discharge Coefficient Cd,
output the...
    disp(strcat('Outlet Mass Flux: ',num2str(Gtop(n+1)),' kg/m^2/s'))   % Top outlet mass flux
for max rack power
    disp(strcat('Inlet Mass Flux: ',num2str(Gside(n+1)),' kg/m^2/s'))   % Side inlet mass flux
for max rack power
    disp(strcat('Temperature: ',num2str(Ttop(n+1)),' K'))   % Top outlet bulk avg temperature for
max rack power
    disp(strcat('Outlet Density: ',num2str(pa*Ta/Ttop(n+1)),' kg/m^3')) % Top outlet density for
max rack power
    disp(strcat('Average Specific Heat Capacity: ',num2str((Cp(Ttop(n+1))+Cp(Ta))/2),' J/kg K'))%
Simple avg air specific heat for max rack powers
    Ttop_K(j,:)=Ttop; %Store outlet temperatures for each Cd for all rack powers
    disp(sprintf('\n'))

    %Plot the temperatures for each value of Cd for all rack powers
    plot(Q,Ttop_K(j,:),'Color',[0,j/m,j/m])
    hold on
end

%Add CFD values to the plot for comparison
CFD_Qvals= [.5e6,.35e6,.2e6,.05e6,0];        %CFD Rack powers tested
CFD_Ttop=[586.60, 534.67, 479.10,412.50,Ta]; %Bulk avg outlet temperatures
plot(CFD_Qvals,CFD_Ttop,'black*')            %Plot points
xlabel('Rack Thermal Power [W]');            %Add labels
ylabel('Outlet Temperature [K]');
ylim([373,650])                             %Adjust y axis
legend('Analytical Model C_d=.65','Analytical Model C_d=.6','Analytical Model C_d=.55','Laminar
CFD Model')
hold off

%Determine Reynolds numbers at the inlets and outlet
D_top=sqrt(Abot); %square side length of the top
D_sid=sqrt(As/4); % square side length of the sides
Re_top=Gtop.*D_top./eta_air(Ttop);
Re_sid=Gtop.*D_sid./eta_air(Ta);
```

```
Cd value:0.65
Outlet Mass Flux:1.4534 kg/m^2/s
Inlet Mass Flux:0.18402 kg/m^2/s
Temperature:583.276 K
Outlet Density:0.60532 kg/m^3
Average Specific Heat Capacity:1029.3417 J/kg K
```

```
Cd value:0.6
Outlet Mass Flux:1.3539 kg/m^2/s
Inlet Mass Flux:0.17143 kg/m^2/s
Temperature:598.4172 K
Outlet Density:0.59 kg/m^3
Average Specific Heat Capacity:1031.0045 J/kg K


Cd value:0.55
Outlet Mass Flux:1.252 kg/m^2/s
Inlet Mass Flux:0.15853 kg/m^2/s
Temperature:616.3649 K
Outlet Density:0.57282 kg/m^3
Average Specific Heat Capacity:1033.0169 J/kg K
```

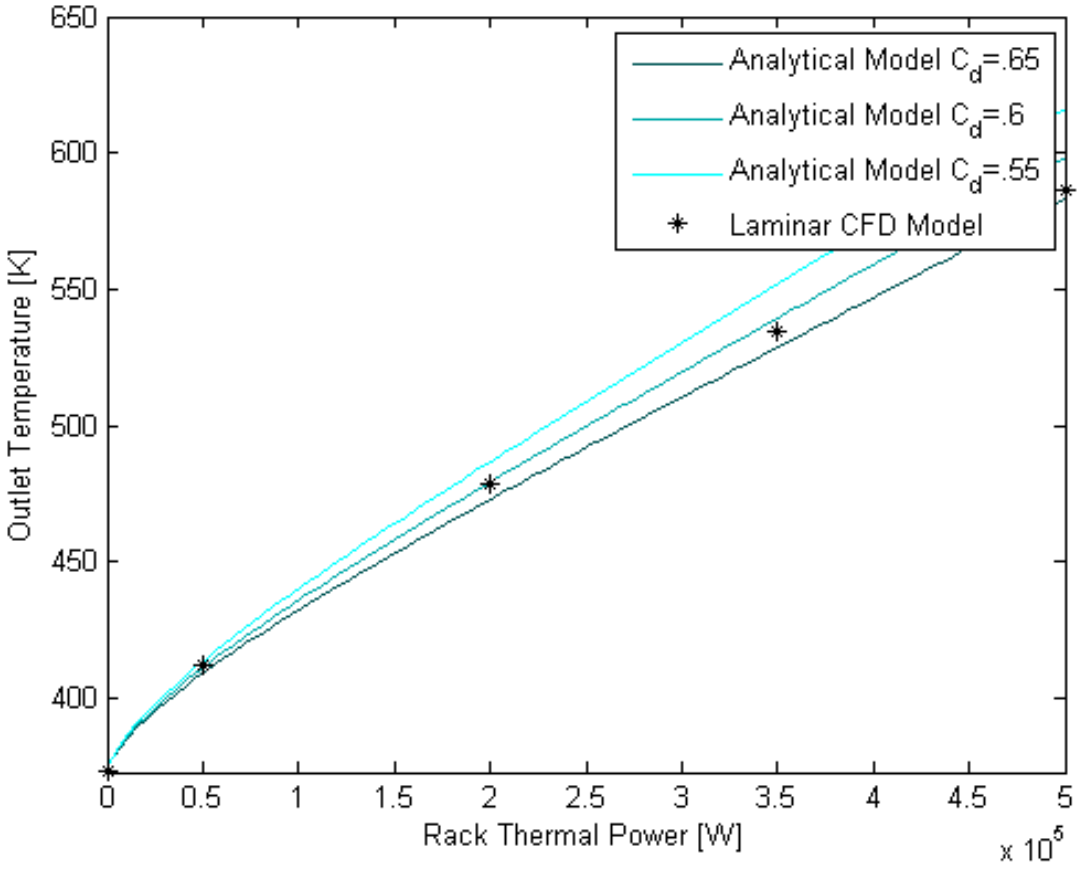

Figure 49: Comparison of the analytical model results (with various discharge coefficients) and CFD model's outlet temperatures as a function of the rack thermal output.

Part 2: Calculate outputs as a function of height, z, for max rack power, Q_{max} and for the Discharge coefficients, C_d

```
k=600;                  %number of vertical steps up the rack
h=hmax/k:hmax/k:hmax;   %heights at each vertical step
Q_=Qmax/k:Qmax/k:Qmax;  %rack power carried out at each vertical step

for i=1:k
    Gz=@(T) Cd(2)*pa*sqrt(Ta/T*g*h(i)*(1-Ta/T));    %Momentum equation
    Fun2=@(T) -Q_(i)+Cp((T+Ta)/2)*Gz(T)*Abot*(T-Ta);%Energy equation
    Tz(i)=bisection(Fun2,Tup,Tlow);                 %Temperature at vert step
    GZ(i)=Gz(Tz(i));                                %Mass flux at vert step
    if (i==1)
         GS(i)=GZ(i)*Abot/(As/k);
    end
    if (i>1)%if not the first vertical step
        GS(i)=(GZ(i)-GZ(i-1))*Abot/(As/k);% calc side flux
    end
end
disp('Producing plots for outputs as a function of height, z....')
disp(strcat('Side Mass Flux value: ',num2str(mean(GS))))%Calc the mean side flux
disp(strcat('Top Mass Flux value: ',num2str(GZ(k))))%Calc the mean side flux


%Plot mass fluxes as a function of height, z
figure()
plot(h,GZ) %plot vert flux
hold on
plot(h(1:k),GS(1:k), 'r') %plot side flux
xlabel('Rack Height,z [m]');
ylabel('Mass Flux [kg/m^2/s]');
legend('Vertical Mass Flux','Side Mass Flux')

%Plot temperatures as a function of height, z
figure()
plot(h,Tz) %plot temperatures
xlabel('Rack Height,z [m]');
ylabel('Temperature [K]');
```

```
Producing plots for outputs as a function of height, z....
Side Mass Flux value:0.17143
Top Mass Flux value:1.3539
```

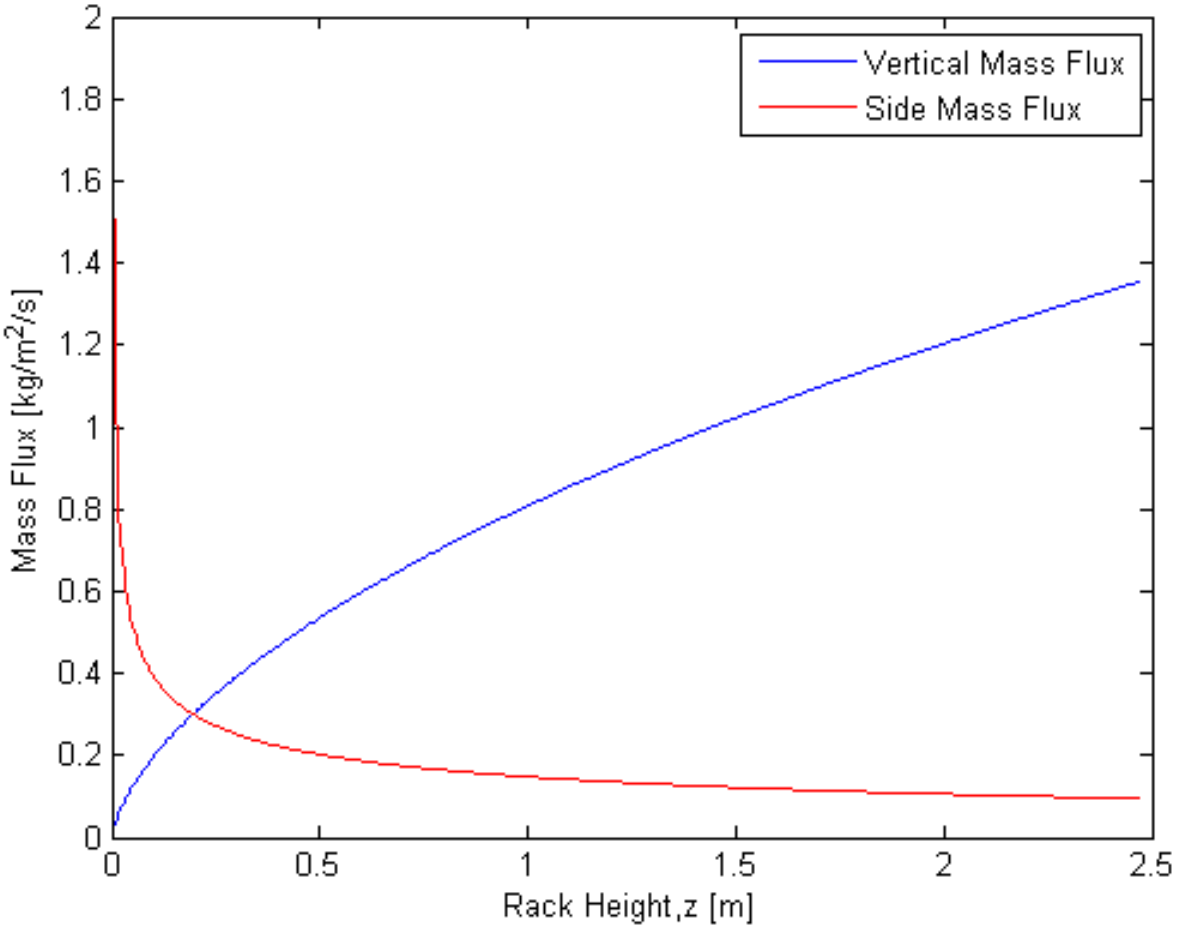

Figure 50: Side and vertical mass fluxes of air predicted by the Andersen based model along the rack's height

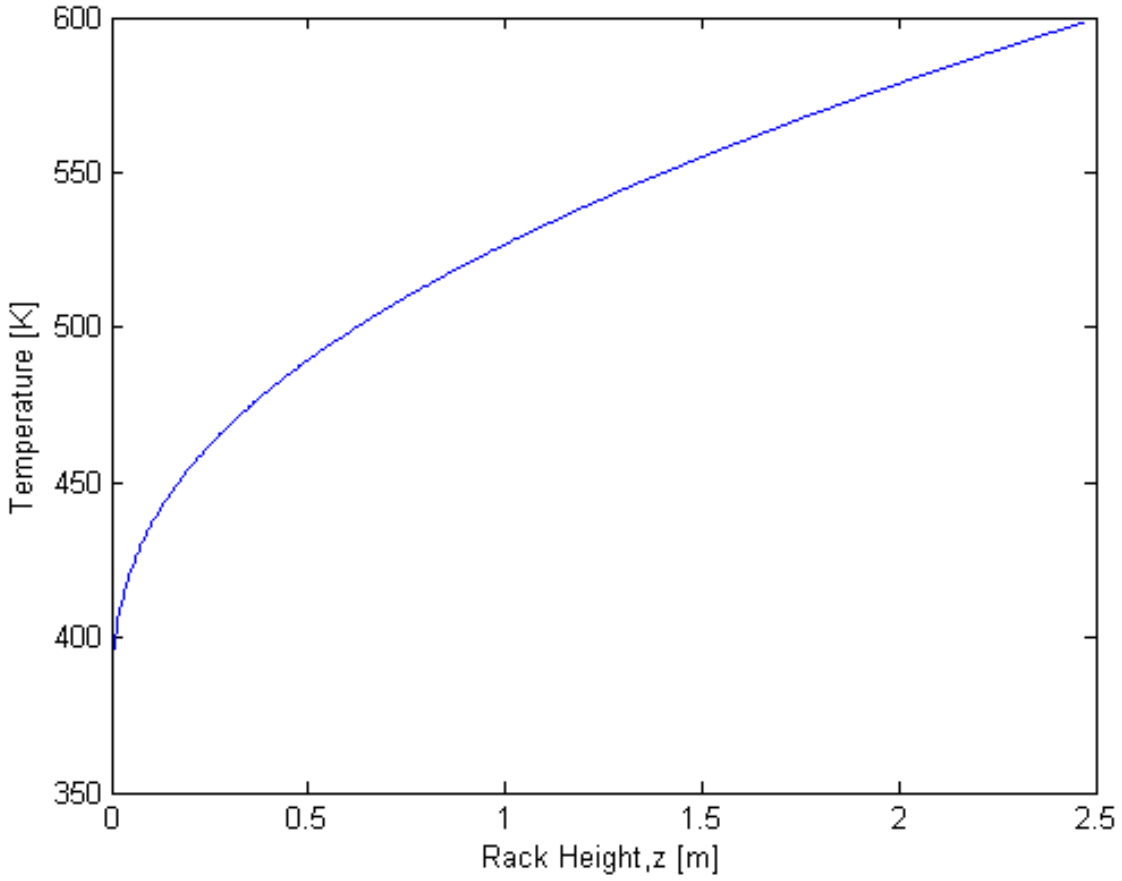

Figure 51: Bulk mean temperature of the air as a function of the rack's height for the Andersen based model.

Finite Difference Model

This script is designed to simulate air flow and temperatures through a rack during a LOCA via a 1D finite element method. Supporting Work for Master's Level Thesis at the Royal Military College. Supervised by P.Chan and E.Corcoran. By Derek Logtenberg. Last modified July 20th, 2018

```
clear all       %Clear previous workspace
close all
clc
disp('Finite Difference Model')
disp(sprintf('\n'))

%Dimensions of Rack
Abot=1.595;     %m^2, Bottom area of rack
h_=.13;         %m, gap between the floor and the bottom of the stack's bundles
hmax=2.6-h_;    %m, maximum height (assumes bottom compartment empty)
As=hmax*5.1;    %m^2, total area of the rack sides
Au=h_*5.1;      %m^2, area of the rack sides for the bottom compartment
```

```
n=160;          %Number of vertical steps
delz= hmax/n;   %m, vertical step size
Ai=zeros(n+1,1)+As/n;   %m^2, side area of a vertical step
h=h_:hmax/n:hmax+h_;    %m, height of the rack array for all vertical steps

%Properties of the air flow
spa=.94618;      %kg/m^3, density of air at the ambient temperature
Ta=373.15;      %K, ambient temperature of air
PCorrFactor_top=4/9; %correction factor for ratio of max to avg flow if
%flow has paraboloid shape
%PCorrFactor_top=2/3;%correction factor for ratio of max to avg flow if
%flow has absolute function shape
Cp=@(T) heaviside(1600-T).*(1047.63657-0.372589265*T+9.45304214e-4*T.^2-6.02409443e-
7*T.^3+1.2858961e-10*T.^4)...
    +heaviside(T-1600).*1.246728323408001e+03; %J/kg/K, Specific Heat capacity of air
%[relation from COMSOL material library for air]
g=9.81;         %m/s^2, gravity
Gz(1)=0;        %kg/m^2/s, Vertical mass flux at bottom of the rack
Tavg(1)=Ta;     %K, Temperature of incoming flow at the bottom of the rack
delP_z0(1)=0;   %Pa, Pressure difference at the bottom of the rack

%Solving constants
Tup=5e3; Tlow=373;          %K, max and min used by bisection solver
Qmax=.5e6;Qmin=.001e6;      %W, max and min rack powers to be tested
m=100;                      %number of steps between min and max rack powers
Q=Qmin:(Qmax-Qmin)/m:Qmax;  %array of all rack powers to be tested

%Initialize output variable for plot
Tout=zeros(m,1);            %K, outlet temperature for each rack power

for j=1:m
    %Initialize heat at steps for each rack power
    Qi(1)=0;                    %W, power at entrance
    Qi=zeros(n+1,1)+Q(j+1)/n;   %W, power at following vertical steps

    for i=2:n+1

        %Create functions for a, b, and c used in the quadratic formula
        a=@(T) (Ai(i)/Abot/PCorrFactor_top)^2/(2*pa/T*Ta);
        b=@(T) Gz(i-1)*(Ai(i)/Abot/PCorrFactor_top*(3/2/pa*(T/Ta)-...
            1/(2*pa)*Tavg(i-1)/Ta));
        c=@(T) Gz(i-1)^2*(1/pa*T/Ta-1/pa*Tavg(i-1)/Ta)-...
            pa*g*(h(i)-h_)+(Ta/Tavg(i-1)+Ta/T)*pa*g*delz/2-delP_z0(i-
1)+1/2/pa*Gz(1)^2*PCorrFactor_top^2;

        %Define the side mass flux, Gs for a vertical step using the
        %quadratic formula
        Gs=@(T) (-b(T)+((b(T).^2-4*a(T).*c(T)).^.5))./(2*a(T)); %kg/m^2/s

        %Conservation of energy equation
        Fun2=@(T) -Qi(i)+Cp(T)*PCorrFactor_top*Gz(i-1)*Abot*(T-Tavg(i-
1))+Cp((T+Ta)/2)*Gs(T)*Ai(i)*(T-Ta);
```

```
        %Use the bisection method to solve conservation of energy equation
        Tint=bisection(Fun2,Tup,Tlow);      %K, Average temperature in step
        Gside(i)=Gs(Tint);                  %kg/m^2/s, store side mass flux
        Gz(i)=Gside(i)*Ai(i)/Abot/PCorrFactor_top+Gz(i-1); %kg/m^2/s, solve for vertical mass
flux
        Tavg(i)=Tint;           %K, store Average temperature in step
        delP_zz(i)=(Gz(i)+Gz(i-1))*(Gz(i)*Tavg(i)/Ta-Gz(i-1)*Tavg(i-1)/Ta)/(2*pa)+...%
            (Ta/Tavg(i)+Ta/Tavg(i-1))*pa*g*delz/2; %Pa, Pressure difference between steps
        delP_z0(i)=delP_z0(i-1)-delP_zz(i);  %Pa, Pressure difference between the top and bottom
    end
    Tout(j)=Tavg(n+1);          %K, Store outlet temperature for each rack power
end

%Display outputs in text (Transposing values for easier viewing)
%These outputs may be supressed when a  large number of
%vertical steps are taken
disp('Probing values at the last iterated (max) rack power')
% disp('Average Temperature values for each vertical step [K]:')
% disp(Tavg')
% disp('Max (central) Vertical Mass Flux values for each vertical step [kg/m^2/s]:')
% disp(Gz')
% disp('Average Side Mass Flux values for each vertical step [kg/m^2/s]:')
% disp(Gside')
disp(strcat('Average Specific Heat Capacity for rack: ',num2str(mean([Cp((Tavg)) Cp(Ta)])),'
J/kg/K'))
disp(strcat('Average Side Mass flux for rack: ',num2str(mean(Gside)),' kg/m^2/s'))
disp(strcat('Average Outlet temperature for rack: ',num2str(Tavg(n+1)),' K'))

%Updating user on outputs
disp('Producing plots for outputs....')

%Plot Average temperature for each vertical step of the last iterated
%(maximum) rack power
plot(h,Tavg)
xlabel('Height [m]');
ylabel('Temperature [K]');

%Plot Maximum Vertical Mass Flux(in blue),the Average Vertical Mass Flux
%(in green) and the side mass flux (in red) for each vertical step of the
%last iterated (maximum) rack power
figure()
plot(h,Gz)
hold on
plot(h,Gz*PCorrFactor_top,'g')
xlabel('Height [m]');
ylabel('Air Mass Flux [kg/s/m^2]');
plot(h(2:n+1),Gside(2:n+1),'r')
legend('Centre Vertical Mass Flux','Avg Vert Mass Flux','Side Mass Flux')

%Plot Average temperatures at the outlet for all rack powers
figure()
plot([0;Q(2:m+1)'],[Ta;Tout])
```

```
xlabel('Thermal Rack Power [W]')
ylabel('Outlet Temperature [K]')
```

```
Finite Difference Model


Probing values at the last iterated (max) rack power
Average Specific Heat Capacity for rack:1040.5486 J/kg/K
Average Side Mass flux for rack:0.15102 kg/m^2/s
Average Outlet temperature for rack:626.4323 K
Producing plots for outputs....
```

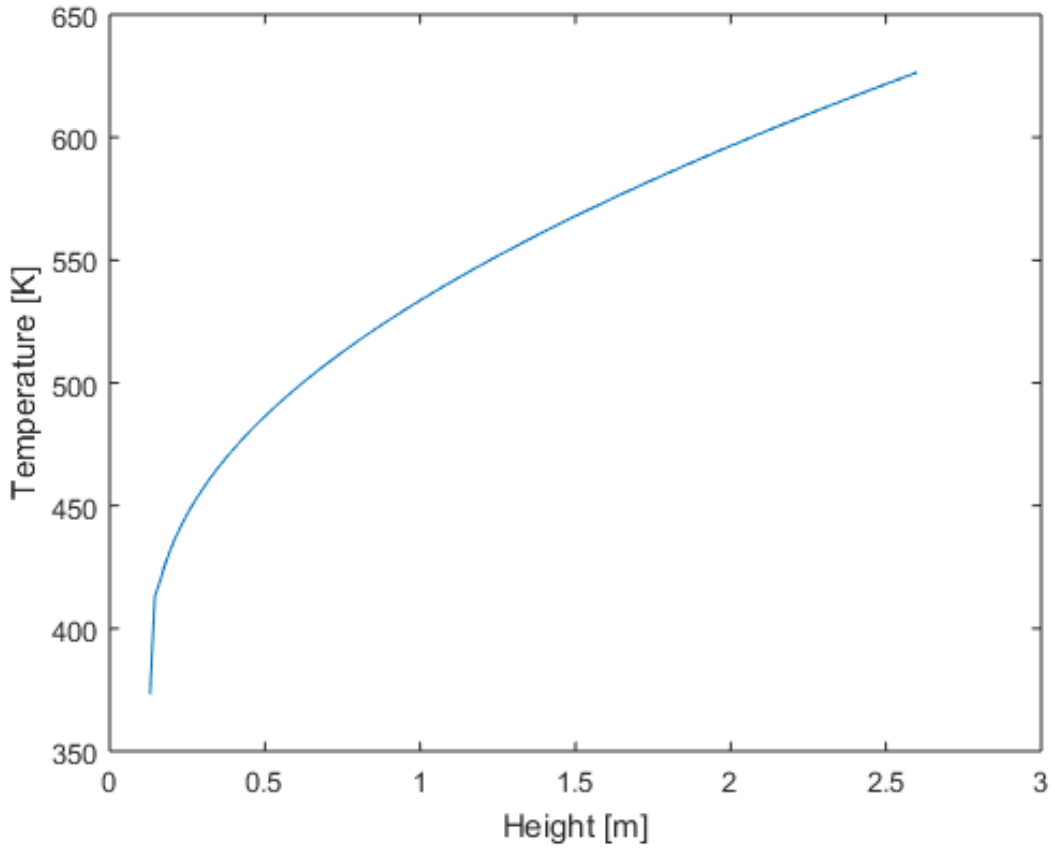

Figure 52: The finite difference model's bulk mean air temperature as a function of rack height. There is assumed to be an empty bottom compartment, so the rack's temperature is first measured at 0.13 m. '

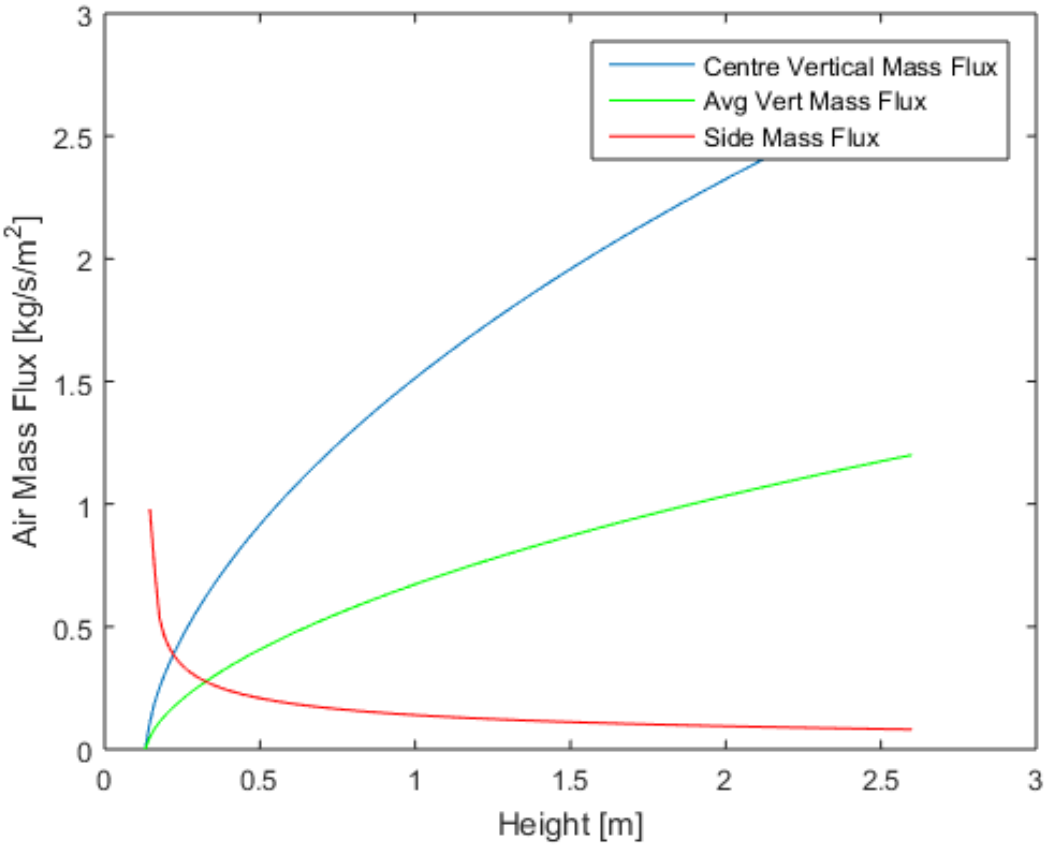

Figure 53: The finite difference moddel predicted side mass flux, rack average vertical mass flux and the mass flux at the rack's centre (i.e. The peak mass flux) are shown. The height is in reference to the ground, and therefore measurements inside the rack start at 0.13 m.

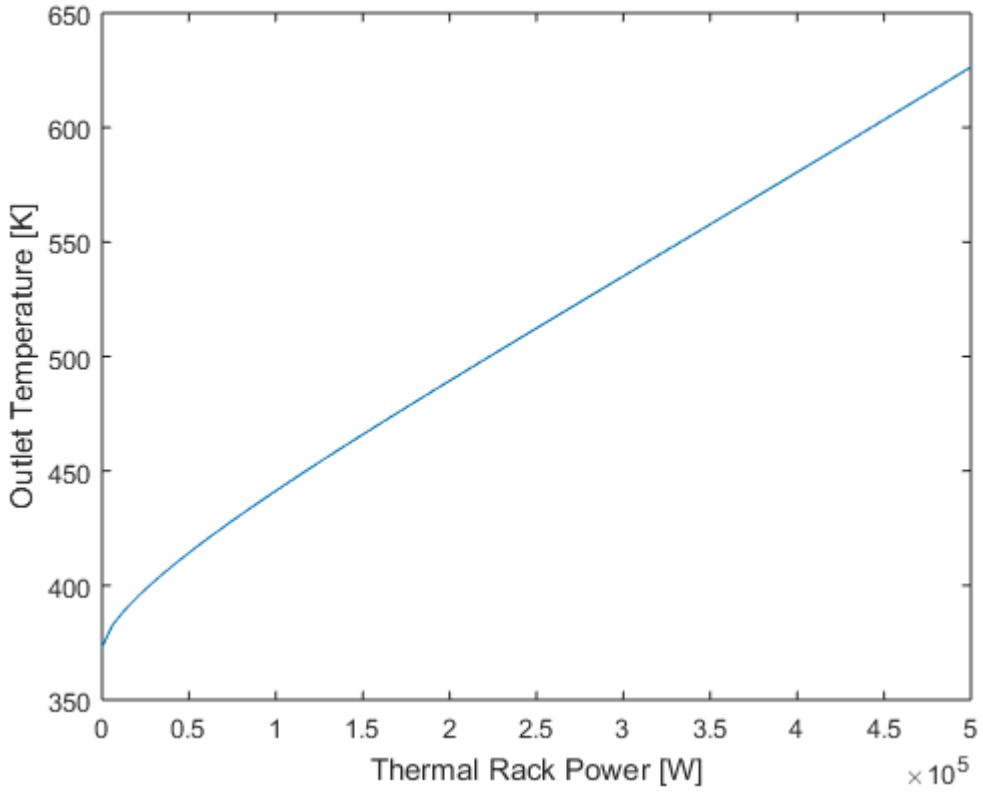

Figure 54:The outlet temperature predicted by the finite element model is shown as a function of the rack's total thermal power. Rack's are not expected to exceed 0.5 MW under normal loading conditions (This does not consider complete offloading of a freshly discharged core).

Published with MATLAB® R2015a

Bisection Method

This function is designed to solve the roots of a non-linear function in the form f (x) = x – g (x) where:

- f is the function itself
- x is the variable to be solved and outputted in the *answ*
- *upp* is the upper boundary of the search interval
- *low* is the lower boundary of the search interval

```
function answ = bisection(f,upp,low )
```

Supporting Work for Master's Level Thesis at the Royal Military College. Supervised by P.Chan and E. Corcoran. By Derek Logtenberg. Last modified October 20th, 2018

```
tol=1e-15;  % absolute tolerance of the solution, (accuracy of answ)
mloop=200;  % maximum number of loops
m=1;        % loop counter, which starts at 1 and goes to mloop
```

```
sol=0;      % solution flag, 0 = not found and 1 = found

% Search until solution is found OR until maximum # of loops is exceeded
while ((m<mloop)&(sol==0))

    %Test at the middle of the search interval
    new=(upp+low)/2;

    %If solves for the root perfectly or cannot be refined further,
    %raise solution flag
    if ((f(new)==0)|((upp-low)/2<tol))
     sol=1;

    %If tested value is greater than zero, set it as the new upper bound
    elseif (f(new)>0)
        upp=new;
    %Otherwise set as lower bound
    else
        low=new;
    end
    m=1+m;      %keep counting loops
end

answ=new;   %return solution

if (sol==0) %return errors and null solution if unsucessful
    disp('failed to converge');
    answ=0;
end
```

```
end
```

APPENDIX B: SUPPLEMENTARY DATA

Table 13 and Table 14 have been compiled to summarize model parameters used for characterizing the conductivity of the gap and zircaloy's thermal properties, respectively.

Table 13: Values for fission gas and helium properties collected from ELOCA [60]

	Fission Gas	Helium
Mole Fraction of Fission Gases	1.0	
Temperature Jump Distance at STP, g_0	0.26 µm	
Constant, s	0.8563	
Initial Pressure, P_g	488 x10^3 Pa	
Initial Temperature, T_g	293.15 K	
Critical Pressure, P_c	281.0 K	
Critical Temperature, T_c	5.86 MPa	
Approximate Temperature Jump Distance for spent fuel during heat-up, g	0.06 µm	

Table 14: Summary of material properties for zirconium used in the 2D cross-sectional model.

Material	Units	Expression
Zirconium Conductivity	W/(m K)	$7.51+(.0209)T - (1.45x10^{-5}) T^2+(7.67x10^{-9})T^3$
Zirconium Specific Heat Capacity at low temperatures (T<1115 K)	J/(kg K)	$6.55 \times 10^6 \frac{1.1061 \times 10^{-4} T+.2575}{\rho_{Zr}}$
Zirconium Specific Heat Capacity at high temperatures	J/(kg K)	$\frac{2.3318 \times 10^6}{\rho_{Zr}}$
Zirconium Density	kg/m^3	6550
Zirconium Cladding Emissivity (Oxidized)		0.8
Zirconium Emissivity (Unoxidized)		0.325

To inform the analysis, properties of CANDU spent fuel were consulted from various sources. The findings of a Romanian study is shown in Table 15.

Table 15: PIE data collected from Romanian experiment [75]

Dimension	Measurement
Sheath Diameter	13.14±0.04 mm
Fuel Rod Inner Pressure	488 kPa ±2%
Zirconium oxide thickness	2-3 μm
Pellet radius	6.13±0.02 mm
Burn-up	194.3 MWh/kgU
Sheath thickness	0.4 mm
Interfacial gap	.04±.04 mm